

Reference

NBS
Publi-
cations



A11106 979061

A11106 726625

NBSIR 78-1472

Materials For Fuel Cells

L. H. Bennett, M. I. Cohen, A. L. Dragoo, A. D. Franklin,
A. J. McAlister and K. F. Young

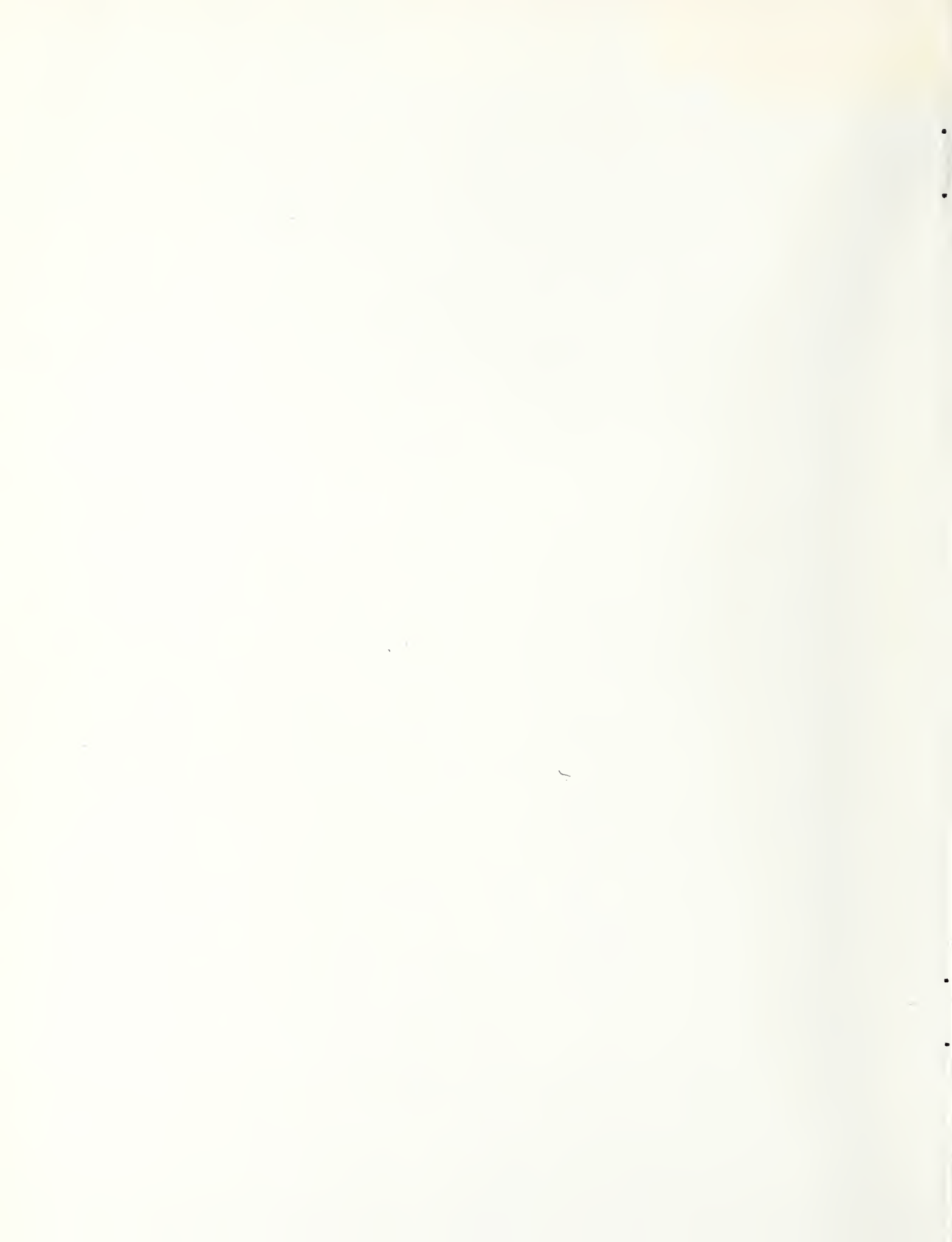
National Measurement Laboratory
National Bureau of Standards
Washington, D.C. 20234

Annual Report — January 1977 to December 1977

Issued July 1978

Prepared for
Power Systems Division
Department of Energy
Washington, D.C. 20545

QC
100
U56
78-1472



507 RCO 26
6100
101
157 100
NBSIR 78-1472

NBSIR 78-1472

MATERIALS FOR FUEL CELLS

L. H. Bennett, M. I. Cohen, A. L. Dragoo, A. D. Franklin,
A. J. McAlister and K. F. Young

National Measurement Laboratory
National Bureau of Standards
Washington, D.C. 20234

Annual Report — January 1977 to December 1977

Issued July 1978

Prepared for
Power Systems Division
Department of Energy
Washington, D.C. 20545



NBS Interagency Report 1977-1978

U.S. DEPARTMENT OF COMMERCE, Juanita M. Kreps, Secretary

Dr. Sidney Harman, Under Secretary

Jordan J. Baruch, Assistant Secretary for Science and Technology

NATIONAL BUREAU OF STANDARDS, Ernest Ambler, Director

Table of Contents

	Page
Abstract	1
1. Introduction	2
2. Subtask Reports	3
2.1 Electrocatalysis	3
Introduction	3
2.1.1 Electrocatalysis on Non-Noble Metals and Alloys	4
Introduction	4
Acid Stability Tests	4
Tungsten Carbide	5
Rhenium	7
$W_{0.5} Ti_{0.5} C$	7
$Mo_{1-x} W_x C$	8
Phosphides and Sulfides	14
2.1.2 Microprocessor - Controlled Potentiostat Electrochemical Measurements	16
Introduction	16
The Potentiostat	16
Basic Experimental Set-up and Design Criteria	17
The Microcomputer	19
Board-by-Board Details	22
Programming	38
System Use	40
Cost of Implementation	46
Acknowledgements	46

Table of Contents (Cont'd)	Page
2.2 High Temperature Solid Electrolytes	49
Introduction	49
2.2.1 Electrolyte Materials	51
Introduction	51
Homogeneous Precipitation of the Carbonates	54
Preparation of Mixed Oxide Powders via Organic Resins	58
Preparation of Mixed Oxide Powders via Extraction of an Organic Complex	62
Summary	63
Acknowledgement	65
2.2.2 Impedance Measurements	65
Introduction	65
Data Handling	65
Experimental Results - The Bulk Arc	67
Experimental Results - The Electrode Arc	79
Summary	90
2.3 Battery Materials	94
Introduction	94
2.3.1 Beta-Alumina	94
Introduction	94
Experimental	99
Results	102
Analysis	105
Discussion	109
Conclusions	117
References	118

TABLES

	Page
1. Electrocatalytic Activity of Tungsten Carbide Specimens.	6
2. Data Clock Rate Selection	28
3. Circuit Board Parts Cost and Commercial Availability	47
4. Resistance and Capacitance Values from ArcFits in Fig. 28.	71
5. Parameters for Electrode Arc for Hot-Pressed $\text{Ce}_{0.9} \text{Y}_{0.1} \text{O}_{1.95}$.	85
6. Comparison of Internal Friction Relaxation Energies.	117

1.	Rhenium metal, in 1 M H_3PO_4 at 22°C. Sweep rate is 0.002 Hz. Reference electrode is calomel.	9
2.	$W_{0.5}Ti_{0.5}C$, in 1 M H_3PO_4 at 22°C. Sweep rate is 0.002 Hz. Reference electrode is calomel.	10
3.	$M_{0.8}W_{0.2}C$, once leached in hot concentrated H_3PO_4 . Voltammetric sweeps in 1M H_3PO_4 at 22°C. Sweep rate is 0.002 Hz. Reference electrode is calomel.	11
4.	$M_{0.8}W_{0.2}C$, once leached in hot concentrated H_3PO_4 . Electrode is pretreated by Cathodic Polarization in presence of "Au". Voltammetric sweeps in 1M H_3PO_4 at 22°C. Sweep rate is 0.002 Hz. Reference electrode is calomel.	12
5.	Block diagram of potentiostat and cell.	18
6.	Block diagram of complete system.	23
7.	Schematic of CPU Board as modified. Also shown are components mounted on front panel.	25
8.	Memory map of system.	26
9.	Schematic of 8 kilobyte RAM Board. Also shown Power-on Reset circuit which is included on one RAM Board only.	27
10.	Schematic of Variable speed serial interface.	29
11.	Schematic of Timer-Converter Board: Address decoding system.	30
12.	Timer-Converter Board: Timer section.	31
13.	Timer-Converter Board: DAC section.	33
14.	Timer-Converter Board: modification to DAC section proposed for Interrupt-Triggered return to zero output.	34
15.	Timer-Converter Board: ADC section.	36
16.	Schematic of Signal Distribution Board.	39

17. a) Cross-assembled Data Acquisition Program	41
b) Data Acquisition Program (continued)	42
c) Data Acquisition Program (continued)	43
18. a) Sample of System Output	44
b) System Output (continued)	45
19. Aggregation and porosity.	
19a. Aggregate particle from a precipitation of Ce-Y hydroxides by the addition of ammonium hydroxide to a nitrate solution.	53
19b. Fracture surface of a sintered specimen which was fabricated from a powder containing aggregates similar to that shown in Fig. 19a.	53
20. Schematic of the carbonate procedure.	55
21. Ce-Y carbonate platelets.	60
22. Ce-Y oxide nodules prepared by homogeneous precipitation and dispersal in a succinic acid resin.	60
23. Ce-Y oxide, coarse aggregates after grinding; powder prepared by nonhomogeneous precipitation of the hydroxides and dispersal in a tartaric acid resin.	61
24. Ce-Y oxide aggregate and fines; powder prepared by nonhomogeneous precipitation of the hydroxides and dispersal in a tartaric-ethylene glycol ester resin.	61
25. Ce-Y oxide aggregate; powder prepared by nonhomogeneous precipita- tion of the salicylate and extraction into isoamyl alcohol.	64
26. Equivalent Circuit for Y-doped CeO_2 Ceramic with Sputtered Pt Electrodes.	66
27. Complex Impedance Plot for Bulk Arc for $\text{Ce}_{0.9} \text{Y}_{0.1} \text{O}_{1.95}$ in O_2 () and N_2 (x) at 350°C.	69

28. Complex impedance plots for $\text{Ce}_{0.9} \text{Y}_{0.1} \text{O}_{1.95}$ at temperatures near 70
 250°C. The curves are fitted to the data points from 31.6 kHz
 (indicated by the arrow) to 12 MHz (extreme left). They represent:
 1, O_2 at 253°C; 2, N_2 at 252°C; 3, O_2 at 248°C; 4, N_2 at 248°C;
 5, N_2 at 248°C. The data were taken in the order indicated, with
 an excursion to 804°C in O_2 between curves 1 and 2, and to 804°C in
 both O_2 and N_2 between curves 2 and 3.

29. Complex impedance plot for sintered $\text{Ce}_{0.9} \text{Y}_{0.1} \text{O}_{1.95}$ at 250°C in O_2 . 72
 Calculated values are from the equivalent circuit of Fig. 26 (high
 frequency side), fitted to the data. The arc represents Z_{gb}^* .

30. Complex impedance plot for hot-pressed $\text{Ce}_{0.9} \text{Y}_{0.1} \text{O}_{1.95}$ at 250°C in 73
 O_2 . Calculated values are from the equivalent circuit of Fig. 26,
 fitted to the data. The arc represents Z_{gb}^* .

31. Complex impedance plot for hot-pressed $\text{Ce}_{0.9} \text{Y}_{0.1} \text{O}_{1.95}$ in N_2 at 75
 several temperatures: \square , 252°C; \circ , 350°C; x , 470°C; $*$, 580°C.

32. Arrhenius plot for bulk resistance, R_B , for hot-pressed $\text{Ce}_{0.9} \text{Y}_{0.1} \text{O}_{1.95}$ 76
 in N_2 .

33. Complex impedance plot at low frequencies for hot-pressed 80
 $\text{Ce}_{0.9} \text{Y}_{0.1} \text{O}_{1.95}$ in O_2 at 702°C. \square , experimental points; x , cal-
 culated using eqn (9) with fitted values for R_d and τ , and with
 the exponent 1/2 replaced by n , whose value is selected by fitting.

34. Schematic of Porous Electrode-Electrolyte Interface. R_d denotes 81
 the resistive path for the oxygen discharge reaction, and W the
 diffusive path.

35. Comparison of experimental values (Ref. 63) for effective electrode 84
 capacitance per unit area ($C_z \text{A}^{-1}$) to values calculated with eqn. 16
 (see text). The solid line is illustrative of the expected behavior.

36. Complex impedance plots at low frequencies for hot-pressed	86
$\text{Ce}_{0.9} \text{Y}_{0.1} \text{O}_{1.95}$ in O_2 at 478°C (x) and N_2 at 470°C ().	
37. Complex impedance plot at low frequencies for hot-pressed	87
$\text{Ce}_{0.9} \text{Y}_{0.1} \text{O}_{1.95}$ in O_2 at 593°C (+) and in N_2 at 582°C ().	
38. Complex impedance plot at low frequencies for hot-pressed	88
$\text{Ce}_{0.9} \text{Y}_{0.1} \text{O}_{1.95}$ in O_2 at 702°C (+) and in N_2 at 694°C ().	
39. Complex impedance plot at low frequencies for hot-pressed	89
$\text{Ce}_{0.9} \text{Y}_{0.1} \text{O}_{1.95}$ at 804°C in O_2 (•) and in N_2 ().	
40. Temperature dependence of $\text{T}\Delta\text{Z}_{\text{el}}$ for $\text{Ce}_{0.9} \text{Y}_{0.1} \text{O}_{1.95}$ at 804°C	91
in Tank O_2 (•) and Tank N_2 ().	
41. Temperature dependence of C_z for $\text{Ce}_{0.9} \text{Y}_{0.1} \text{O}_{1.95}$ in tank O_2	92
and tank N_2 .	
42. Arrangement of ions in the conducting plane of beta-alumina. Dotted	96
lines enclose "cell"; two such "cells", on adjacent conducting planes,	
are included in the crystallographic unit cell. Na^+ ion sites are:	
1, BR site; 2, aBR site; and 3, MO site. Mirror planes described	
in text are indicated by dashed lines.	
43. Flexural strain produced in specimen bar for two orientations.	100
44. Experimental arrangement for internal friction experiment.	101
45. Internal friction for the sodium beta-alumina specimen with the	103
width horizontal. Falling temperature, x. Rinsing temperature 0.	
46. Internal friction for the sodium beta-alumina specimen with the	104
width vertical. Falling temperature x. Rising temperature 0.	
47. Internal friction for the sodium beta alumina specimen with the	106
width vertical, details of the temperature variation. Falling	
temperature x, rising temperature □, estimated equilibrium data +.	

	Page
48. Maximum systematic temperature error in internal friction data.	108
49. Arrhenius plot for internal friction in sodium beta-alumina. Data of Barmatz and Farrow (Ref. 74) o, our data with maximum systematic error added x, and subtracted □. The error bars are reported random error standard deviations.	110
50. Arrangement and jumps of split interstitials from one "cell" to another in sodium beta-alumina. aBR sites lie at intersections of trigonal network; MO sites are indicated by small filled circles. Lines connecting MO sites indicate possible split interstitials and arrows the paths from one "cell" to the next.	112
51. Approach of the split interstitial model for sodium beta-alumina to the activated state for both transport and reorientation jumps. The large circle is the lattice oxygen ion, the shaded circles are sodium ions on MO sites, and the small circle is the unoccupied MO site.	114

ABSTRACT

Research is described on hydrogen oxidation electrocatalysis on a number of compounds related to tungsten carbide (WC). Compounds in the molybdenum-tungsten carbide series, $Mo_{1-x}W_xC$ with $x \approx 0.2$, were found to be active, although some uncertainty exists about the purity of the samples. Some activity was also noted in $W_{0.5}Ti_{0.5}C$ and rhenium metal. Experiments on the preparation of molybdenum phosphide, MoP, and iron phosphide, FeP₂, are described.

The microprocessor-controlled potentiostat for electrochemical measurements was completed and is described in detail.

Experiments on several techniques for the preparation of very finely divided Y-doped CeO₂ powder are described, the powders to serve as raw materials for hot-pressing pure, dense, homogeneous ceramics. Straight sintering of some of these specimens yield densities of 95-97% theoretical.

The equivalent circuit previously suggested appears to fit very well the frequency-dependence of the impedance of sintered specimens of yttrium-doped cerium dioxide, $Ce_{0.9}Y_{0.1}O_{1.95}$, with sputtered or evaporated platinum (Pt) electrodes. The bulk part of the data is independent of oxygen partial pressure and varies with porosity as expected. An activation energy for the crystal conduction was obtained in agreement with literature values. High temperature instability in the Pt electrodes was observed. The electrode polarization impedance is fitted rather well by a Cole-Cole expression. It cannot be attributed to a model proposed earlier involving oxygen atom diffusion in the Pt electrode.

Internal friction experiments on a single crystal of sodium beta alumina, Na β -Al₂O₃, are interpreted in terms of the sodium ion motion. They are compatible with the split-interstitial model on mid-oxygen sites for the excess sodium ions, but not with the simple interstitial occupying anti-Beevers-Ross sites.

1. Introduction

The National Bureau of Standards has undertaken a program of research on materials for fuel cells and batteries. This program includes studies of electrocatalysis in liquid-electrolyte cells and of solid electrolytes, in high-temperature cells and in batteries. The overall objectives of the program are:

1. to provide data allowing selection of optimum materials for critical aspects of fuel cell operations;
2. to improve the measurement capability and standards for assessment of performance (e.g., efficiency of electrode processes and lifetime of components) of materials in fuel cells and batteries.

This report will describe the results for the second year of the program.

The Materials for Fuel Cells Program at NBS consists of four major elements, which taken together reinforce each other in techniques and concepts; these elements embrace:

- i. electrocatalysis, especially oxygen reduction, on non-metallic surfaces;
- ii. electrocatalysis, especially hydrogen oxidation, on non-noble metals and alloys;
- iii. degradation mechanisms involving solid oxygen-transporting electrolytes; and
- iv. mechanisms controlling transport of sodium ions in sodium beta-alumina.

Items ii and iii were partially supported by DOE during this past year, and item i was essentially dormant but work will be resumed in the coming year. This report will cover progress in items ii, iii, and iv.

2. Subtask Reports

2.1 Electrocatalysis

Introduction

In most fuel cell applications a major contribution to the overvoltage, and therefore to a reduction in useful voltage and to efficiency, comes from electrode polarization. For use in hot H_3PO_4 no satisfactory substitutes for Pt have been found, but Pt is not completely satisfactory. In catalyst loadings sufficiently large to ensure adequate efficiency and lifetime it makes a significant contribution to the cost. At the anode its sensitivity to CO poisoning forces the use of higher temperatures and catalytic shift conversion in the fuel processing train. At the cathode a mixed potential situation seems to exist and the open-circuit voltage lies below what should be possible. Thus a continued study of electrocatalysis and electrocatalysts in H_3PO_4 is worthwhile.

In our program we have elected to study refractory metal-metallloid compounds (e.g. WC) as potential anode catalysts. Work on oxide catalysts for use at the cathode was suspended for lack of funds, but some effort has gone into automating the electrochemical measurements used in studying electrocatalysis of either kind. These two lines of work are reported here.

2.1.1. Electrocatalysis on Non-Noble Metals and Alloys

Introduction

A limiting factor in full scale implementation of the low temperature acid fuel cell for electric power production is the scarcity and expense of Pt, the current material of choice for fuel and oxygen electrocatalysts. In the search for adequate non-precious substitutes for Pt, the "refractory hard metals" - alloys of transition metals with carbon, boron, nitrogen, etc. - offer a promising area of investigation, for they are platinum-like in a number of respects: they have d-band vacancies, have refractory properties, and display considerable chemical activity. Several such materials, notably WC and CoP_3 , have been shown to have useful H_2 oxidation activity and acid stability over practical ranges of voltage. This project entails a general search for other acid stable, catalytically active materials, and includes detailed characterization of known active materials as a guide to achieving this end.

Acid Stability Tests

Four samples of transition metal compounds having the NiAs structure were obtained commercially and examined. The NiAs structure is closely related to the WC structure; WC has metal atoms at simple hexagonal sites, and C repetitively occupies but one of the two trigonal sites in the primitive cell; in the NiAs structure, the unit cell is doubled, with the metalloid occupying the trigonal sites alternately. Samples of FeSe, VS, CoS, and NiS were examined. All reacted visibly with hot concentrated H_3PO_4 (85%, 82°C), the NiS more slowly than the others. Studies of the NiS by cyclic voltammetry showed no activity for H_2 oxidation in H_3PO_4 .

A number of commercially obtained phosphides were also examined. FeP , Fe_2P , Co_2P , and Ni_3P all reacted rapidly with the hot, concentrated H_3PO_4 . A sample of "MoP" proved to be only unreacted elements. $\text{Fe}_{40}\text{Ni}_{40}\text{P}_{14}\text{B}_6$ ("Metglas") reacted very slowly, but showed no H_2 oxidation activity.

Samples of the superalloy component $\text{Ni}_{3-x}\text{Al}_{1-x}\text{Ti}_x$ are attacked very slowly by hot H_3PO_4 . Their stability and possible activity will be studied voltammetrically.

Tungsten Carbide

Since the earliest work on WC, it has been realized that oxidative treatment tends to enhance its catalytic activity. We predicted [1]¹ on the basis of H_2 uptake and Auger surface analysis measurements on variously prepared WC samples by Ross and Stonehart [2] that alloying substitution of oxygen for carbon in WC was responsible for this enhancement. We therefore carried out hydrogen oxidation measurements on a series of WC samples prepared in different ways, some intended to include oxygen as an alloying addition in the bulk lattice. Two samples were carburized tungsten foils. The rest were powders of mesh size ranging from -200 to +400. Identification of the product was by x-ray diffraction. Powder electrodes were prepared by hot pressing Teflon 30 bonded powders onto Au disks coated with a thin layer of teflon. Cyclic voltammetric measurements were carried out on flooded electrodes, in stirred 1M H_3PO_4 at 22°C , with either H_2 or N_2 bubbled as appropriate. Results are summarized in Table 1.

¹ Figures in brackets indicate the literature references given at the end of this report.

Table 1
Electrocatalytic Activity of Tungsten Carbide Specimens

Sample No.	Form	Preparation	H_2 Oxidation Current Per Unit Capacitance at +0.3 Volts (RHE)
1	foil	$W + CH_4$	5.7×10^{-3} A/F
2	powder	$W + C$	10.1×10^{-3} A/F
3	powder	$WO_3 + C$	17.1×10^{-3} A/F

Preparation and Support:

- 1) Sheet, formed by exposing 0.5 mil W sheet to a 5% CH_4 -95% H_2 mixture for 4 hours at 1500°C. Supported on epoxy.
- 2) Commercially obtained powder, formed by direct reaction of W with carbon. Supported on Ta sheet.
- 3) Powder, formed by heating WO_3 and carbon powder for 2 hours at 1800°C in H_2 . Supported on Ta sheet, and on Au with teflon bonding.

Current is normalized to capacitance, evaluated from the sweep rate and current at +0.3 volts (RHE).

Clearly, those samples likeliest to contain alloyed oxygen in the bulk show the greatest specific activity. This result has been confirmed in much greater detail in a recent paper by Ross and Stonehart [4] who report activity and characterization (x-ray diffraction, Auger, and ESCA) measurements on variously prepared samples, and definitely correlate higher activity with the presence of carbon substituted oxygen.

The mechanism of this oxygen-alloying effect remains unclear. Perhaps it is simply a local electronic structure effect, but there are indications that crystallite morphology plays an important role here. We are preparing WC samples of varying oxygen content and activity by the method of Kulcickyj and Petrdlck (CO carburization of tungstic acids variously precipitated from ammonium metatungstate solution).

Microstructure and crystallite morphology will be studied by x-ray diffraction and electron microscopy and correlated with sample hydrogen oxidation activity.

Hydrogen oxidation activity and a useful range of acid stability were observed in several materials this year. Brief discussions of each material follow.

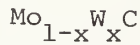
Rhenium

In our published studies of the electronic structure of WC [3] we noted similarities between the experimental state distribution of WC and the calculated density of states of the hcp metal Re (filled to an electron per atom ratio of 6, as a model for hexagonally coordinated W). It was of interest, therefore, to examine Re metal for stability and H_2 oxidation activity in H_3PO_4 . Fig. 1 shows voltammetric sweeps on a Re electrode fabricated by pressing Teflon 30 bonded Re powder (99.99% stated purity) onto a teflon coated Au disc. Activity is observed, with corrosion onset at $\sim +0.7$ volts (RHE).

W_{.5}Ti_{.5}C

WC is catalytically active while W metal is not. We have shown [3] that this change in chemical activity accompanies a change in the local distribution in energy of electronic states at W sites from W to WC. Two factors play a role here: an electronic factor arising from interaction of the metal with the metalloid; and a geometric factor associated with the difference in lattice symmetry. This latter factor makes it of interest to look for activity by W in other than hexagonal refractory hard metals. Voltammetric sweeps of the alloy W_{.5}Ti_{.5}C (cubic NaCl structure) are shown in Fig. 2. The material is active. If one assumes its specific

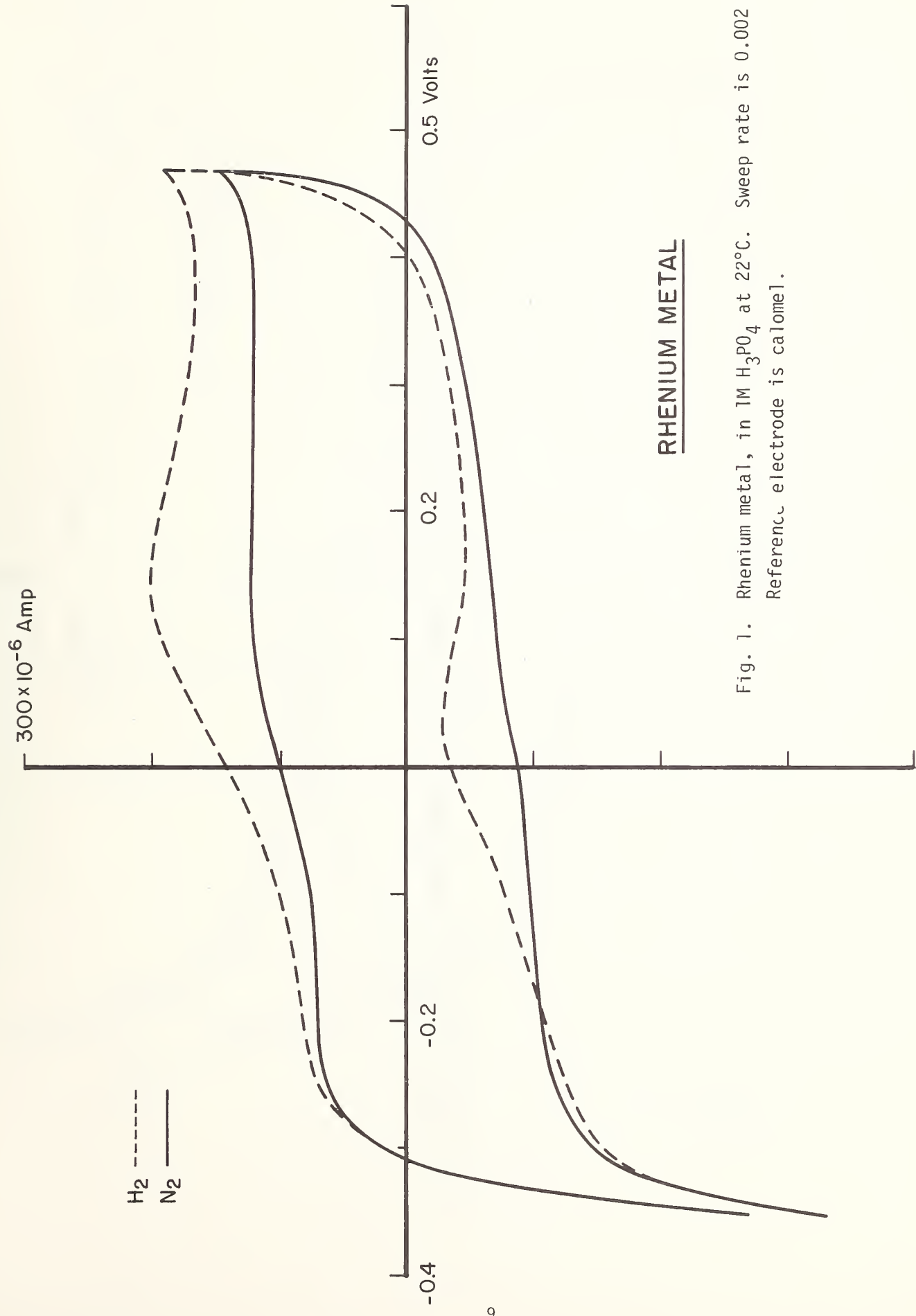
capacitance to be approximately equal to that of WC, then its specific activity scales about as the concentration of W, relative to a WC sample of low or no bulk oxygen content.

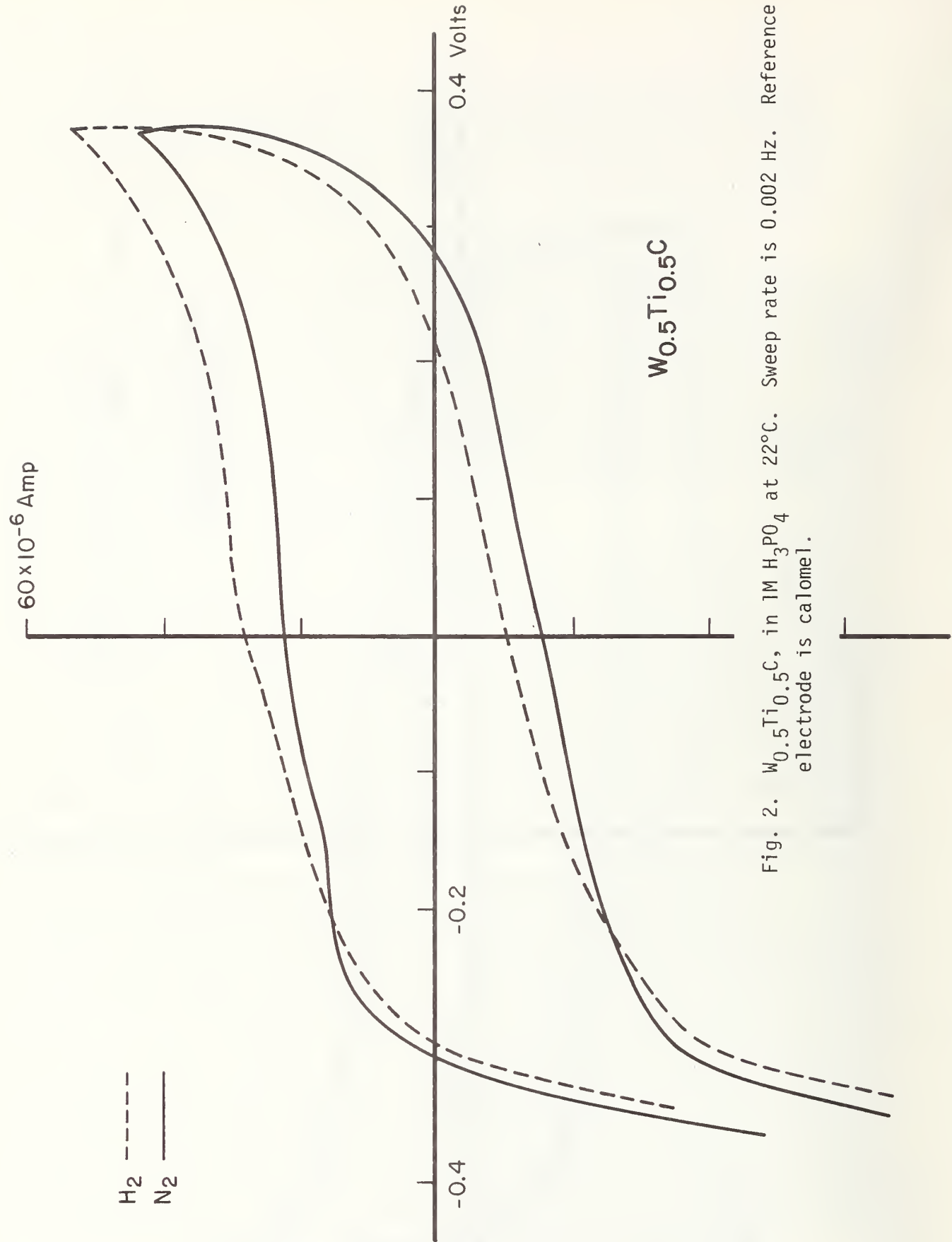


We have continued our study of the $\text{Mo}_{1-x} \text{W}_x \text{C}$ system, which condenses in the WC structure. We have examined additional electrodes made (a) from our original sample of $\text{Mo}_{.8} \text{W}_{.2} \text{C}$, and (b) from a second sample of $\text{Mo}_{.82} \text{W}_{.18} \text{C}$. All of these electrodes show some activity for H_2 oxidation, but none as high overall or so good at low overpotential as that upon which we commented in earlier reports.

This compound is difficult to make, and up to 2% by weight of Ni and/or Co is added to the reactants to catalyze the solid state reaction. Neither Ni or Co is believed to dissolve in the bulk, but some small amount may. In addition, Fe metal was found to contaminate the first sample as received; it was probably introduced during the grinding to powder of the porous lumps produced during compound formation. These contaminants react slowly, with visible discoloration, with hot concentrated phosphoric acid. The present measurements were made on electrodes fabricated from powders (a) cleaned by leaching in hot concentrated H_3PO_4 for several days, then washing, or (b) by repetition of step (a) until no further discoloration of the acid could be observed.

The active electrode of $\text{Mo}_{.8} \text{W}_{.2} \text{C}$ described in our last report was made from once-leached powder, as in procedure (a), bound with diluted Teflon 30, and hot pressed onto an Au disc coated with teflon. It was discovered that this support "leaked"; that is, the Au was exposed to the acid, and its voltammetric characteristics could be seen at high





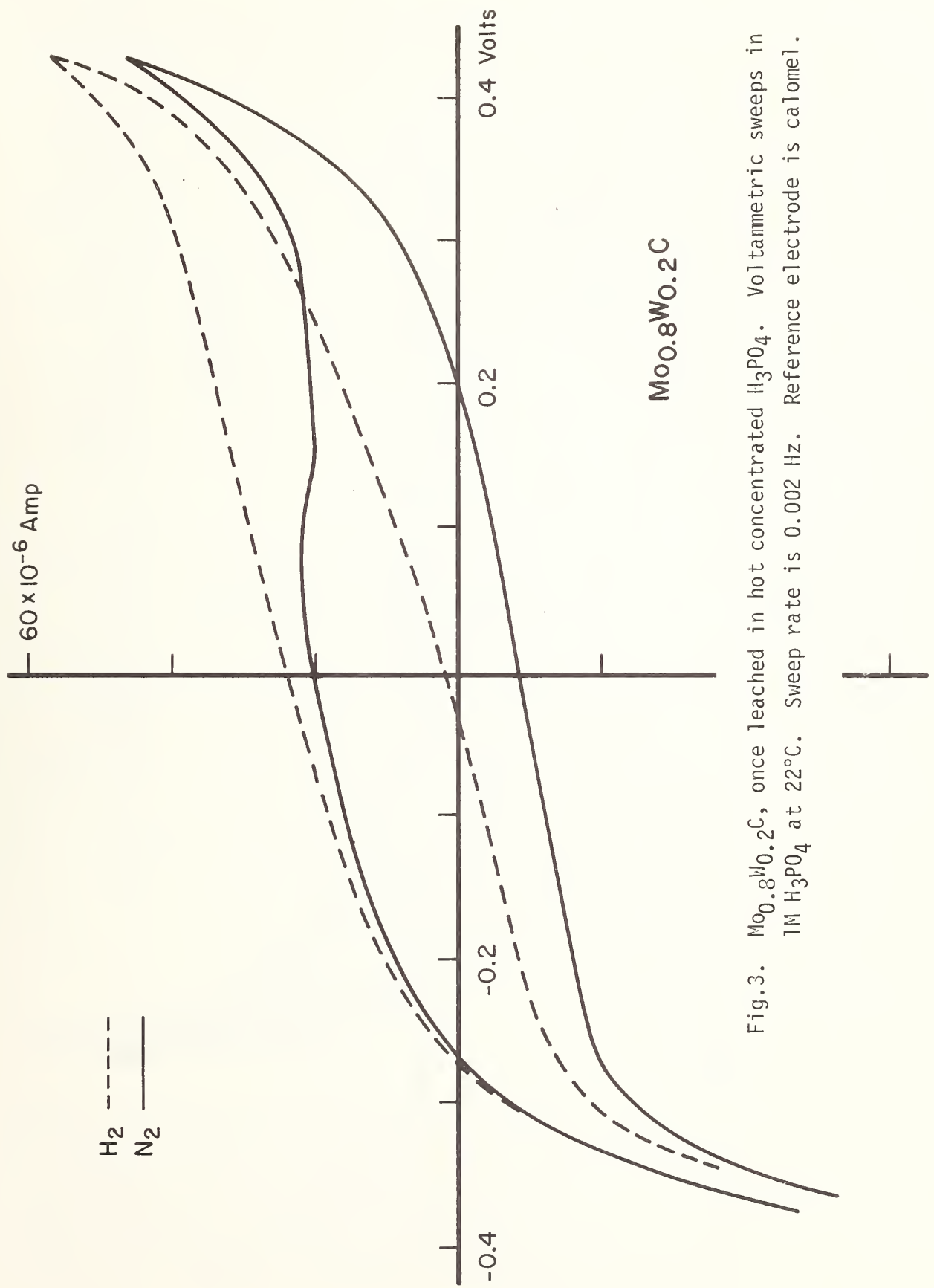
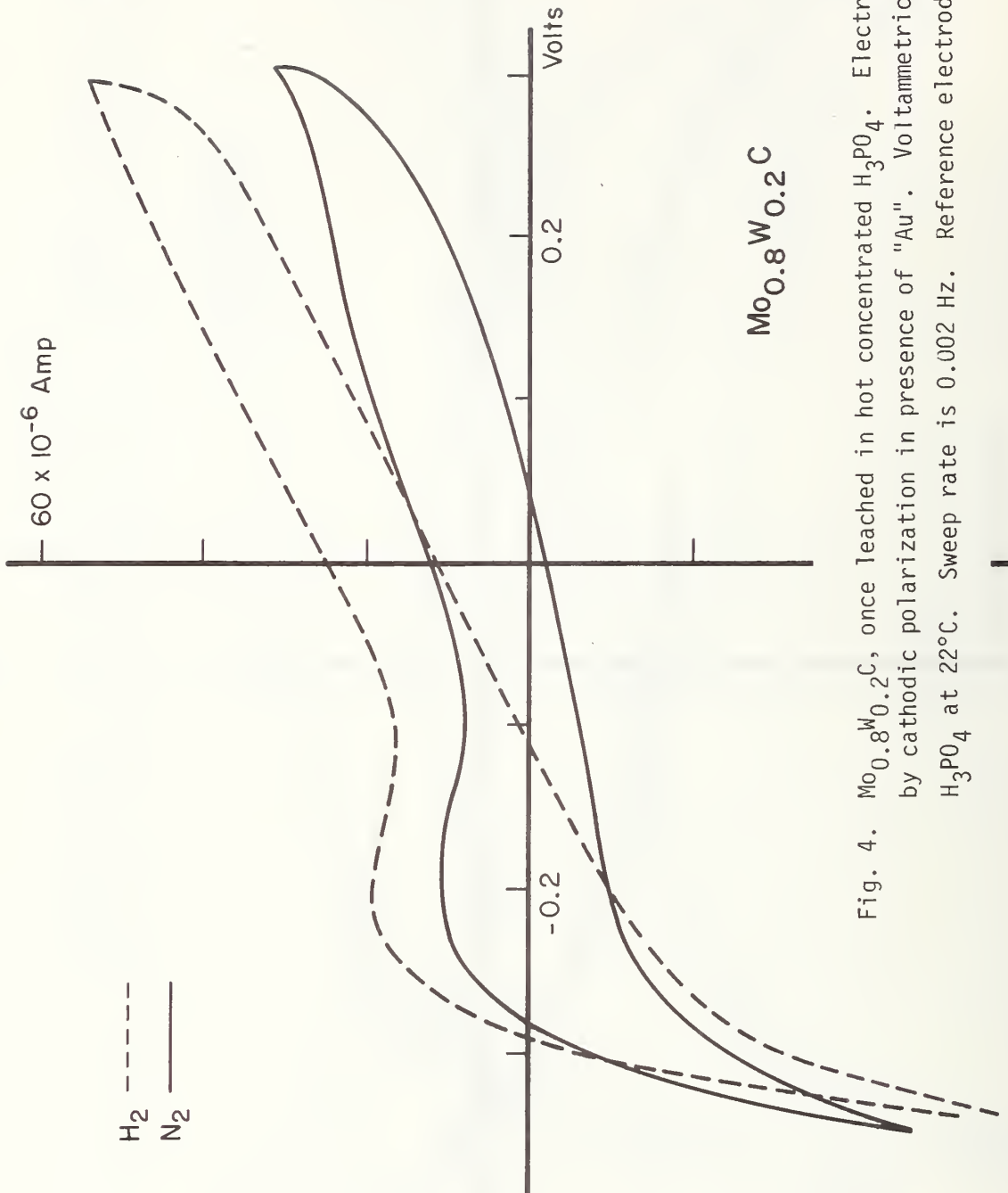


Fig.3. $\text{Mo}_{0.8}\text{W}_{0.2}\text{C}$, once leached in hot concentrated H_3PO_4 . Volammetric sweeps in $1\text{M H}_3\text{PO}_4$ at 22°C . Sweep rate is 0.002 Hz. Reference electrode is calomel.



potential; moreover, the Au stock from which the discs were fabricated was slightly active, due to contamination, although not as active as the given electrode. Two new samples on Au discs were fabricated from the $Mo_{.8}W_{.2}C$ lot, one from the once-leached powder, and one from repetitively leached powder of the same lot. Neither sample "leaked".

The once-leached material is active (Fig. 3), though not nearly as active as our earlier "Au-leached" sample. The activity of the once-leached sample can be enhanced somewhat by a pretreatment in which the electrode is placed in contact with a strip of (contaminated) Au stock and repetitively swept up to the O_2 evolution potential. (Fig. 4)

A recheck of our earlier data on WC, Re, and $W_{.5}Ti_{.5}C$, indicated that none were affected by Au "leakage", but currently, all electrodes are pressed onto teflon alone, with electrical contact being made with Ta metal which, as we have shown in earlier work, is passive over a wide voltage range in H_3PO_4 .

Evidently, the compound $Mo_{1-x}W_xC$ is active for the oxidation of H_2 , although not as active as our first experiment indicated. It is difficult to prepare this material in pure form; we have not yet succeeded in doing so ourselves. Studies on the $Mo_{1-x}W_xC$ system continue. Eight new production lot samples from WaChang-Teledyne² have been leached in hot H_3PO_4 to remove Fe contamination, and teflon mounted electrodes are being prepared for activity testing.

²Certain commercial equipment, instruments, or materials are identified in this report in order to specify adequately the experimental procedure. In no case does such identification imply recommendation or endorsement by the National Bureau of Standards, nor does it imply that the material or equipment identified is necessarily the best available for the purpose.

Phosphides and Sulfides

A number of phosphorous rich transition metal phosphides and layered transition metal sulfides have been reported to possess some range of stability and hydrogen oxidation activity in sulfuric acid. We are working on the extension of these results to phosphoric acid, and on determining the electrochemical properties of related compounds which can be prepared in similar ways, particularly intercalated compounds of the layered species. We are currently engaged in efforts to fabricate such compounds, most of which are not commercially available (studies of some commercially available phosphides and sulfides which were found unstable or inactive have been described in earlier reports of this series.) So far we have concentrated on phosphides, particularly MoP and FeP₂. Our first approach was to isolate the metal and red phosphorous in stoichiometric proportion in evacuated quartz ampoules. The sealed ampoules were heated for 2 hours at 550°C. X-ray diffraction studies of the products showed that the Mo and P were unreacted, and the Fe and P reacted to form an unidentified product of complex diffraction pattern which reacted slowly with H₃PO₄ and proved inactive for H₂ oxidation. In the second attempt, we tried to produce the compound MoP₂ by reaction of the metal with Ca₂P₃. The reactants were mixed, placed in a Ta crucible, and induction heated in vacuum for 2 hours at 600°C. The product was washed in 0.1N HCl to remove Ca, with careful venting and burning of gaseous products to remove any poisonous phosphine produced. The product appeared to be acid stable, but was inactive for H₂ oxidation. It had a complex x-ray diffraction pattern, not containing those of Mo or MoP₂. We are currently setting up a third preparative method, in which metal and

metalloid are independently heated, the metal to a suitable reactive temperature and metalloid to vaporization. Both are placed in a stream of inert carrier gas, the metalloid upstream of the metal.

Introduction

The advent of the microprocessor (μ P) [5] has opened up a relatively low cost approach to digital techniques for control and data handling in the laboratory. Although somewhat limited in throughput and "number crunching" ability (as compared to minicomputers), these devices are more than adequate for many applications in instrument control.

For our purposes, the device is considered as a Central Processing Unit (CPU) on a single chip capable (at maximum speed) of handling 250,000 instructions per second (estimated by utilizing an average of 2 bytes per instruction with 2 cycles per byte at a clock rate of 1 MHz). With the addition of suitable input-output interfaces and peripherals and of memory [both Read-Only-Memory (ROM) and Random-Access-memory (RAM)], a microcomputer is constructed. By the use of appropriate Digital to Analog Converters (DAC) and Analog to Digital Converters (ADC) we can interface this microcomputer with analog instruments for operational control and data acquisition.

The primary goal of this work was to design and implement a relatively low cost control package to be utilized with a standard laboratory potentiostat. The bulk of this paper is concerned with the implementation of this concept for the operational control of and data acquisition from a potentiostat used in electrochemical measurements. However, the System Use Section will be concerned with some planned uses of the equipment.

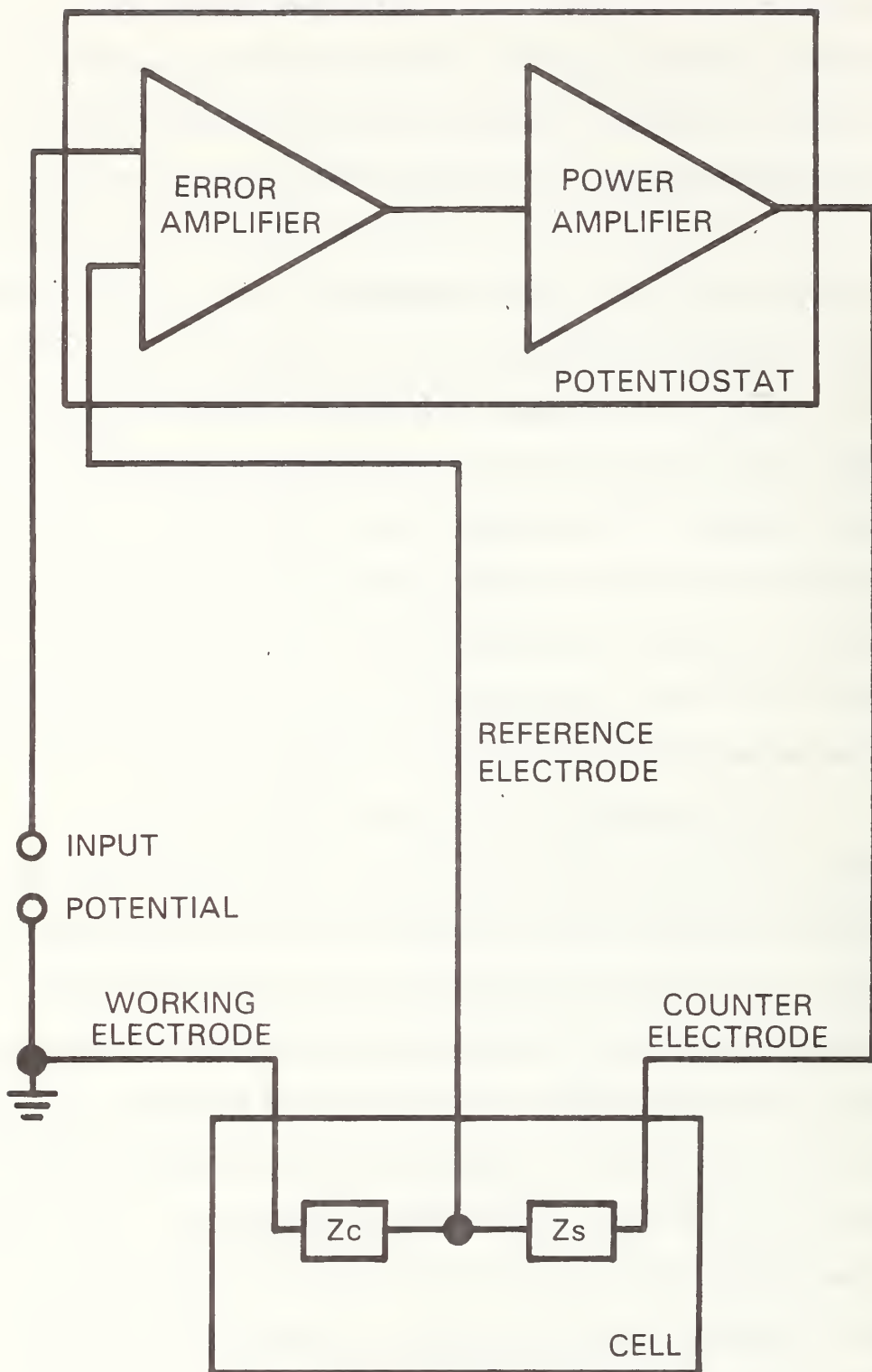
The Potentiostat

A potentiostat is an electronic device used by an electrochemist to control the potential of a cell in an accurate predetermined manner. The primary quantity that the electrochemist measures is the current as a function of the potentiostatically controlled cell potential and the rate of change of that potential. The cell potential, of course, varies with the input voltage which may be either AC or DC. The waveshape and frequency response are governed by the characteristic impedances of the overall system.

It is useful at this point to review the characteristics of a Potentiostat[6] for the purpose of defining the factors that must be controlled by the microcomputer. The instrument can be modeled (Fig. 5) as two amplifiers, one an error amplifier and the other a power amplifier. The electrochemical cell with which the potentiostat is used can be represented by the impedances Z_s and Z_c (for simplicity we assume that the cell contains only resistive components). Z_s is the series impedance in relationship to the counter electrode, the cell electrolyte and the current leads, while Z_c is the impedance between the reference electrode and the working electrode (sample) across which the potential is developed that is to be controlled by the potentiostat. The operation of the system can be outlined as the comparison of the potential across Z_c with some input potential, amplification of the resulting difference signal and application of this amplified potential to the cell. The resulting current changes the potential across Z_c and the process continues until the difference signal is essentially zero.

Basic Experimental Set-up and Design Criteria

A very common experimental arrangement consists of a motorized potentiometer used to generate an input potential which varies linearly with time (ramp or triangular waveshape) as input to the potentiostat. The output of the instrument is the Cell current which is plotted against cell potential on an X-Y recorder. Going beyond this experimental minimum, we find varying arrangements for input and output. The source potential is generated by oscillators, stepping-motor-driven sources, pulse generators, etc. These circuits allow the use of DC, ramps, stepped sweeps, waves, (sine, square and triangle), and pulse inputs. Compensation for changes in potentials due to IR drop across the cell's internal impedance is often added. Output data is often acquired by 2 pen recorders, logarithmic recorders, digital voltmeters, etc.



5. Block diagram of potentiostat and cell.

From this, we see that ideally, a digital control system for potentiostatic measurements should be capable of generating DC and AC potentials whose waveform must be easily controlled. Data acquisition should be high speed and the data should be of high resolution. The output of the acquired data must be flexible in format. To be useful, the instrument must be able to make at least simple computations using the acquired data so that results will be in the most desirable form.

Additional operational requirements can be imposed. The equipment should operate unattended (except for start-up), and must be able to terminate the experiment according to criteria established by the operator. If the device cannot perform the required data analysis by itself, it must have provision for communication with a larger machine. Finally, operation and programming of the instrument must be relatively simple and fast.

All of these functions can be performed by a system consisting of appropriate DAC's and ADC's combined with a digital computer. A minicomputer dedicated to this purpose would be under-utilized and was therefore not considered. The use of a communication line to a central computer with dedicated hardware at the instrument was considered but not used since cost estimates indicated it would be essentially no cheaper than the use of a microcomputer. A desk calculator could be used but is more expensive.

The Microcomputer [7]

The system designer must first evaluate the trade-offs necessary to determine which microprocessor (NP) matches the application best. Many factors enter into this decision and they must be carefully evaluated before proceeding. We have stressed the following:

1. Word size - The word length of a microprocessor at the present time can be 4, 8, 12, 16 bits, etc. In general, the power of the unit increases with increasing word length, but so does the overall system cost.

2. Speed - The speed of a μ P is not only a function of clock frequency, but also depends upon other factors such as the instruction cycle and the instruction set.
3. Instruction set - In general, the larger the instruction set, the more powerful the device. We must note, however, that in some cases, a device may require special instructions for a function (e.g., input-output instructions) that are not needed by other devices.
4. Chip family - This factor is of great importance to the researcher. A well integrated and compatible set of circuits that reduce the time and effort necessary for design and construction of a system can more than offset other factors.
5. Available software - If we examine the overall costs of a system, programming is by far the most expensive element. If a body of software already exists, then the overall expense of the system is effectively reduced.
6. Available hardware - Obviously, the less time and effort taken from the researcher for design and construction, the better. New devices and much new hardware are appearing all the time and the designer should be alert.

Details necessary for evaluation of many of these factors are available from the μ P manufacturer's data sheets. The relative importance of each factor is dependent upon the particular project, the potentiostat used and the individual designer.

Our choice was the 6800 Microprocessor.[8] It is an 8 bit device, with a clock frequency of up to 1 MHz and a minimum instruction time of 2 cycles. It has a reasonably extensive instruction set with several addressing modes giving great flexibility. Peripherals are treated as memory locations, thus requiring no special instructions. (This is probably the most important

reason for selecting the 6800. This feature, desirable for the potentiostat, is not, in general, found in other microprocessors at similar cost). The accessory chips are appropriate allowing relatively simple and easy access to peripherals with a minum of design. Although the available software is not as extensive as that available for the 8080 microprocessor (Intel Corp.) it is adequate for our purposes. There is a considerable variety of peripheral hardware available for microcomputer systems based on the 6800 μ P, enabling the designer to add on functions to his system with minmal problems of design and construction.

The 6800 based microcomputer we have constructed is based on the manufacturer's evaluation board, [9] which has been somewhat modified. This board provides the microprocessor with its support circuits (clock, gating circuits, etc.). It also provides interface adaptors for 3 peripherals [2 parallel using Peripheral Interface Adaptors (PIA) and one serial using an Asynchronous Communications Interface Adaptor (ACIA)]. One of the parallel ports is dedicated to communication with a teletype or low speed RS-232-C device. (A detailed discussion of all the circuit boards will follow later on in this paper). In our system, communication with a central computer, if desired, is provided through a terminal with a modem and an acoustic coupler. However, if we wish, data can be recorded on cassette tape at the terminal (at 30 to 120 characters per second) for later processing by the central computer.

The rest of the microcomputer consists of 5 circuit boards. There are two 8196 byte (one byte equals an 8 bit word) RAM boards, one converter (DAC's, ADC) and timer board, one board for signal distribution, and one variable speed serial interface board. The two memory boards feature data buffers and fully decoded address circuitry and include switching operations to place their base address at any 4K boundary in the address field. The variable speed, serial interface provides interfacing for RS-232-C communication levels at 8 speeds ranging from 10 characters per second to 960 characters per second.

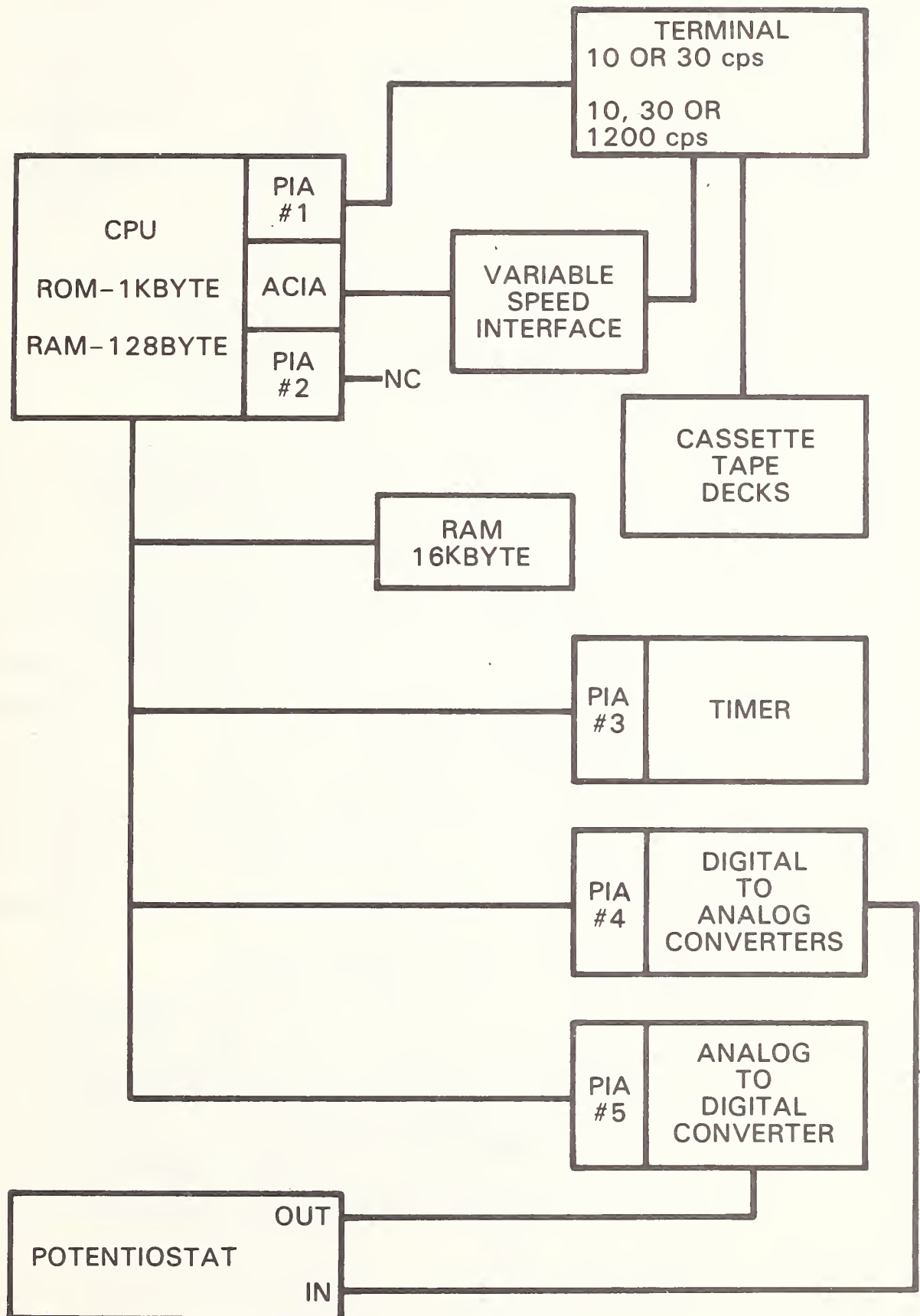
The converter and timer board contains three PIA's with interfacing, one of which is dedicated to a programmable timer. This has a range of microseconds to 40 minutes per timing point and generates an interrupt signal at the conclusion of the period. A second PIA is dedicated to two 10 bit digital to analog converters which have an output range of -5.12 to +5.11 volts. The third PIA interfaces with a 10 bit tracking ADC.

The signal distribution board provides connection points for input and output to the potentiostat or other device. Of the two DAC outputs one is normally connected to the input potential point on the potentiostat. The other output is connected to a voltage controlled oscillator (3×10^{-5} to 3×10^6 Hz). There are three ADC connectors. One provides an output of the analog voltage generated by a DAC which output is subsequently compared with the input (identified in Fig. 16 as ECHO), while the other two connectors are inputs which are connected thru a switch to a precision voltage clipper (discussed below). The output of the clipper provides the input to the ADC. These two inputs have a common return. (One of these inputs carries the full signal, while the other input carries half of this potential).

Communication between operator and equipment occurs via a Teletype or RS-232-C interface to a terminal. There is a monitor program in the ROM which obviates the need for panel switch programming. In fact, the only switches needed (other than power on) are a reset and communication speed set switch. Power requirements are +5V @ 6A, +15 V @ 50 mA, and +12 V @ 100 mA. A small cooling fan is necessary if the microcomputer is enclosed in a cabinet. Figure 6 shows the overall block diagram of the system.

Board-by-Board Details

The CPU of the microcomputer is a somewhat modified version of the manufacturer's evaluation board #1. The original board was designed to be a stand-alone unit with limited memory. Addressing is redundant and expansion of the memory is possible only by removing the redundancy. This is easily accomplished by removing all memory from the evaluation board except



6. Block diagram of complete system.

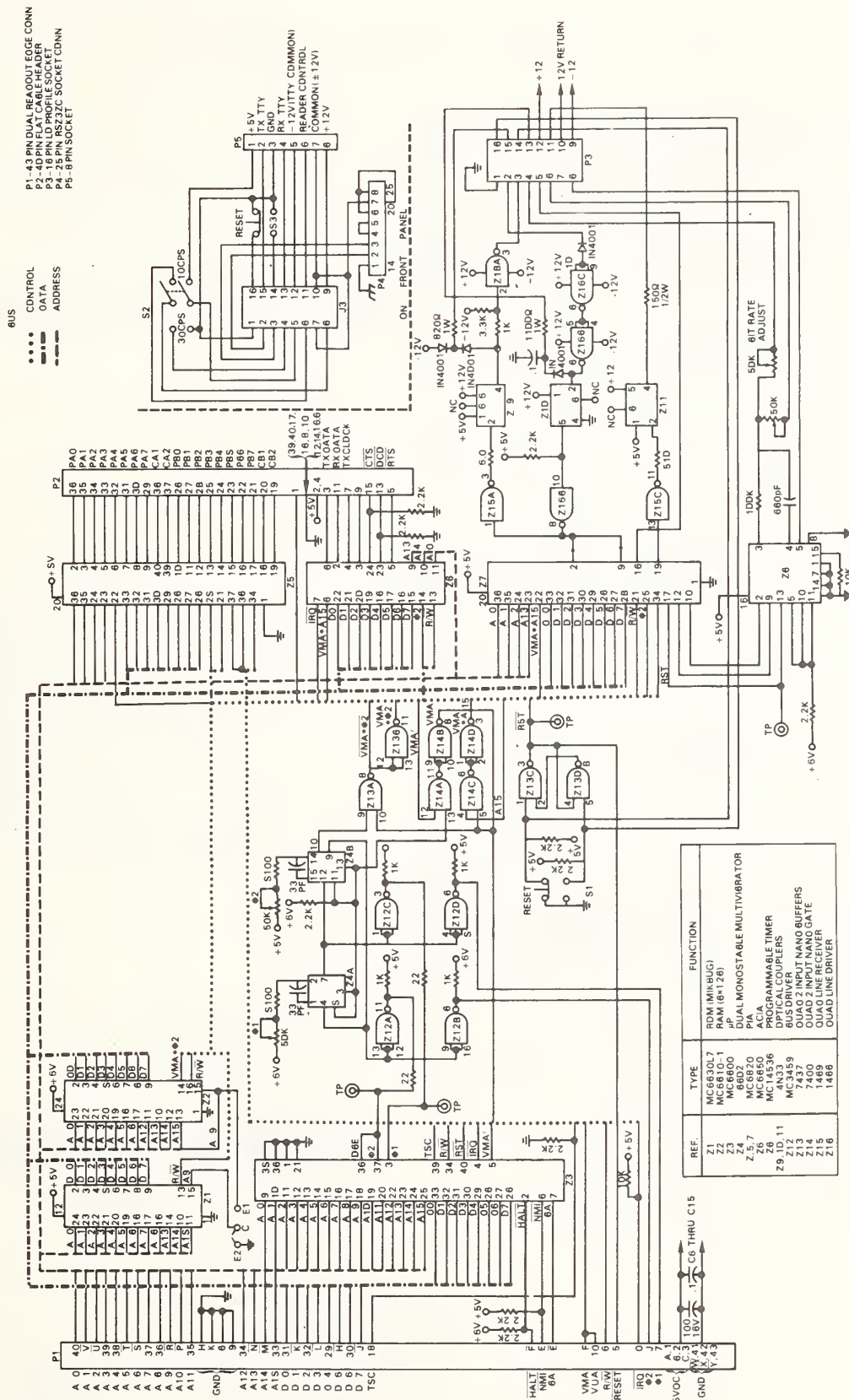
for the monitor ROM (address E000 hex) and its associated scratch-pad RAM (address A000 hex). An additional redundancy exists for the peripheral addresses. Since it is desirable for the peripheral addressed to be separated from main memory, we added an address line to the scratch pad enabling several blocks of addresses in the memory region that is identified by Axxx hex. An additional line was run from the PIA used for a low speed terminal. This line allows switch selection of 10 or 30 character per second operation. A schematic of the resulting board, including only operational circuits, is shown in Fig. 7. A map of available memory is shown in Fig. 8.

The monitor ROM (MIKBUG*), which is included in the evaluation kit, allows for loading from and generating of tapes, displaying and changing the contents of memory locations, displaying the contents of the primary registers and entering a user written program. Since most of the commercially available software is written using MIKBUG subroutines for control of input and output, we have retained it. Although limited in scope, it is adequate for our purposes.

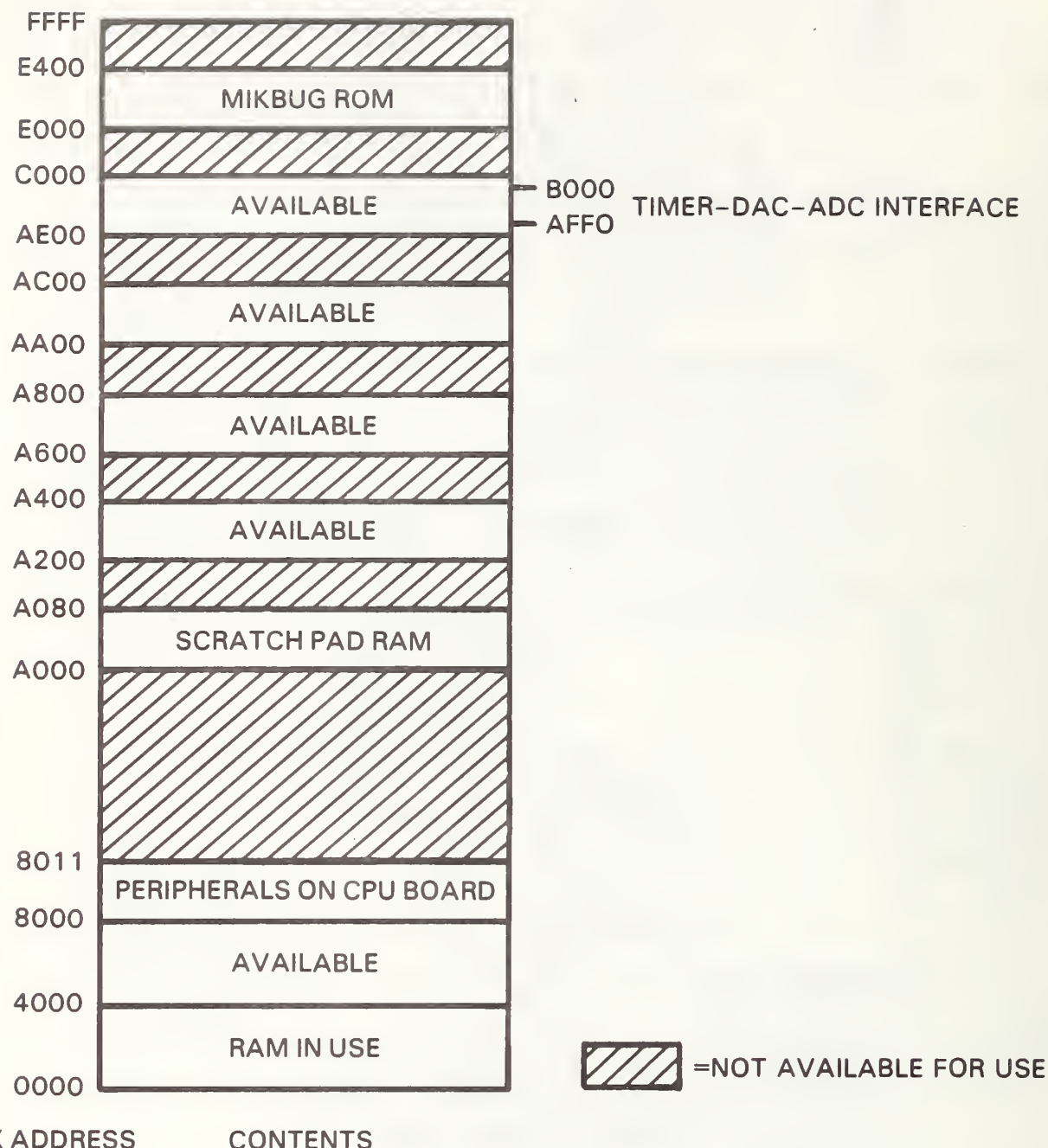
The 2 phase multivibrator clock oscillates at a frequency of 1 MHz for operation of the microcomputer. Three buses (data, address and control) are brought out through a dual 43 pin edge connector. As previously mentioned, there are 3 on-board peripheral adaptors. One of these adaptors (a PIA) is reserved to interface with a planned addition of a floppy disc unit.

The 8K memory boards (Fig. 9) are based on 1024 x 1 bit static memory Integrated Circuits (IC). These memories have access times of 500 nanoseconds (nsec) or better. Address and data lines are buffered and base address selection is made by means of a hexadecimal coded switch. Connection to the bus is via a dual 43 pin edge connector. Only one board contains the Poweron Reset [10] circuit shown in Fig. 9.

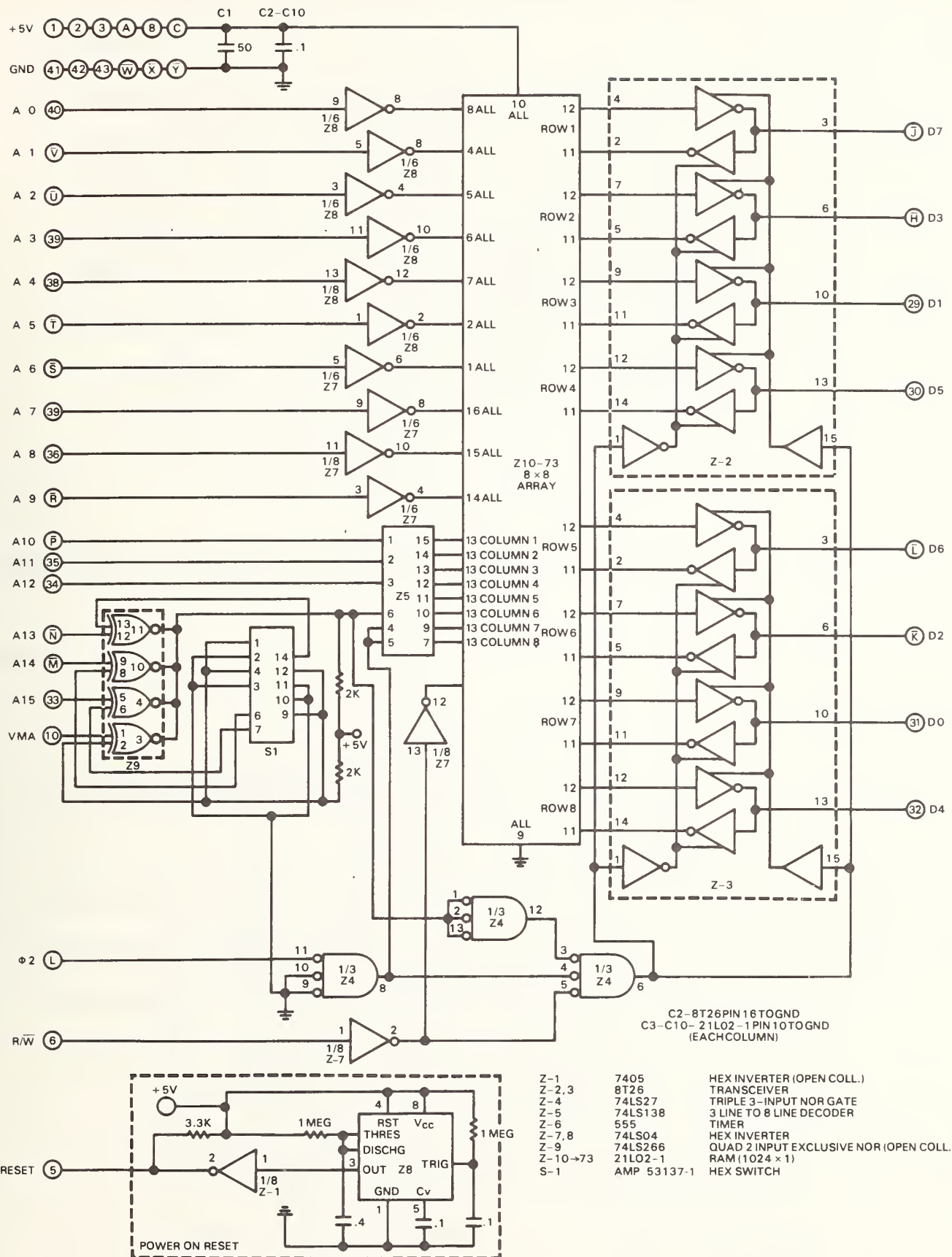
*Registered Trademark Motorola (Firmware ROM program)



7. Schematic of CPU Board as modified. Also shown are components mounted on front panel.



8. Memory map of system.



9. Schematic of 8 kilobyte RAM Board. Also shown Power-on Reset circuit which is included on one RAM Board only.

Figure 10 is a schematic of the variable speed interface together with the low speed terminal connections. RS-232-C interface connections are shown for mating with an Automatic Send Receiver (ASR) terminal that has the capability for 120 characters per second operating speed when recording or playing back with its built-in cassette tape drives. If desired, data rates other than those shown can be obtained through the use of the MC 14411 bit rate generator. [9,12] These data rates can be achieved by wiring pins 22 and 23 (Rate Select B and Rate Select A) according to Table 2 or by connecting them to a peripheral interface and programming them. There are also 8 other speeds directly available from the chip at any rate select configuration. (Note that the output frequency for each of the positions is found by multiplying the characters/sec by 160).

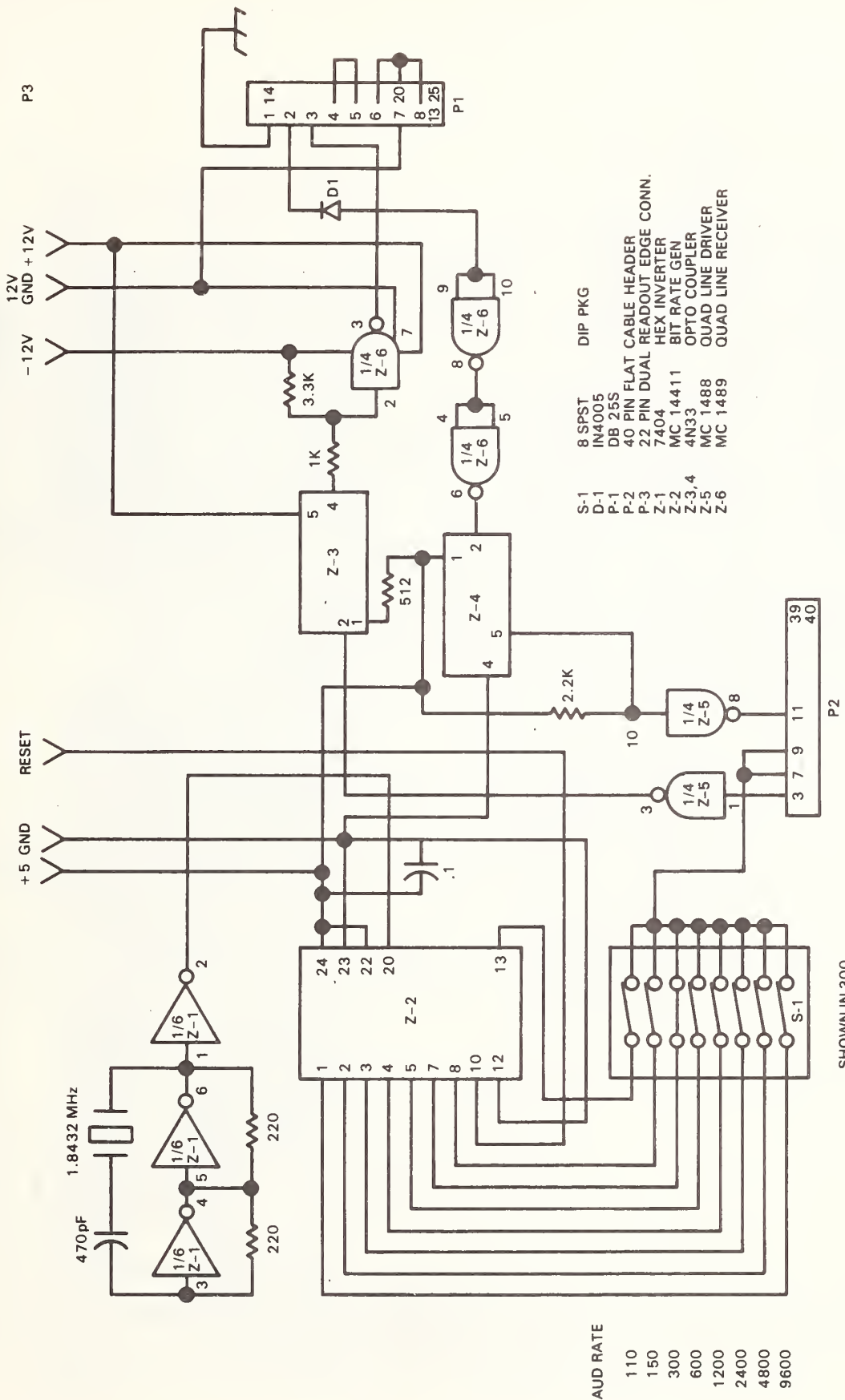
Table 2. Data Clock Rate Selection

Rate Multiplier	Rate Select A Connection	Rate Select B Connection
X1	0	0
X8	1	0
X16	0	1 (present connections)
X64	1	1

where: 0 = GND
1 = +5V

The timer-converter board schematics are shown in Fig. 11 through Fig. 15. The interval timer [11] section (Fig. 12) is software programmable and runs off the system clock (1 MHz). Thus, its accuracy is dependent upon the stability and frequency of that signal. Since we are not using a crystal controlled oscillator the stated set times must be considered to be nominal values. At the present time, they are sufficiently precise for our application. Installation of a two phase crystal controlled clock is not difficult and can be done when necessary.

The setting of the time interval is done in two steps. First a code, defining which output from the 7490-74452 decade divider chain is to be fed to the presetable counter (74455), is loaded, via the PIA A side, into the 9312 multiplexer. Then, the 74455 is preset with the number of counts desired (0-256) from the B side of the PIA, and counting (down count)



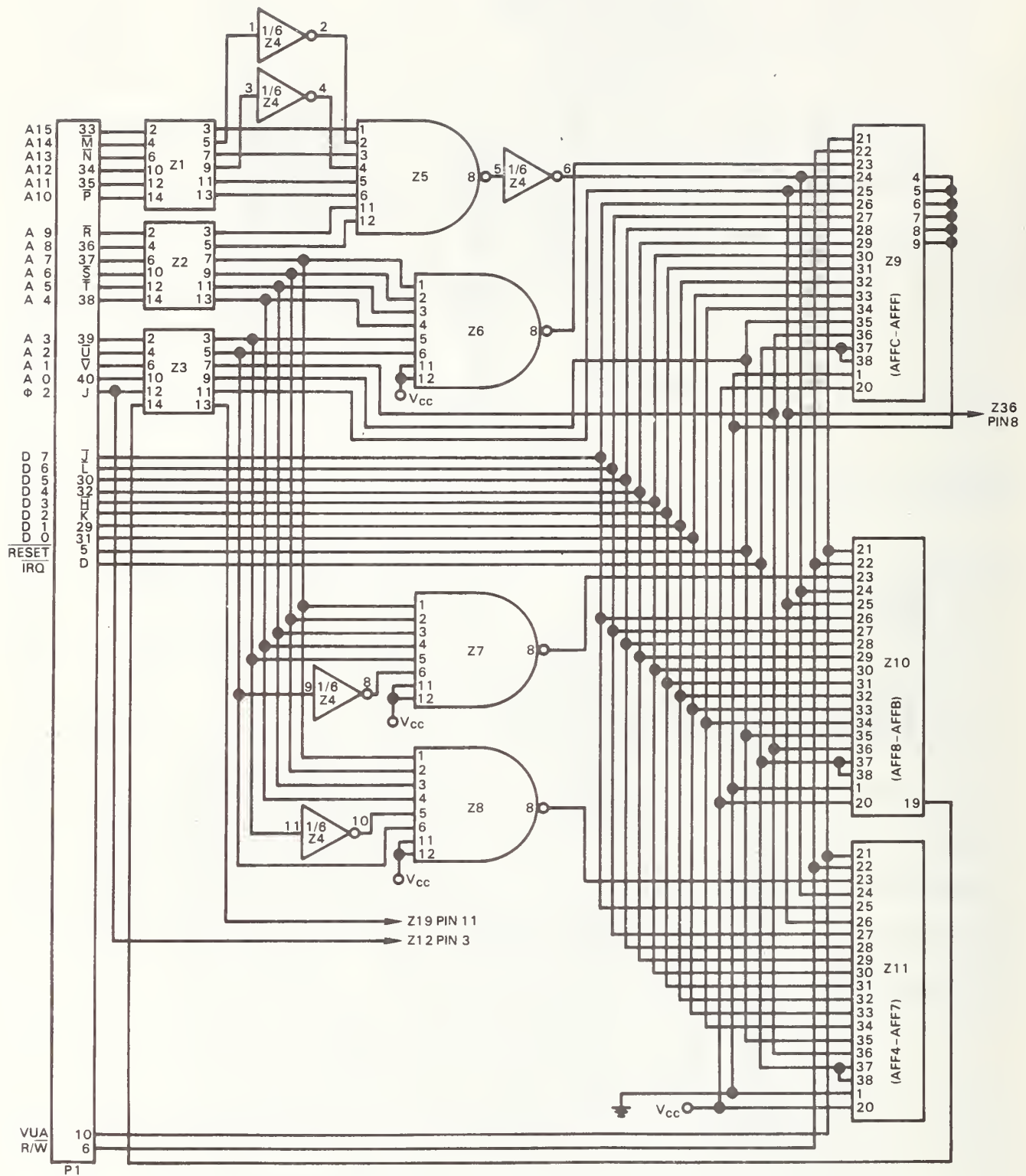
Baud Rate

110 150 300 600 1200 2400 4800 9600

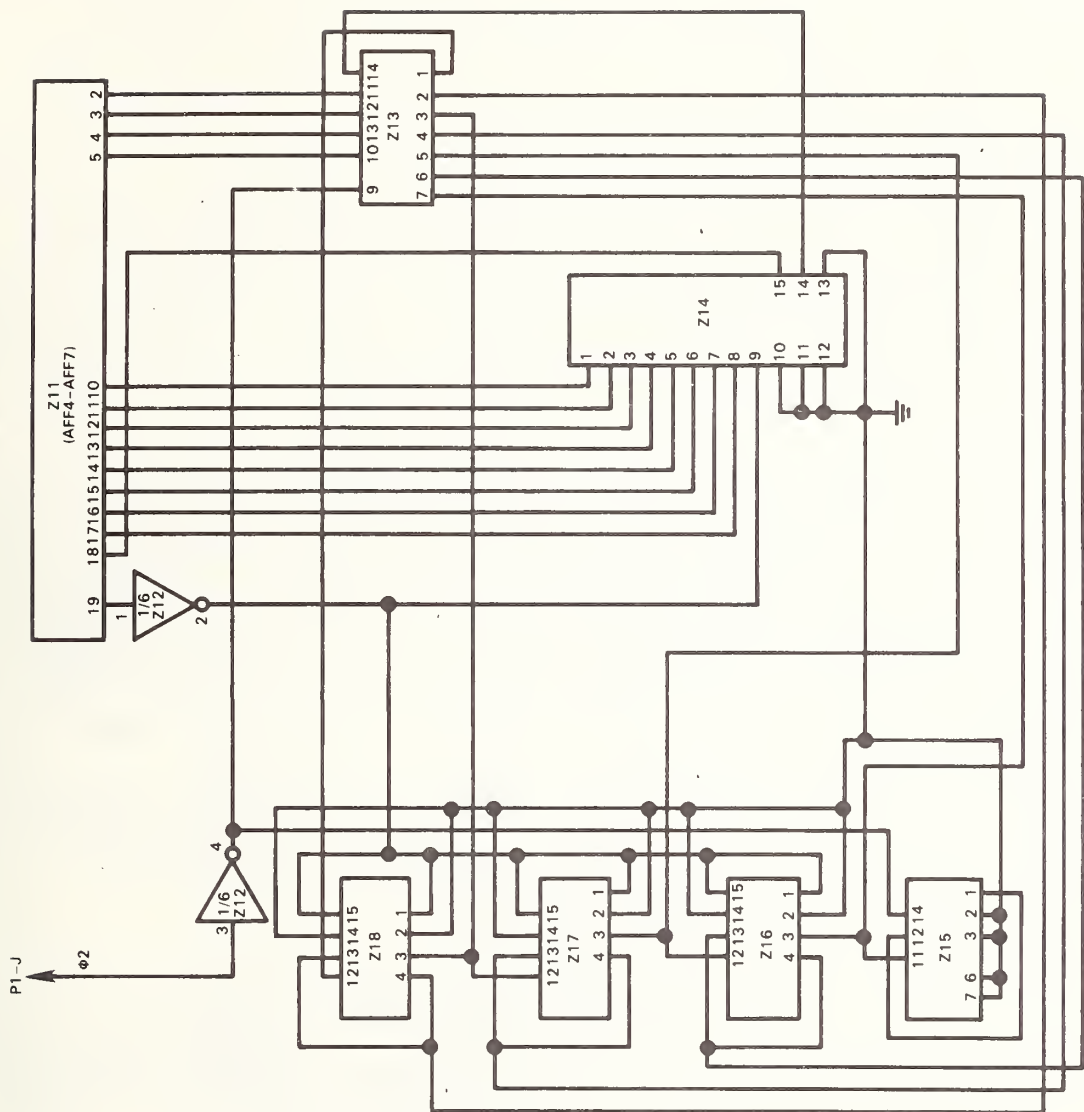
SHOWN IN 300 BAUD POSITION

P2

10. Schematic of Variable speed serial interface.



11. Schematic of Timer-Converter Board: Address decoding system.



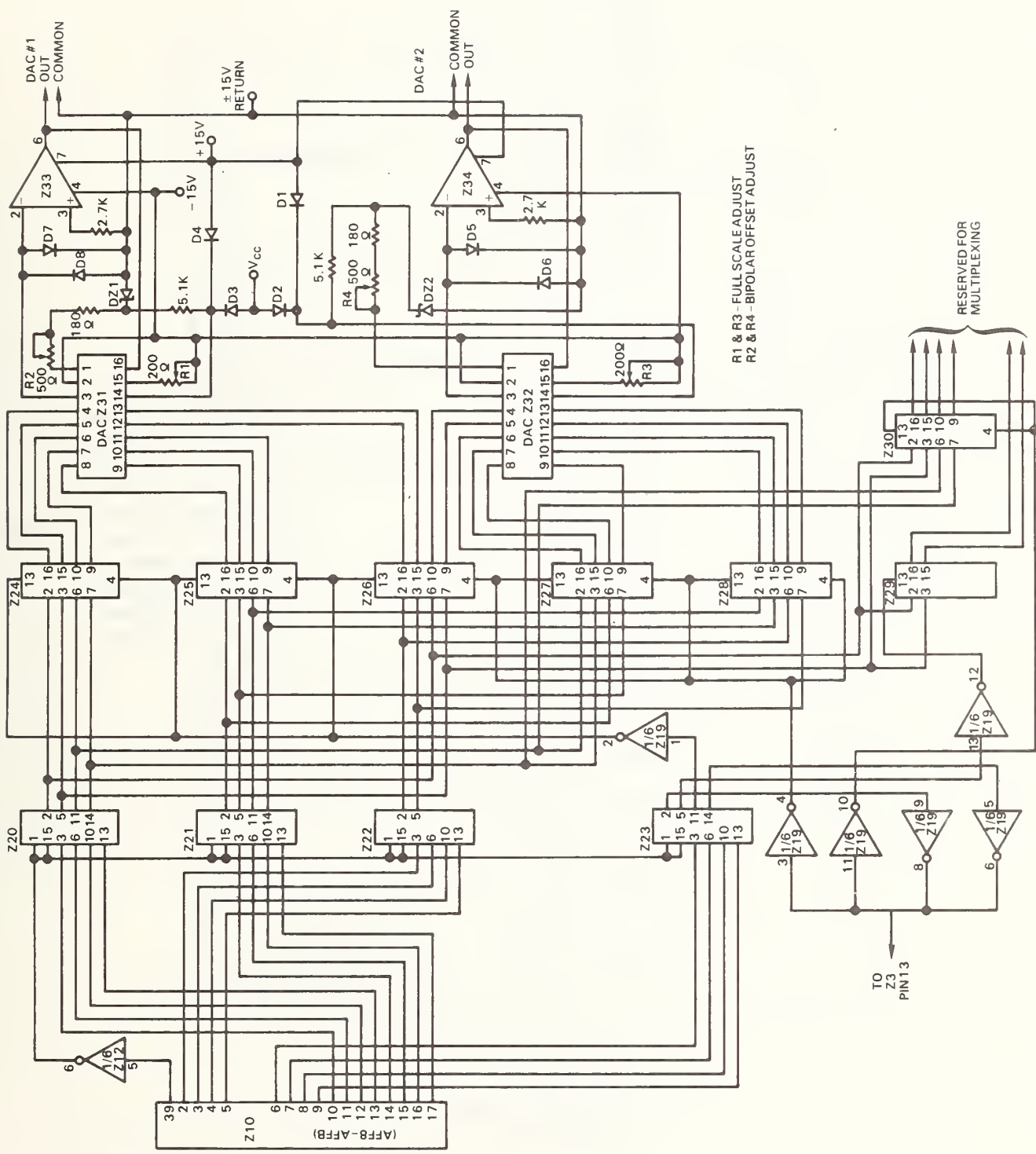
TIMER-CONVERTER COMPONENTS			
REF.	TYPE	FUNCTION	
Z1,2,3	8T97	BUFFER	
Z4,12,19,45	7404	INVERTER	
Z5,6,7,8	MC6820	8 INPUT NAND GATE	
Z9,10,11	9312	PIA	
Z13	MC74455	MULTIPLEXER	
Z14		BINARY UP/DOWN COUNTER	
Z15	7490	DECade COUNTER	
Z16	MC74452	DUAL DECADE COUNTER	
Z20,21,22,23	8T24	BUS TRANSCIEVER	
Z24,25,26,27,	7475	4 BIT LATCH	
Z28,29,30			
Z31,32,35	DAC-100	10 BIT DAC	
Z33,34,40	741	OP AMP	
Z36,37,38	MC2824	BINARY UP/DOWN COUNTER	
		FLIP-FLOP	
Z39	7474	VOLTAGE COMPARATOR	
Z41	CMP-01		
Z42,43,44	7408	2 INPUT AND GATE	
Z46	7432	EX OR GATE	
D1-12	IN914	DIODE	
D1-13	IN754	ZENER DIODE	

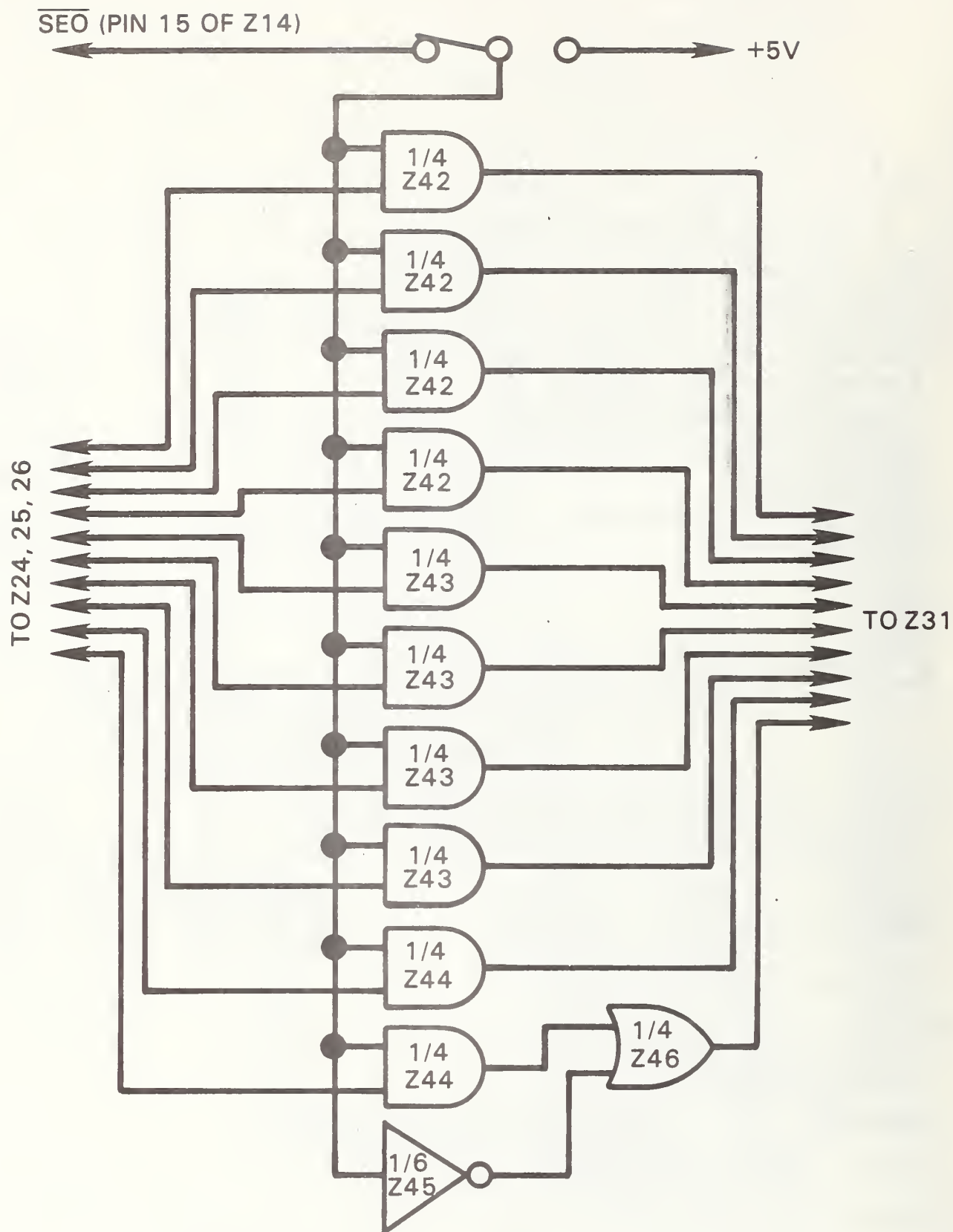
12. Timer-Converter Board: Timer section.

is started. When the desired number of timing pulses has been counted, the 74455 puts out an interrupt pulse to the CPU. The minimum interval time for the timer is 1 microsecond (μ sec). The maximum interval is 42.6 minutes. However, the maximum repetition rate is dependent on the interrupt handling routine in the microprocessor. We have not directly determined this elapsed time for the shortest program but estimate it to be on the order of 30 μ sec. The program we are using takes on the order of 250 μ sec. As will be shown, this places a lower limit on the effective pulse time period for the input to the potentiostat.

There are two identical DAC's (Fig. 13) on this board. [13] Under program control, each one can be independently loaded from the PIA utilizing the 7475 latches. As presently formatted, the input to the DAC remains the same until changed by the CPU. Thus, the output of the DAC, which is fed to the potentiostat, remains at a constant level until the next value is placed on the latches. For our purposes this is satisfactory. A simple addition of circuitry (shown as Fig. 14) will remove this feature and allow the input pulse width to the potentiostat to closely follow the timer period.

As a check on performance, a program for generating a triangle wave (in steps of 10 millivolts (mV)) was written. An effort was made to minimize program steps. When run, this program generates a DAC output triangular wave of 25 Hz. The time per point works out to be 20 μ sec. From this we can estimate that a waveform generated from a lookup table would take about 50 μ s per step (based on a minimum number of instructions). It is obvious that were we to generate individual points of a waveform and use them individually, as generated by the program, we would have much longer times per point. Pulses of variable duty cycles would be limited in repetition rate by the interrupt handler (see timer discussion) to about 30 μ sec, although "on" time could be adjusted by the technique discussed before (Fig. 14 and text of previous paragraph).



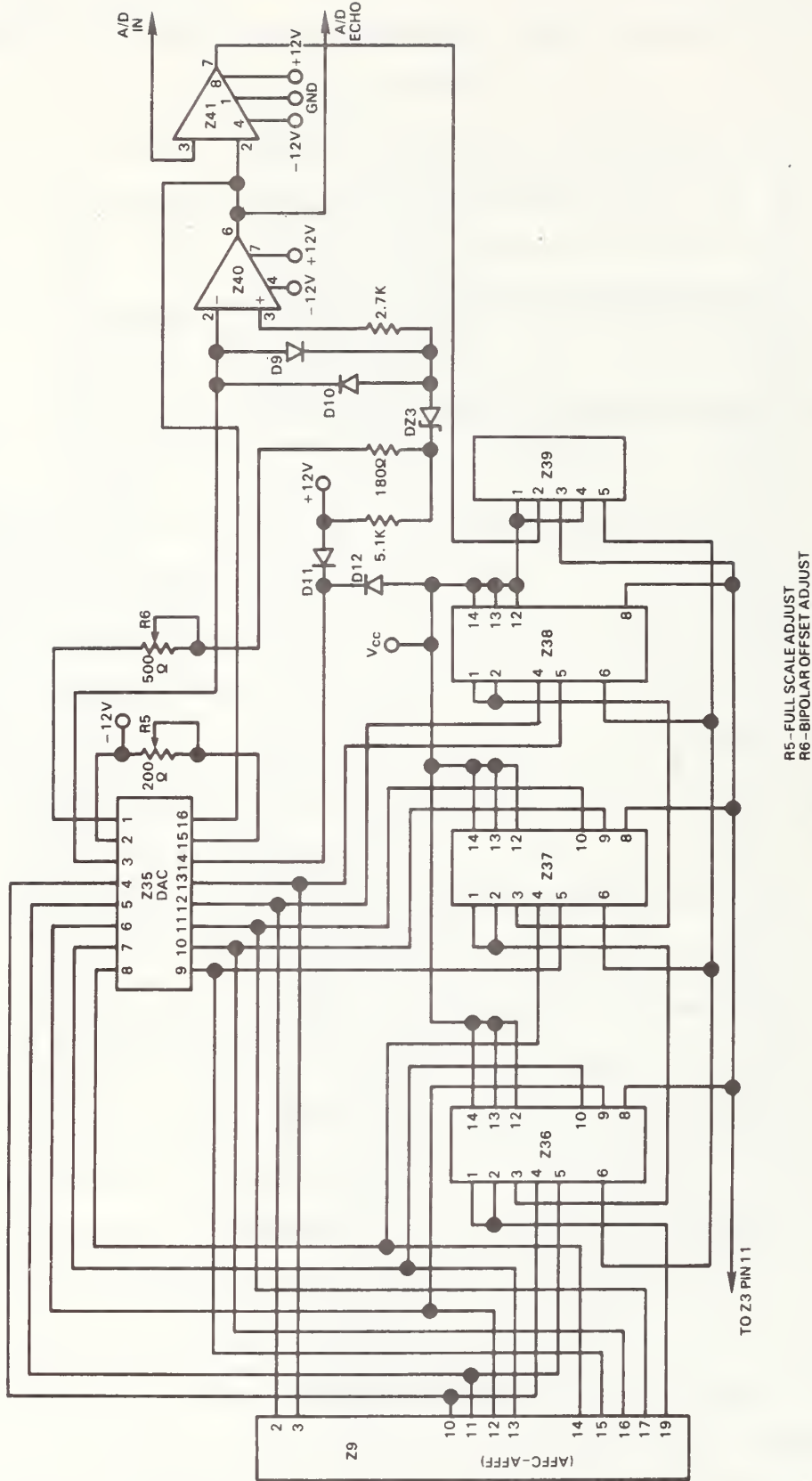


14. Timer-Converter Board: modification to DAC section proposed for Interrupt-Triggered return to zero output.

Repetitive waveforms of normal complexity (sine, square, triangle, ramp) for input to the potentiostat can be generated under program control in an alternative manner. The output of one of the DAC's can act as input for a Voltage Controlled Oscillator (VCO) (the VCO we use has a frequency deviation range of 30 μ Hz to 3 MHz) allowing program selection of output frequency. The inverted CB₂ output of the timer PIA is used as a trigger signal for the VCO. This oscillator puts out one cycle of the selected frequency when triggered. Since peak-to-peak voltage, offset voltage, and starting phase are all controllable, we have considerable flexibility for the generation of waveforms.

One final comment is in order. The DAC section of the board contains logic for limited multiplexing (although not fully implemented) of the input and output signals. With the installation of some reed relays we can choose between two distinct analog sources and simultaneously between four outputs. Some minor circuitry changes would allow all of these lines to be dedicated to some other arrangement of signals or to extend the multiplexing range.

The ADC section (Fig. 15) of the board reflects some major compromises that were made after careful trade-off considerations of system speed requirements and costs. Ideally, the analog to digital converter would have a resolution of one millivolt or better and would acquire the data in one μ sec or less. Such a device is not feasible at this time. Examination of the experimental needs allows relaxation of these requirements particularly in the area of high-speed operation. The experiment as planned calls for the input to the potentiostat to be stepped through a cycle in which the input potential is changed by a fixed value, and then sustained for a period of time. At this time the current is measured and after this reading the cycle is continued. As indicated in the timer discussion the fastest rate at which the input can be changed is 30 μ sec (or 33.33 kHz). This establishes an upper limit on the required operating speed. Resolution requirements can be minimized by amplification of the input signal (preferably under program control. In our case, automatic amplification is not performed, our choice being a manual change in output amplification on the potentiostat). In addition to the factors already noted, cost and circuit complexity are vital considerations.



15. Timer-Converter Board: ADC section.

R5 - FULL SCALE ADJUST
R6 - BIPOLAR OFFSET ADJUST

We should also note here that the output current from the potentiostat (our analog signal source) will often be slowly falling with time due to the charging of the reactive components of the cell. It is desirable for the ADC to follow this fall closely. (When this exponential fall-off has reached a quasi-constant level, a "steady state" condition has been reached in the cell, and this is a region of interest).

After weighing all these points, we decided to use a 10 bit tracking ADC (also known as counter-ramp ADC). [14,15] This type of ADC is normally thought of as a "slow" converter, since the time to acquire the signal is $(2^n - 1)$ times the step rate of the counter for full scale changes (n is the number of bits in the DAC component of the converter). In our case, this is about three milliseconds. However, this number is valid only for full scale excursions. For less than full scale the time is reduced by a factor proportional to the change in the number of counts needed. Indeed for a change in input potential of 100 mV (10 counts) the time is 30 μ sec. This is estimated for a step change. For a slow change the speed would be even better. The overall limitation on ADC conversion (for small analog change) rate is the conversion speed of the component DAC.

The tracking ADC converter follows the input potential continuously, and the digital output is always available. It is a relatively simple circuit [14] consisting of an up/down counter, a DAC, an amplifier, a comparator and a gate. We are using a 10 bit DAC that has a conversion rate of ~40 kHz. Our clock source for the counter is the CPU clock of 1 MHz. The ADC could be run at a maximum frequency of 2.5 MHz if desired. This would allow an ADC conversion rate of 800 Hz for full scale excursions and proportionally reduced times for small changes. OVERRANGING is a problem with this converter. If the input potential exceeds the full scale potential, the counter will continue to count indefinitely and the digital data will be in error. To avoid this, a precision voltage limiter

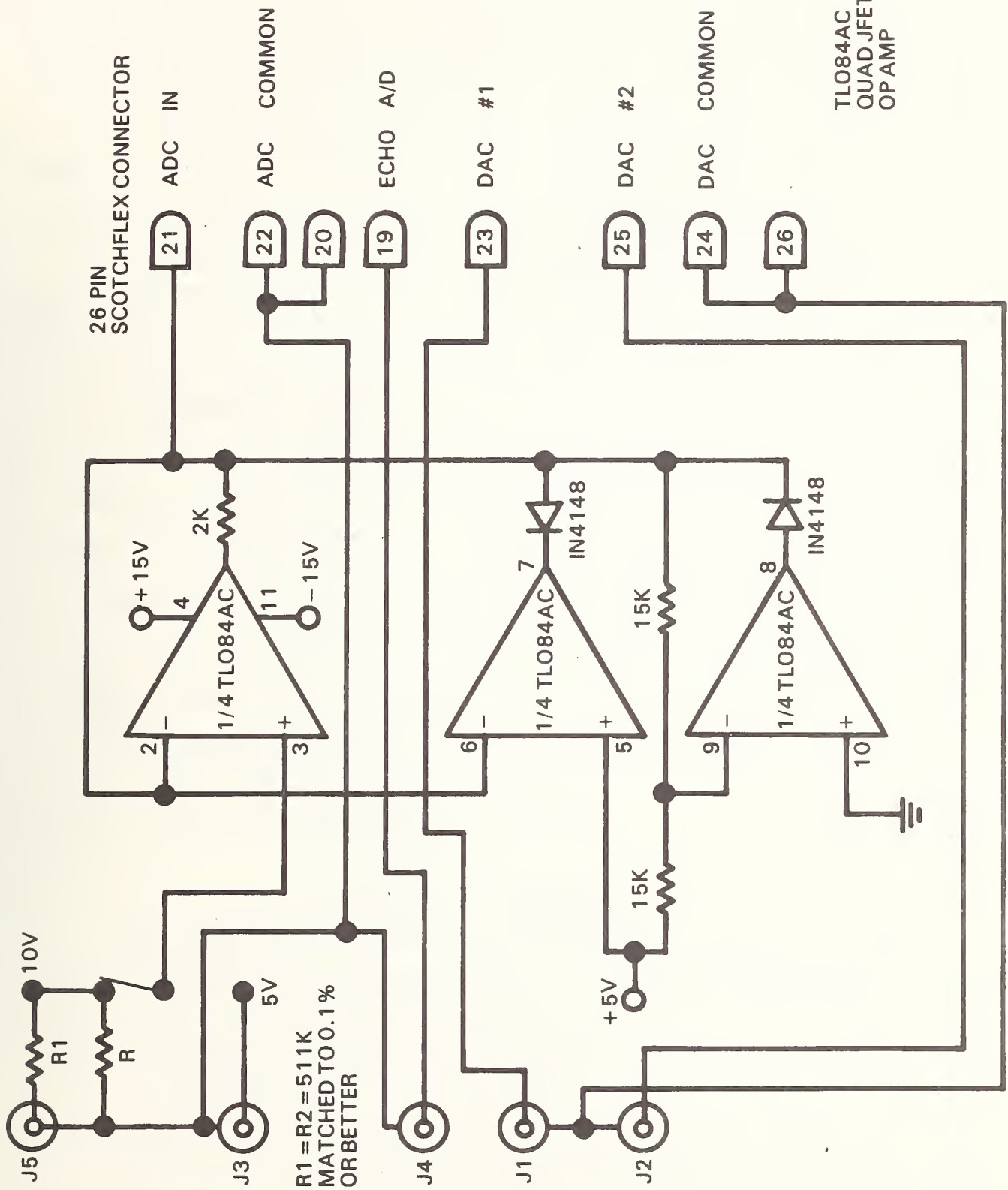
is employed on the input to the ADC. [16] This is physically located on the signal distribution board (Fig. 16) in close proximity to the potentiostat. The full scale input to the ADC ranges from -5 to +5 volts.

Programming [17,18]

To no one's surprise, initial programming is a major fraction of the time needed to develop an operating system. Fortunately, the commercial availability of a higher level language (BASIC) has reduced the size of this effort considerably. There are compromises needed, however, which must be carefully weighed.

Assembly language programming yields a more concise and faster running code than the use of a higher level language, especially when that language is implemented as an interpreter. Since relatively high speed data acquisition is an integral part of our experimental concept, alternatives to BASIC must be considered. Two approaches are immediately obvious. First, we can implement in hardware a Direct Memory Access (DMA) system. This would have the advantage of providing the fastest possible storage of data. However, flexibility would be reduced. The second approach (the one we adopted) would involve the calling of a machine language program as a subroutine while the overall program would be in BASIC. Under this concept, we would maintain the ease and flexibility of programming in a higher level language while maintaining reasonable data acquisition speeds. This requires that the BASIC program (written or purchased) include a command to call a machine language program, a means to return from that program and the ability to handle the data in the form generated by the data acquisition program. There are several commercial programs available (one of which we have acquired) [19] that satisfy these requirements.

For generation of machine language programs the use of an assembler is suggested. This can either be "resident" in the microcomputer or can be



available via time-sharing on a large computer (cross-assembler). An example of a cross assembled program is shown in Figure 17. This particular program is of interest since it is the data acquisition program we currently are using. Some comments are in order. First, this program utilizes only one of the two DAC's. Second, initial clearing of the data storage area is accomplished by the BASIC control program (automatically on RUN). Third, this is probably not the fastest possible program (as indicated earlier it uses about 250 μ sec per point). Fourth, proper organization of the BASIC program will enable this program to be utilized for signal averaging. For this purpose, the data storage allotted per point, limits the maximum number of sweeps to 63. Addition of one more byte of data storage per point would allow more data accumulation by allotting memory space for the addition of 256 more sweeps.

The required memory for the BASIC interpreter and the machine language program is approximately 8K byte. The BASIC control program and its required buffer memory takes an additional 4K byte leaving 4K byte for data storage. Since 4 bytes are required per point, only 1000 points can be stored without installing additional RAM. In the future, we expect to place these programs into ROM thereby freeing the 16K bytes of RAM for additional data storage. At present, however, they are recorded on cassette tape and are loaded into RAM when needed.

System Use

We have described the implementation of a microprocessor control and fast data acquisition system for use with a standard laboratory potentiostat. Figure 18 shows a result from one of the experiments we are conducting using this instrument. Using this as an example we can illustrate several features. First, we can accumulate digital data at selected rates. If we sweep at fast rates, the data can be plotted in a manner yielding the equivalent of a potentiodynamic scan. If we use long delay times per point - long enough for steady state to be reached -

LINE	ADDR	B1	B2	B3	E	DATA ACQUISITION	PAGE	1
1						RAM DATA ACQUISITION		
3						♦THIS PROGRAM OUTPUTS A POTENTIAL		
4						♦BETWEEN -5 AND +5 VOLTS FOR A		
5						♦FIXED TIME PERIOD, AT THE		
6						♦END OF WHICH, A POTENTIAL IS READ.		
7						♦THE UPPER AND LOWER LIMITS CAN BE		
8						♦SET EXTERNALLY, AS CAN BE THE		
9						♦STEP SIZE AND CLOCK PERIOD.		
11						ORG \$1EBF		
12	1EBF	1E	AF			CLKCT EQU \$1EAF HI=TIME/COUNT:LO=COUNTS		
13	1EBF	1E	B3			STEPL EQU \$1EB3		
14	1EBF	1E	B2			STEPH EQU \$1EB2		
15	1EBF	1E	B4			HILIM EQU \$1EB4		
16	1EBF	1E	B6			LOLIM EQU \$1EB6		
17	1EBF	1E	B8			DIREG EQU \$1EB8 0=DOWN:1=UP		
18	1EBF	1E	B9			TREG EQU \$1EB9 POINTER TO TOP OF DATA STACK		
19	1EBF	1E	BB			RREG EQU \$1EBB POINTER TO BOTTOM OF STACK		
20	1EBF	AF	F4			TIMER EQU \$AFF4		
21	1EBF	AF	F8			DAC EQU \$AFF8		
22	1EBF	AF	FC			ADC EQU \$AFFC		
23	1EBF	A0	00			IOINT EQU \$A000 INTERRUPT VECTOR		
24	1EBF	A0	14			TEMPR EQU \$A014		
25	1EBF	1E	BD			TREGW EQU \$1EBD		
26	1EBF	A0	16			INPEG EQU \$A016		
27	1EBF	A0	18			SREG EQU \$A018		
28	1EBF	1E	B1			SWEFP EQU \$1EB1 SAVE #OF SWEEPS		
30	1EC0	36				PSH A SAVE REGISTERS		
31	1EC0	37				PSH B		
32	1EC1	07				TPR		
33	1EC2	36				PSH A		
34	1EC3	FF	A0	16		STX INREG		
35	1EC6	BF	A0	18		STS SREG		
37	1EC9	7F	1E	B8		CLR DIREG SET DIRECTION, DOWN		
38	1ECC	FE	1E	B9		LDX TREG		
39	1ECF	FF	1E	BD		STX TREGW		
40	1ED2	BE	1E	B4		LDS HILIM		
41	1ED5	AF	00			STS 00,X LOAD LIMIT INTO T REGISTER		
42	1ED7	CE	AF	F4		SETUP LDW #TIMER SET UP PERIPHERALS		
43	1EDA	4F				CLRA		
44	1EDB	A7	02			STAR 02,X		
45	1EDD	A7	03			STAR 03,X		
46	1EDF	A7	06			STAR 06,X		
47	1EE1	A7	07			STAR 07,X		
48	1EE3	43				COMA		

17. a) Cross-assembled Data Acquisition Program

LINE	ADDR	B1	B2	B3	E	DATA ACQUISITION	PAGE	2
49	1EE4	A7	00			STAA 00,X		
50	1EE6	A7	01			STAA 01,X		
51	1EE8	A7	04			STAA 04,X		
52	1EEA	A7	05			STAA 05,X		
53	1EEC	86	04			LIAA #\\$04		
54	1EEE	A7	02			STAA 02,X		
55	1EF0	A7	08			STAA 08H,X		
56	1EF2	86	20			LIAA #\\$20		
57	1EF4	A7	03			STAA 03,X		
58	1EF6	86	30			LIAA #\\$30		
59	1EF8	A7	06			STAA 06,X		
60	1EFA	A7	08			STAA 08H,X		
61	1EFC	86	20			LIAA #\\$20		
62	1EFE	A7	07			STAA 07,X		
63	1F00	0E				DATAT CLI		
64	1F01	CE	1F	1C		LIX #SERV		
65	1F04	FF	A0	00		STX IDINT		
66	1F07	FE	1E	BD		LIX TREGW		
67	1F0A	AE	00			LIS 00,X		
68	1F0C	BF	AF	F8		STS DAC OUTPUT-ANALOG VOLTAGE		
69	1F0F	FE	1E	AF		LIX CLKCT		
70	1F12	FF	AF	F4		STX TIMER OUTPUT TIME PERIOD		
71	1F15	BE	A0	18		LIS SREG		
72	1F18	3E				WAI WAIT FOR INTERRUPT		
73	1F19	01				NOP		
74	1F1A	20	0F			BRA CONT		
75	1F1C	86	08			SERV LIAA #\\$08		
76	1F1E	B7	AF	F4		STAA TIMER STOP TIMER		
77	1F21	B6	AF	F5		LIAA TIMER+1 READ OUT TIMER		
78	1F24	FE	AF	FC		LIX ADC READ ADC		
79	1F27	FF	A0	14		STX TEMPR		
80	1F2A	3B				RTI		
81	1F2B	FE	1E	BD		CONT LIX TREGW		
82	1F2E	A6	03			LIAA 03,X RECALL PREVIOUS VALUE		
83	1F30	E6	02			LIAB 02,X		
84	1F32	BB	A0	15		ADDA TEMPP+1 ADD NEW VALUE		
85	1F35	F9	A0	14		ADC8 TEMPP		
86	1F38	A7	03			STAA 03,X STORE SUM		
87	1F3A	E7	02			STAB 02,X		
88	1F3C	A6	01			LIAA 01,X		
89	1F3E	E6	00			LIAB 00,X		
90	1F40	7D	1E	B8		TST DIREG UP OR DOWN?		
91	1F43	27	19			BEO DOWN		
92	1F45	B0	1E	B3		UP SUBA STEPL UP! THEN DECREMENT		
93	1F48	F2	1E	B2		SECB STEPH		
94	1F4B	A7	05			STAA 05,X		
95	1F4D	E7	04			STAB 04,X STORE NEW D-A DATA IN ◆NEXT LOCATION		
96	1F4F	FF	A0	14		STX TEMPR SAVE INDEX		
98	1F52	EE	04			LIX 04,X		
99	1F54	BC	1E	B4		CPX HILIM COMPARE NEW X TO UPPER LIMIT		
100	1F57	27	2D			BEO END GREATER? THEN GO TO END		
101	1F59	FE	A0	14		LIX TEMPR ELSE? RESTORE INDEX		
102	1F5C	20	17			BPA NEXT		

17. b) Data Acquisition Program (continued)

LINE	ADDR	B1	B2	B3	E	DATA ACQUISITION	PAGE	3
103	1F5E	BB	1E	BB		DOWN ADDA STEPL DOWN! THEN INCREMENT		
104	1F61	F9	1E	B2		ADCB STEPH		
105	1F64	A7	05			STAA 05,X		
106	1F66	E7	04			STAB 04,X STORE NEW X		
107	1F68	FF	A0	14		STX TEMPR SAVE INDEX		
108	1F6B	EE	04			LDX 04,X		
109	1F6D	BC	1E	B6		CPX LOLIM COMPARE NEW X TO LO LIMIT		
110	1F70	27	0C			BEQ REVER LESS? THEN TURN AROUND		
111	1F72	FE	A0	14		LDX TEMPR ELSE, RESTORE INDEX		
112	1F75	08				NEXT INX		
113	1F76	08				INX		
114	1F77	08				INX		
115	1F78	08				INX		
116	1F79	FF	1E	BD		STX TREGW SAVE NEW POINTER		
117	1F7C	20	82			BRA DATAT NEXT POINT		
118	1F7E	7C	1E	BB		REVER INC DIREG CHANGE DIRECTION		
119	1F81	FE	A0	14		LDX TEMPR		
120	1F84	20	EF			BRA NEXT NEXT POINT		
121	1F86	FE	1E	BD		END LDX TREGW SAVE POINTER TO LAST DATA *POINT		
122								
123	1F89	08				INX		
124	1F8A	08				INX		
125	1F8B	08				INX		
126	1F8C	08				INX		
127	1F8D	FF	1E	BB		STX RREG		
128	1F90	FE	1E	B9		LDX TREG RESTORE ALL REGISTERS		
129	1F93	FF	1E	BD		STX TREGW RESTORE WORKING T REGISTER		
130	1F96	BE	A0	18		LDS SREG		
131	1F99	FE	A0	16		LDX IMREG		
132	1F9C	32				PUL A		
133	1F9D	06				TAP		
134	1F9E	33				PUL B		
135	1F9F	32				PUL A		
136	1FA0	39				RTS		
137	1FA1					END		

TOTAL ASSEMBLER ERRORS = 0

DATA ACQUISITION

PAGE 4

SYMBOL TABLE

♦ 1							
AID	AFFC	CLKCT	1EAF	CONT	1F2B	DAC	AFF8
DATAT	1F00	DIREG	1EB8	DOWN	1F5E	END	1F86
HILIM	1EB4	IMREG	A016	IOINT	A000	LOLIM	1EB6
NEXT	1F75	REVER	1F7E	RPEG	1EBB	SERV	1F1C
SETUP	1ED7	SREG	A018	STEPH	1EB2	STEPL	1EB3
SWEEP	1EB1	TEMPR	A014	TIMER	AFF4	TREG	1EB9
TREGW	1EBD	UP	1F45				

17. c) Data Acquisition Program (continued)

READY
#RUN
ELECTROCHEMICAL DATA TAKER VERSION 2

DATE
? 9/19/77
SAMPLE
? TI:TR
FULL SCALE CURRENT-MA
? 1
ENTER TIME/COUNT

CODE	TIME IN SEC
0	10E1
1	10E0
2	10E-1
3	10E-2
4	10E-3
5	10E-4
6	10E-5
7	10E-6

? 0
ENTER #: OF COUNTS: 0-255
? 2
OF SWEEPS: 0-255
? 1
STEP-SIZE (MLVTS-STEPS OF 10)
? 250
HILIM-MLVT
? 1000
LOLIM-MLVT
? -2000
TO START-ENTER 1, TO CHANGE PARAMETERS-ENTER 0
? 1

STARTED!

9/19/77 TI:TR 1 MA FULL SCALE

POTENTIAL (V)	CURRENT (MA)	LOG CURRENT
1	-0.014	-11.1764532
0.75	-0.014	-11.1764532
0.5	-0.014	-11.1764532
0.25	-0.01	-11.5129255
0	-0.014	-11.1764532
-0.25	-0.014	-11.1764532
-0.5	-0.014	-11.1764532
-0.75	-0.018	-10.9251388
-1	-0.034	-10.2891498
-1.25	-0.054	-9.82652653
-1.5	-0.082	-9.40879133
-1.75	0.938	-6.97176062
-2	6.E-03	-12.0237511
-1.75	-0.906	-7.00647127
-1.5	-0.29	-8.14562984
-1.25	-0.03	-10.414312
-1	-0.014	-11.1764532
-0.75	2.E-03	-13.1223634
-0.5	6.E-03	-12.0237511
-0.25	6.E-03	-12.0237511
0	2.E-03	-13.1223634
0.25	-2.E-03	-13.1223634
0.5	-2.E-03	-13.1223634
0.75	-0.01	-11.5129255

18. a) Sample of System Output

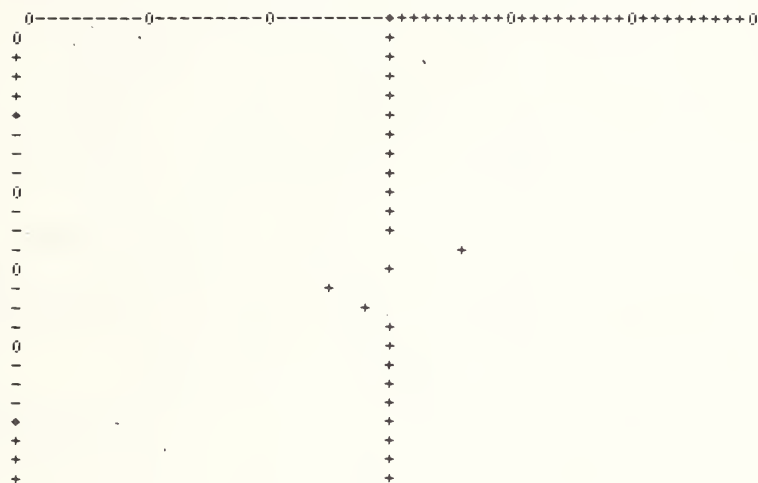
9/19/77

TI:TA

1 MA FULL SCALE

PLOT OF CURRENT VERSUS POTENTIAL

CURRENT



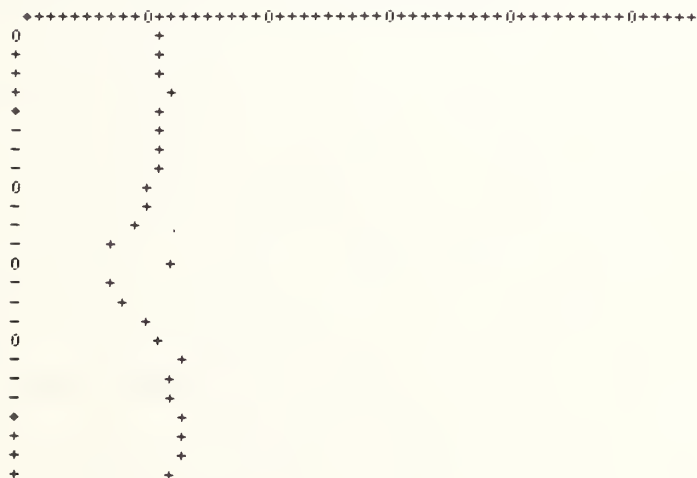
9/19/77

TI:TA

1 MA FULL SCALE

POTENTIAL VS LOG(CURRENT)

LOG OF CURRENT



#: OF SWEEPS LEFT=0
RUN COMPLETE!-----WANT ANOTHER? YES=1, NO=0

18. b) System Output (continued)

we can generate Tafel plots [20]. (Alternatively the machine language program can be changed to one that will check the raw data for steady state conditions after which the data is plotted).

Second, we can perform most of the necessary computations without an operator. This means that the instrument will not only give us the data as acquired, but will perform the necessary mathematical steps to generate a more usable form of information (e.g., calculate the log of the current and then plot those values). The BASIC program in the μ P, although slow compared to a big machine, is capable of most of the operations (except Matrix functions in particular) that BASIC in a larger computer could perform. Computational speed is quite adequate, and for those occasions when it is not, communication with a larger machine is provided.

Third, once programmed and started, the instrument can run unattended. The length of time a run takes does not have to be fixed. The microcomputer can run an experiment for as long as it needs to run. It can be programmed, if necessary, to take emergency measures when conditions exceed limits.

This instrument has, as indicated before, Alternating Current (AC) capabilities. For discussion purposes, we will separate pulse techniques from other methods. In general, in pulse techniques we observe the effects of an impulse input on the cell by observing the decay of its effect. Pulses can be derived either from the timer (minimum width 1 μ sec) or from the voltage controlled oscillator (minimum width 200 nsec). Other waveforms can be provided by the DAC or the VCO (which depend upon the frequency desired-see DAC discussion). If needed, one DAC can provide a DC level which can be summed with the VCO output (controlled by DAC #2) and directed to the potentiostat input.

Direct measurement of AC potentials is possible using the existing ADC for a limited frequency range. To obtain all the information in an AC signal, the sampling rate must be at least twice the highest signal frequency. [21] Our sampling rate for full scale excursions is 300 Hz and thus our maximum

Table 3. Circuit Board Parts Cost and Commercial Availability

PC Board	Prototype Parts Cost	Similar Board Available Commercially*	Commercial Pricing
Microcomputer	\$200	Yes	Same or higher
8K Byte RAM	180	Yes	Higher
8K Byte RAM	180	Yes	Higher
Variable Speed Serial Interface	25	Yes	Higher
Converter & Timer Board (including Signal Distribution)	250	No	--
Power Supplies & Motherboard	150	Yes	Same or higher
TOTAL	\$985		

*Partial listing of possible sources for directly compatible boards:
Motorola, Creative Micro Systems, Electronic Product Associates, and
many others.

frequency would be 150 Hz. In line with our previous discussion, this established maximum would increase as the AC peak to peak voltage decreases. As a practical consideration, however, the increase in bandwidth is not wide enough in general, and another technique should be considered. This can either take the form of a different type of ADC with wider bandwidth or some form of AC to DC converter whose output can be measured by the micro-computer ADC. At present, the response is adequate for our purpose but we are actively pursuing the resolution of this problem for the future.

Cost of Implementation

The system described here was constructed for a parts cost of slightly less than \$1000 (exclusive of terminal). Table 3 shows the breakdown of costs per board. Depending upon desired parameters, systems similar to this can be constructed that range in parts cost from about \$800 on up. The lowest system price is based on the use of minimum memory hardware (no BASIC). Decisions as to memory size, other peripherals, and/or purchase of assembled boards from commercial sources will have a significant effect on overall expense. There is, at present, no commercial source for a tracking type analog to digital converter (similar to the one used here) available, that mates with this bus structure. Successive approximation type converters are available (usually with multiplexed inputs) but they are more expensive, are relatively limited in throughput, and do not contain the necessary timer circuit.

Conclusions

In conclusion, an instrument has been constructed that offers improvement in measurement techniques over manual methods. This device incorporates one of the recent advances in instrumentation (the microprocessor) which allows rapid, concise and consistent measurements not before realized by manual methods.

Acknowledgements

The authors wish to thank H. P. R. Frederikse, A. D. Franklin, and L. H. Bennett for useful discussions. A very special thanks to U. Bertocci without whose advice and encouragement this work would not have been completed.

2.2 High Temperature Solid Electrolytes

Introduction

Oxide solid solutions having a defective fluorite structure and based on ZrO_2 , CeO_2 and ThO_2 , doped with CaO , Y_2O_3 or the trivalent rare earth oxides, have high oxygen ion mobilities relative to the pure constituent oxides. The high oxygen ion mobilities make these oxide solid solutions potentially useful solid electrolytes for high temperature fuel cells. The high oxygen ion mobility results from the large concentration of oxygen vacancies introduced into the oxygen sublattice of the host oxide, about 5 to 15 mole % of dopant may be added depending upon the oxide system.

ZrO_2 -based solid solutions have been used as electrolytes for high-temperature electromotive force measurements since the mid-1930's [22, 23], and ThO_2 -based electrolytes, since 1957 [24]. ZrO_2 -based electrolytes have been studied for fuel cell applications principally at Westinghouse and G.E. in the United States, and elsewhere in France, Germany and the Soviet Union. Recent results [25, 26] on $CeO_2:Ln_2O_3$, where Ln represents a variety of lanthanide ion or Y^{3+} , have revealed oxygen-ion conductivities essentially equivalent to that of $ZrO_2:CaO$ but at temperatures about 200°C lower. Thus, fuel cells using a CeO_2 -based electrolyte might operate at about 800°C as compared to one with ZrO_2 -based electrolyte which would require 1000°C. However, CeO_2 -based electrolytes begin to show appreciable electronic conduction at higher oxygen partial pressures than do the ZrO_2 -electrolytes; for example, one-half of the electrical conductivity is electronic in $(CeO_2)_{0.95}(Y_2O_3)_{0.05}$ at $P_{O_2} = 10^{-14}$ atm ($\sim 10^{-19}$ Pa) for $t = 800^\circ C$, whereas for $ZrO_2:CaO$, $P_{O_2} = 2.5 \times 10^{-31}$ atm 2.5×10^{-36} Pa) for $t = 1000^\circ C$ [27].

At the high oxygen vacancy concentrations present in these electrolytes, the oxygen vacancies are probably nearly all associated with the dopant cations [28]. If these electrolytes undergo prolonged anneals at moderate temperatures ($<1000^{\circ}\text{C}$), the oxygen vacancies, and perhaps to a lesser extent, the dopant cations, may order into a structure coherent with the fluorite structure of the host oxide. Formally, in terms of a coherent structure, the vacancies no longer exist. In actual consequence, the ionic conductivity of the electrolyte may decrease (resistance may increase) because the vacancies, relative to the fluorite structure, must then move cooperatively.

The existence of coherent structures is well documented for ZrO_2 -based solid solutions [29-36]. Coherent structures in CeO_2 -based solid solutions have not been identified.

Carter and Roth [33] found that the increase in resistance of calcia stabilized zirconia (CSZ) when annealed at $<1000^{\circ}\text{C}$ was associated with the formation of coherent structures, observed as superstructure in neutron and x-ray diffraction. This "aging" of CSZ could be reversed ("deaged") by annealing at 1400°C . In a high temperature fuel cell aging of the electrolyte would reduce the efficiency of the cell.

A second aging process which may alter the long-term performance of a high temperature fuel cell electrolyte is the redistribution of the dopant cations along the grain boundaries. Relative to the lattice, the dopant cations appear as negative charges. Thus, they can be expected to migrate under the influence of an applied field. Although the mobility of these cations within the interior of the grain is negligibly small for practical purposes, their mobility in the grain boundaries can be significant. For example, from the tracer diffusion measurements for

Ca^{2+} ions in CSZ [37], the time required for Ca^{2+} ions to cross a 20 μm thick electrolyte film with a potential difference of 0.8 V is on the order of hundreds of years. On the other hand, the same tracer diffusion study showed that migration of Ca^{2+} ions in the grain boundaries is perhaps 1000 times larger at 1800°C than the bulk diffusion rate, a ratio that would be expected to be even larger at lower temperatures. Hence, migration of the dopant ions along grain boundary paths over significant distances during times of the order of a year or less can be expected in all of the fluorite-structure oxides of current interest as solid electrolytes.

The migration of dopant ions along grain boundaries can be expected to result in at least three deleterious effects: (1) a build-up of a resistive layer at either electrolyte boundary, (2) a build-up of a space charge at the electrodes resulting effectively in an overvoltage, and (3) a possible interference with the electrode reaction due to a change in electrolyte composition at the electrolyte-electrode boundaries.

The NBS program of studies on high-temperature electrolytes currently contains two elements: a study of degradation mechanisms in CeO_2 -based oxygen-ion electrolytes, and the development of the impedance measurement as a method of analyzing fuel cell performance with the particular aim of developing a lifetime-prediction test.

2.2.1 Electrolyte Materials

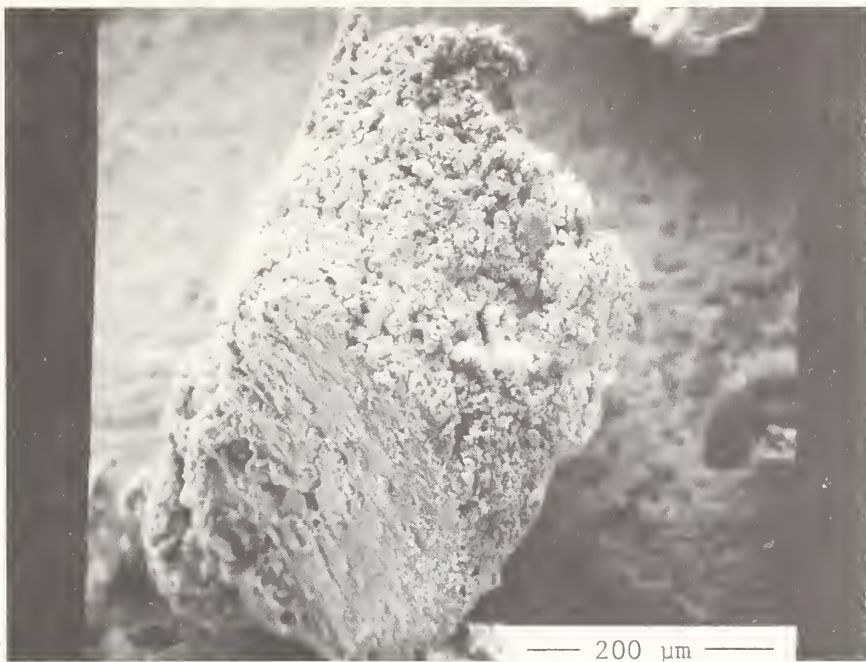
Introduction

In an effort to produce $\text{CeO}_2:\text{Y}_2\text{O}_3$ specimens of high density and uniform composition, chemical preparation of sinterable powders with the desired compositions was undertaken this year. This work is summarized

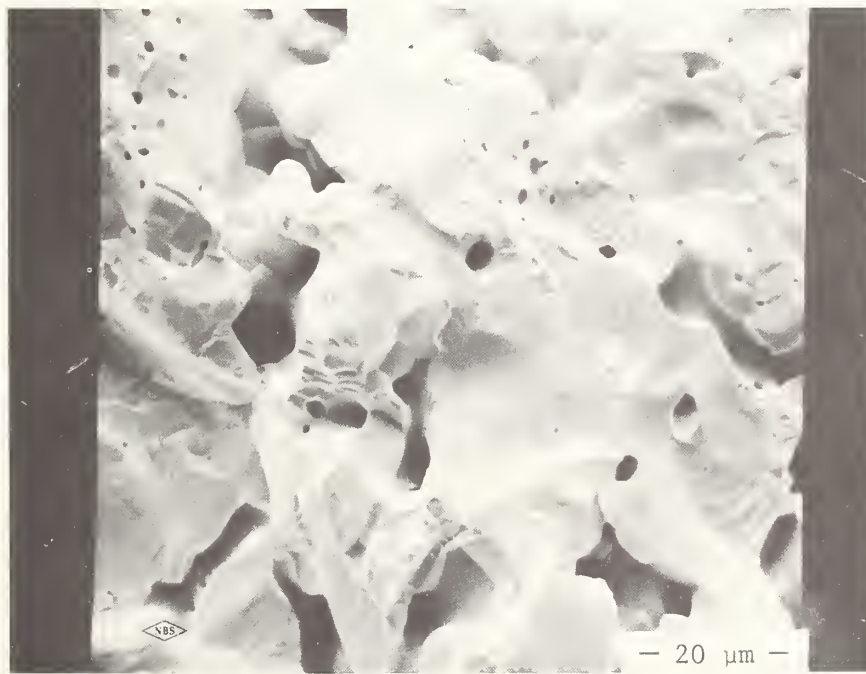
here, and in particular, the details of one procedure, "the carbonate procedure", are given. The carbonate procedure is now in use to prepare 600 to 700 g batches of powder for hot-pressing. Two other procedures which show promise are briefly described. These two procedures utilize complexes of Ce(III) and Y(III) with organic reagents. Cerium-yttrium nitrate stock solutions, whose preparation was described in the previous annual report [54], were used as the starting point for all of the chemical procedures described here.

Chemical preparation of ceria-yttria powders generally requires one or more coprecipitations. Insufficient control of the precipitation process can result in aggregation of the precipitate particles. The pores incorporated into the aggregates can persist to the final sintered specimens unless further chemical processing, extensive grinding or isostatic pressing of the green-bodies to high pressures (300 to 700 MPa) [38] are used to break up the aggregates.

An example of the persistence of pores is shown by the SEM micrographs in Fig. 19. Figure 19a shows an aggregate particle from a powder obtained by coprecipitating the ceria-yttrium hydroxide from a nearly concentrated nitrate stock solution by the addition of ammonium hydroxide; followed by rinsing successively with water, ethanol, acetone and toluene; and then by air-drying. Upon examination at higher magnifications than that of Fig. 19a, the particle shows rather even surfaces punctuated with pores, such as that in the lower part of the picture, and surfaces consisting of billowy masses of particles, such as that on the upper portion of the aggregate particle. Fig. 19b shows a fracture surface of a specimen fabricated from such material and sintered for 4 days at 1525°C. Although there appears to be regions where the grains are



19a. Aggregate particle from a precipitation of Ce-Y hydroxides by the addition of ammonium hydroxide to a nitrate solution.



19b. Fracture surface of a sintered specimen which was fabricated from a powder containing aggregates similar to that shown in Fig. 19a.

thoroughly sintered together, the specimen also appears to be interlaced with rather large pores. The bulk density of specimens isostatically pressed and sintered from the aggregated material was 5.51 to 5.65 g/cm³ (79 to 81% of theoretical).

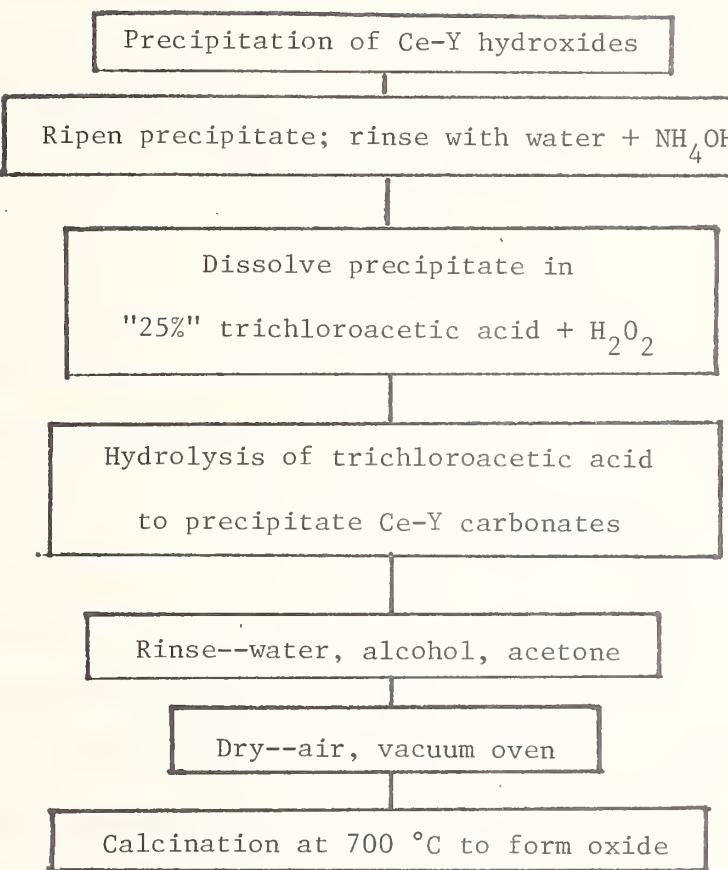
Aggregation can be reduced significantly by using the homogeneous release within the solution of the precipitating agent. The science and techniques of homogeneous precipitation were discussed by Gordon [39,40] and by Gordon et. al. [41]. The hydrolysis of trichloroacetic acid to precipitate the carbonates and of the decomposition of urea to precipitate the hydroxides were examined in our work as possible techniques for preparing sinterable ceria-*yttria* powders.

Homogeneous Precipitation of the Carbonates

The preparation of rare earth carbonates by the hydrolysis of trichloroacetic acid solutions of the rare earth salts was first reported by Salutsky and Quill [42]. They prepared the carbonates of lanthanum, neodymium and samarium. This method was subsequently extended to the other rare earths [43-46]. Charles [47] carried out an investigation of the compositions of the rare earth carbonates prepared by this method. Head and Holley [48] investigated the hydrolysis reaction under CO₂ atmospheres of moderate pressure and studied the thermal decomposition of the carbonates.

Figure 20 is a diagram of the procedure we have developed based on the hydrolysis of trichloroacetic acid to obtain the rare earth carbonates. Ce and Y hydroxides are prepared by diluting 1 part of nitrate stock solution with 2 parts water and then neutralizing the solution by the dropwise addition of ammonium hydroxide diluted by the same proportion.

Carbonate Procedure



20. Schematic of the carbonate procedure.

The size of our apparatus limits us to about 500 ml of stock solution at a time, the equivalent of about 50 g of oxide, so that blending is required at later stages of the operation. The progress of the neutralization can be followed by the color changes of the solution: the deep red of the ceric solution at high acidity fades as the solution is neutralized; the color is yellow-orange to yellow at a pH of 1 to 2; at a pH of 2 the color of the solution begins to shift from yellow to green and the pH begins to decrease again; the pH decreases to 1, where the solution has a green tint, the yellow having completely faded; the pH then rises rapidly and precipitation starts at pH = 2.8. If the final solution is made slightly alkaline, the precipitate takes on a muddy violet-gray color which suggests the presence of some cerosoceric hydroxide [49]. After the precipitate has been rinsed several times with water containing a small amount of ammonium hydroxide to promote settling, a pale yellow to white precipitate is obtained. With each rinsing the precipitate is warmed and stirred to ripen the precipitate. Following each rinse, the precipitate is allowed to settle before the supernatant liquid is pumped off through a fritted disc.

The carbonate is prepared from the hydroxide by treating the precipitate with 1000 ml of nominally 25 w/o trichloroacetic acid, pH about -0.1 to -0.2, and 25 ml of 30% hydrogen peroxide, added while the solution and precipitate are stirred together. The hydrogen peroxide is added in about a 1:1 mole ratio to the amount of Ce present to promote the dissolution of the precipitate. The mixture of precipitate and solution becomes brown immediately upon the addition of the hydrogen peroxide, and a thick head of foam develops; after about 30 minutes the solution becomes clear and the foaming ceases.

Hydrogen peroxide has long been known as an aid to dissolving ceric oxide in hydrochloric acid [50], chlorine being evolved as the oxide is dissolved and reduced. However, in the present case the hydrogen peroxide appears to attack primarily the Ce(IV) ions either in the precipitate or in the solution, reducing them to Ce(III) and apparently forming a colored complex with the Ce(III) as an intermediate in the reaction [49,51].

After the solution clarifies, it is diluted to give a total volume of 3000 ml and warmed to 80-100°C to hydrolyze the trichloroacetic acid. When the hydrolysis is completed, about 30 g of ammonium bicarbonate, NH_4HCO_3 , are added to neutralize the solution and to bring down all of the precipitate. The solution is warmed for an additional 24 hours to ripen the precipitate and to reduce the volume of the supernatant liquid. Several of the precipitates may be blended at this point. The supernatant liquid is pumped off through a fritted disc, and the precipitate is rinsed several times with water containing a small amount of NH_4HCO_3 , then with ethanol and finally with acetone. The precipitate is dried first in air and then in a vacuum oven at 60°C.

An SEM examination of the Ce-Y carbonate prepared by the above procedure showed many small platelets, see Fig. 21, plus larger masses having a layered structure. No structure lines were observed with x-ray diffraction.

After calcination of the material at 700°C for 6 hours, the fluorite structure oxide was obtained. A portion of the initial oxide powder prepared by the carbonate procedure was isostatically pressed into two specimens and calcined at 1500°C for 3 days to yield sintered specimens with bulk densities of 6.32 and 6.53 g/cm³ (95 and 97 % of theoretical).

Preparation of Mixed Oxide Powders via Organic Resins

In an attempt to produce finer, unaggregated powders the coprecipitated Ce-Y hydroxide was dispersed in, or complexed by, several organic resins. The following organic media and processes were investigated:

1. homogeneous precipitation of the hydroxide in excess succinic acid;
2. dispersion of the hydroxide in tartaric acid;
3. dispersion of the hydroxide in citric acid;
4. dispersion of the hydroxide in the tartarto-ethlyene glycol ester;
5. dispersion of the hydroxide in the citrato-ethylene glycol ester.

For process "1." the hydroxide was formed by the decomposition of urea in the presences of succinic acid--6 moles of acid to 1 mole of oxide. The solution was evaporated to dryness with stirring to disperse the hydroxide in the organic matrix. For processes "2." to "5." the hydroxide was coprecipitated from the nitrate solution by the addition of ammonium hydroxide, then rinsed and dispersed in the organic matrix. As in the case of "1." the solution was evaporated to dryness with stirring. The incorporation of the hydroxide into an ester of a polycarboxylic acid and ethylene glycol was suggested by Pechini [52]. The resin then was burned off to yield the oxide powder. For process "1." the burn-off was carried out in a Pt crucible heated to 700°C for 4 1/2 hours in a furnace. Since complete removal of the resin from the beaker in which it was made was difficult, the resins obtained by the other processes were burned off in situ by heating the beaker on a hot-plate and directing a stream of oxygen on to the surface of the resin.

SEM micrographs of the oxide powders from the succinato-resin, the tartrato-resin and the tartrato-ethylene glycol ester resin are compared in Fig. 22, 23 and 24. Results for the citrate-based resins were similar to those for tartrate-based resins.

The oxide particles from the succinato-resin, Fig. 22, are somewhat spherical nodules with a diameter of $32\pm8\text{ }\mu\text{m}^*$. The nodules appear to be hollow, fragile structures as evidenced by the broken one to the upper left of center in the micrograph. These small, uniformly sized nodules probably resulted from the homogeneous precipitation. The subsequent burning-off of the resin appears to leave these structures more-or-less intact.

In contrast to Fig. 22, the oxide particles from the tartrato-resin, Fig. 23, are massive aggregates similar to those obtained when the hydroxides are coprecipitated under nonhomogeneous conditions, see Fig. 19a. The large particles, diameter = $0.23\pm0.03\text{ mm}^*$, with similar shapes, in Fig. 23 are from the coarse fraction which was obtained after grinding and sieving to remove the fines for surface area and sintering studies. Although the size of the coarse particles is not indicative of the size of the initial particles in the precipitate, the micrograph still suggest that considerable aggregation occurred during precipitation and that the cohesion within an aggregate particle may be fairly strong.

The oxide particles from the tartrato-ethylene glycol ester resin, Fig. 24, show some massive aggregates among many fine particles. This sample also was obtained from the coarse fraction after grinding and sieving to remove the fines for further study. The mixture of coarse

* The uncertainty expresses the 95% confidence limits.



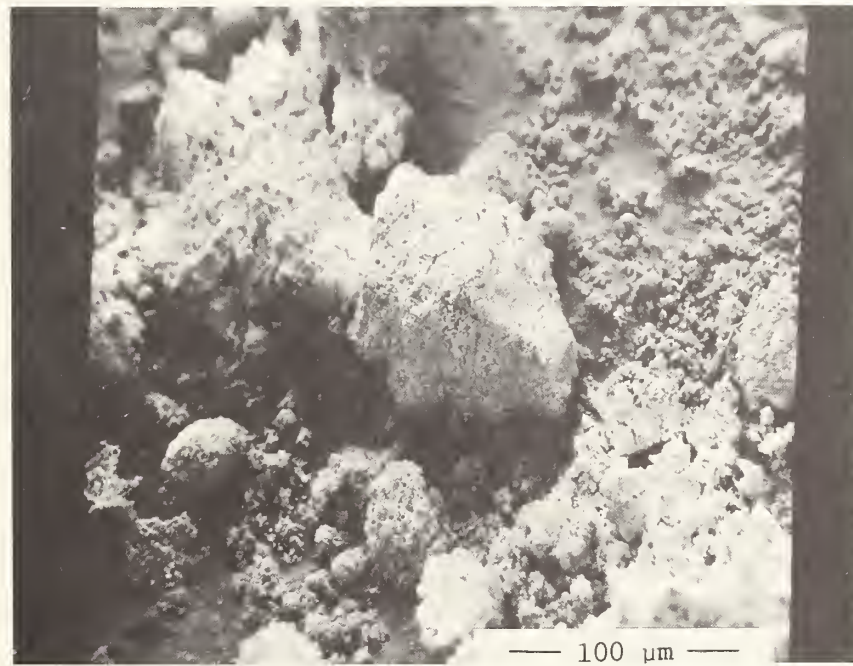
21. Ce-Y carbonate platelets.



22. Ce-Y oxide nodules prepared by homogeneous precipitation and dispersal in a succinic acid resin.



23. Ce-Y oxide, coarse aggregates after grinding; powder prepared by nonhomogeneous precipitation of the hydroxides and dispersal in a tartaric acid resin.



24. Ce-Y oxide aggregate and fines; powder prepared by nonhomogeneous precipitation of the hydroxides and dispersal in a tartaric-ethylene glycol ester resin.

aggregates and fines in the SEM sample suggests that there is less cohesion within these aggregate particles than for the particles from the tartrato-resin.

Although these results are preliminary, they suggest that homogeneous precipitation of the hydroxide may be required if large, and possibly hard, aggregates are to be avoided in using any of the resin processes.

Preparation of Mixed Oxide Powders via Extraction of an
Organic Complex

This method was suggested by the work of Sudarikov et. al. [53] on the extraction of scandium, yttrium, cerium, lanthanum, uranium and thorium salicylates into isoamyl alcohol (3-methyl - 1-butanol). They found that both the Ce-complex and the Y-complex could be extracted quantitatively at a pH >5. In our preliminary work we obtained yields of 70 to 90% for the oxide powder depending upon the amount of salicylate used.

The pH of the nitrate stock solution was adjusted to about 1 by the addition of ammonium hydroxide. The solution then was diluted and treated with hydrogen peroxide to reduce the Ce(IV) to Ce(III). Salicylic acid was added to 25 ml aliquots of the solution in the molar ratio of about 3:1 for three samples and of about 6:1 for three samples. The samples then were titrated with an ammonium hydroxide solution, about 0.25 M, to a pH of about 5.5 - 6.0. A slimy brown precipitate was obtained which was extracted quantitatively into isoamyl alcohol. The isoamyl alcohol fraction was transferred to a distillation apparatus where most of the alcohol was recovered. Once most of the alcohol had

been removed from the precipitate, the distilling flask was removed from the apparatus and heated to decompose the precipitate to an oxide powder having the fluorite structure.

Figure 25 is an SEM micrograph of one of the oxide particles. Although the particles generally appeared to be small, they showed considerable aggregation, as illustrated by the particle in the micrograph. Adjustment of the pH homogeneously by the decomposition of urea may reduce the amount of aggregation.

Summary

Although homogeneous precipitation of the carbonate is being used at present to prepare batches of the oxide powders, the resin techniques and the extraction technique show enough promise to encourage further efforts to perfect them. There are three observations which hold for all of the techniques.

First, a preliminary coprecipitation of the hydroxides from the nitrate solution is desirable so that the fluoride and the excessive nitrate present in the stock solution can be removed. This precipitation can be carried out rapidly by neutralization with ammonium hydroxide rather than with one of the slower homogeneous processes. The hydroxides can be dissolved and the Ce(IV) can be reduced to Ce(III) in a moderately acid solution.

Second, a subsequent coprecipitation is best performed from a homogeneous solution to minimize aggregation of the precipitate.

Third, the supernatant liquid can be removed more rapidly by pumping it off through a fritted disc than by collecting the precipitate on a filtering funnel.



25. Ce-Y oxide aggregate; powder prepared by nonhomogeneous precipitation of the salicylate and extraction into isoamyl alcohol.

The carbonate procedure requires several rinses of the carbonate precipitate to remove any chloride ions produced by side-reactions during the hydrolysis of the trichloroacetic acid. The resin techniques and the extraction technique avoid the slow rinsing operations, but these techniques entail either the evaporation of the aqueous solution or the distillation of the alcohol, both of which may be time (and energy) consuming. The extraction technique seems to offer the possibility for further purification of the oxides since Na-ions, a major contaminant, may remain mostly in the aqueous phase when the Ce-Y salicylates are extracted into the isoamyl alcohol.

Acknowledgement

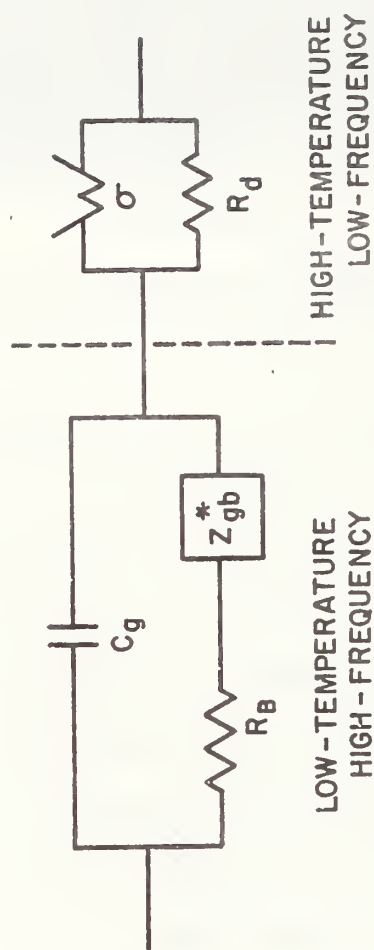
We wish to thank Gail Cooper for performing many of the chemical procedures reported here.

2.2.2 Impedance Measurements

Introduction

As described in our last Annual Report, for calendar year 1976 [54], we are studying the ac impedance of specimens of Y-doped CeO_2 fitted with symmetrical sputtered Pt electrodes over the range of frequency from 10 Hz to 13 MHz and of temperature from room temperature to about 850°C. Tank O_2 and tank N_2 are being used at present to vary the oxygen partial pressure, but equipment is being installed to control and measure this pressure quantitatively.

These data are being handled in the framework of equivalent circuits of the kind shown in Fig. 26. Z_{gb}^* is a contribution to the impedance that has a broad distribution of time constants and is thought to arise



26. Equivalent Circuit for Y-doped CeO_2 Ceramic with Sputtered Pt Electrodes.

from the presence of inhomogeneities in the interior of the specimen.

We find it can be represented by a Cole-Cole [55] equation:

$$Z_{gb}^* = \frac{\Delta Z_{gb}}{1+(jw\tau)^{1-\alpha}}. \quad (1)$$

The electrode impedance, Z_{el}^* , can also be represented by an equation of this sort. In eqn (1), τ is the most probable time constant and α is a measure of the width of the time constant distribution. The circular frequency is w , and ΔZ_{gb} is the contribution of this mechanism to the dc resistance.

The impedance data as a function of frequency are fitted to the equations for the equivalent circuit by a steepest-descent least-squares fitting procedure that gives as output the "best" values for the parameters of the equivalent circuit and their standard deviations. The fit is achieved by minimizing the sum of the squares of the distances in the complex plane between the experimental and calculated points. A test [56] of the entire measurement and data handling procedure was run on a dummy specimen composed of two resistors and two capacitors whose values were measured independently to better than 1%. The impedance measurements were fitted using the actual circuit as the equivalent circuit and determining the resistances and capacitances as "best" values by the fitting technique. The results gave an excellent account of the frequency dependence of the data, and the "true" values for the resistances and capacitances were reproduced to within $\pm 10\%$.

Experimental Results-The Bulk Arc

According to the equivalent circuit of Fig 26, at high frequencies the impedance data are determined essentially by the part of the circuit

on the left hand side of the dotted line, the so-called bulk effect.

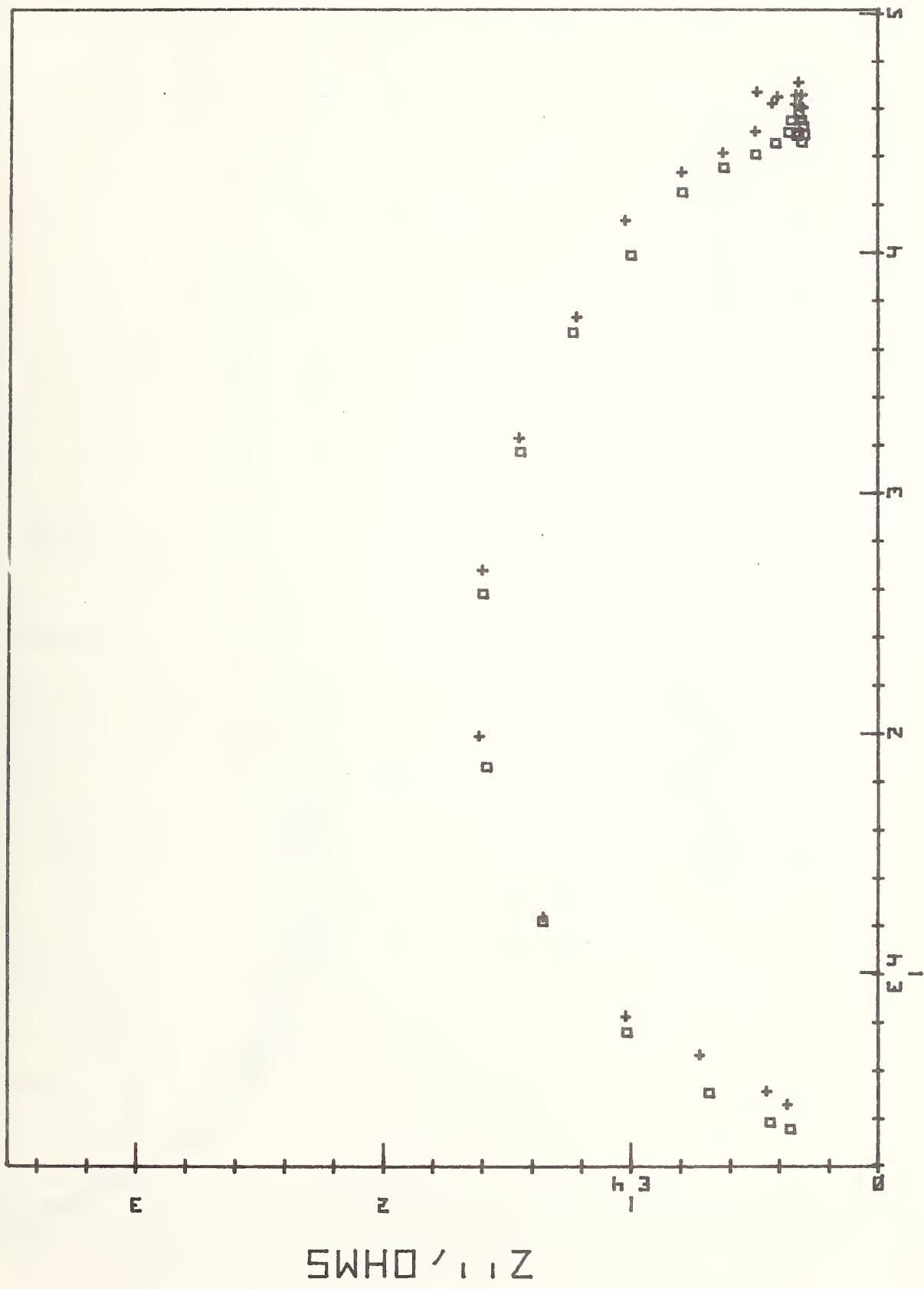
The circuit elements here are the geometric capacitance, C_g , the resistance R_B of the interior of the conducting grains, and an inhomogeneity contribution indicated by Z_{gb}^* as given by eqn. (1).

All of these elements should be independent of the oxygen partial pressure, and indeed the indications are that they are. Figure 27 shows measurements made in O_2 at $350^\circ C$, and then after replacing the O_2 with N_2 . This figure represents the complex plane for the impedance, with Z' the real and $-Z''$ the imaginary part. Very little change is seen. On the other hand, the sputtered Pt electrodes under study appear to age persistently. Figure 28 shows the data taken at $250^\circ C$ for several runs on another specimen. The very low frequency data, on the right hand side, represents the inhomogeneity effect. The curves, which are numbered in the order in which the data were taken, represent a parallel R-C network fitted to the highest frequency data, starting at the point indicated by the arrow in Fig. 28. Curves 1 and 3 refer to data taken in O_2 , while the data in curves 2, 4, and 5 were taken in N_2 . Between curves 1 and 2 the specimen was heated to $804^\circ C$ in N_2 and O_2 .

Sintering of the electrode could reduce the contact between the solid electrolyte and the metal electrode, and thus increase the specimen resistance. To a first approximation, there should be little or no effect on the capacitance, since the ratios of the spacing between the electrolyte and non-contacting electrode particles to the electrolyte thickness should be much smaller than the inverse dielectric constant of the electrolyte. The parameters drawn from the arc fits are shown in Table 4.

FEB 13, 1978 02 AND N2

Al2 350 02 63

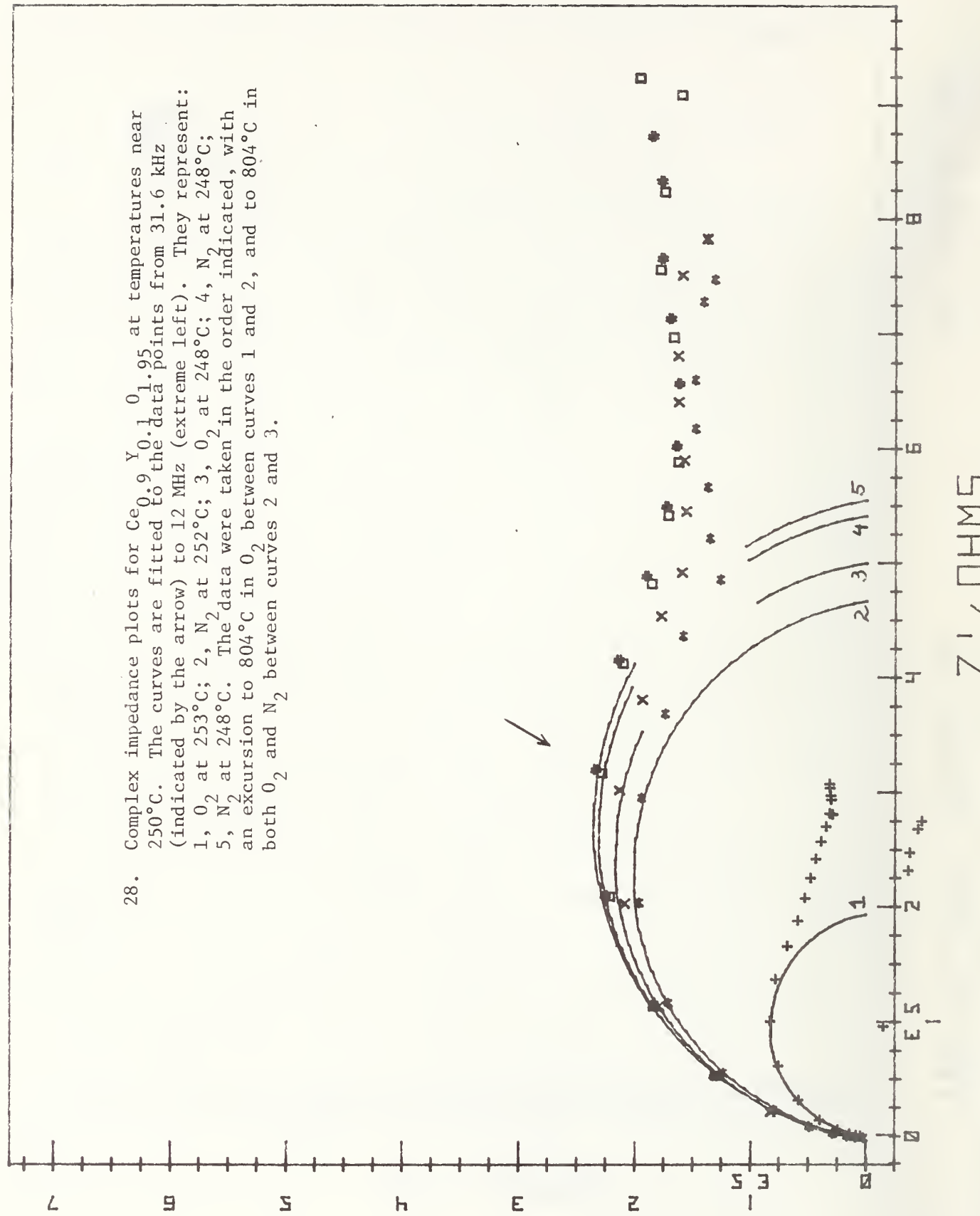


27. Complex Impedance Plot for Bulk Arc for $\text{Ce}_{0.9}\text{Y}_{0.1}\text{O}_{1.95}$ in O_2 (□) and N_2 (+) at 350°C . Z' is the real and Z'' the imaginary parts of the impedance.

FEB 13, 1978

HPB 248 NZ 97

28. Complex impedance plots for $\text{Ce}_{0.9} \text{Y}_{0.1} \text{O}_{1.95}$ at temperatures near 250°C. The curves are fitted to the data points from 31.6 kHz (indicated by the arrow) to 12 MHz (extreme left). They represent: 1, O_2 at 253°C; 2, N_2 at 252°C; 3, O_2 at 248°C; 4, N_2 at 248°C; 5, N_2 at 248°C. The data were taken in the order indicated, with an excursion to 804°C between curves 1 and 2, and to 804°C in both O_2 and N_2 between curves 2 and 3.



5MHz - 11Z

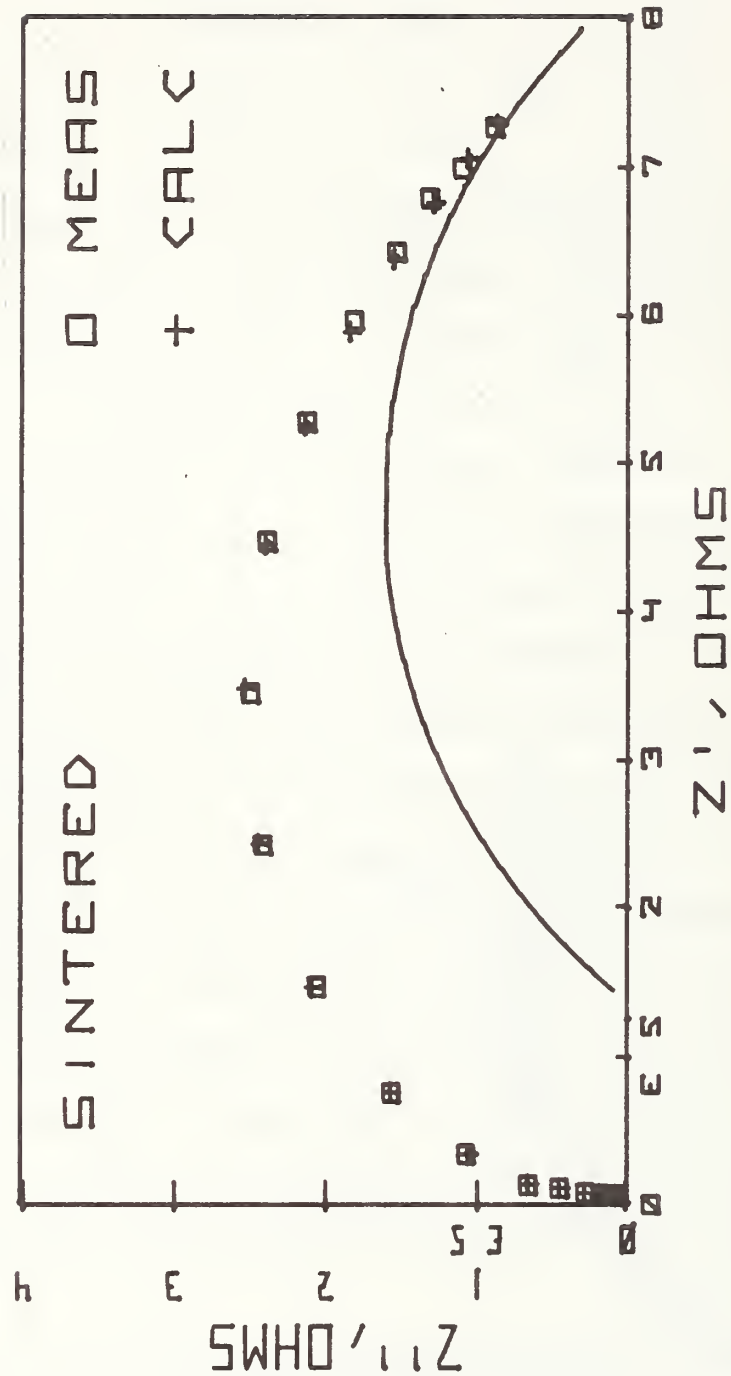
Table 4. Resistance and Capacitance Values from Arc. Fits in Fig. 28.

<u>Curve</u>	<u>Atmos.</u>	<u>T°C</u>	<u>R_B, Ω</u>	<u>C, pF/g</u>	<u>$R_B C$, rad/s/g</u>
1	O_2	253	1.9×10^5	13.2	3.9×10^5
2	N_2	252	4.7×10^5	6.9	3.1×10^5
3	O_2	248	5.0×10^5	7.1	2.8×10^5
4	N_2	248	5.4×10^5	6.9	2.7×10^5
5	N_2	248	5.5×10^5	6.9	2.6×10^5

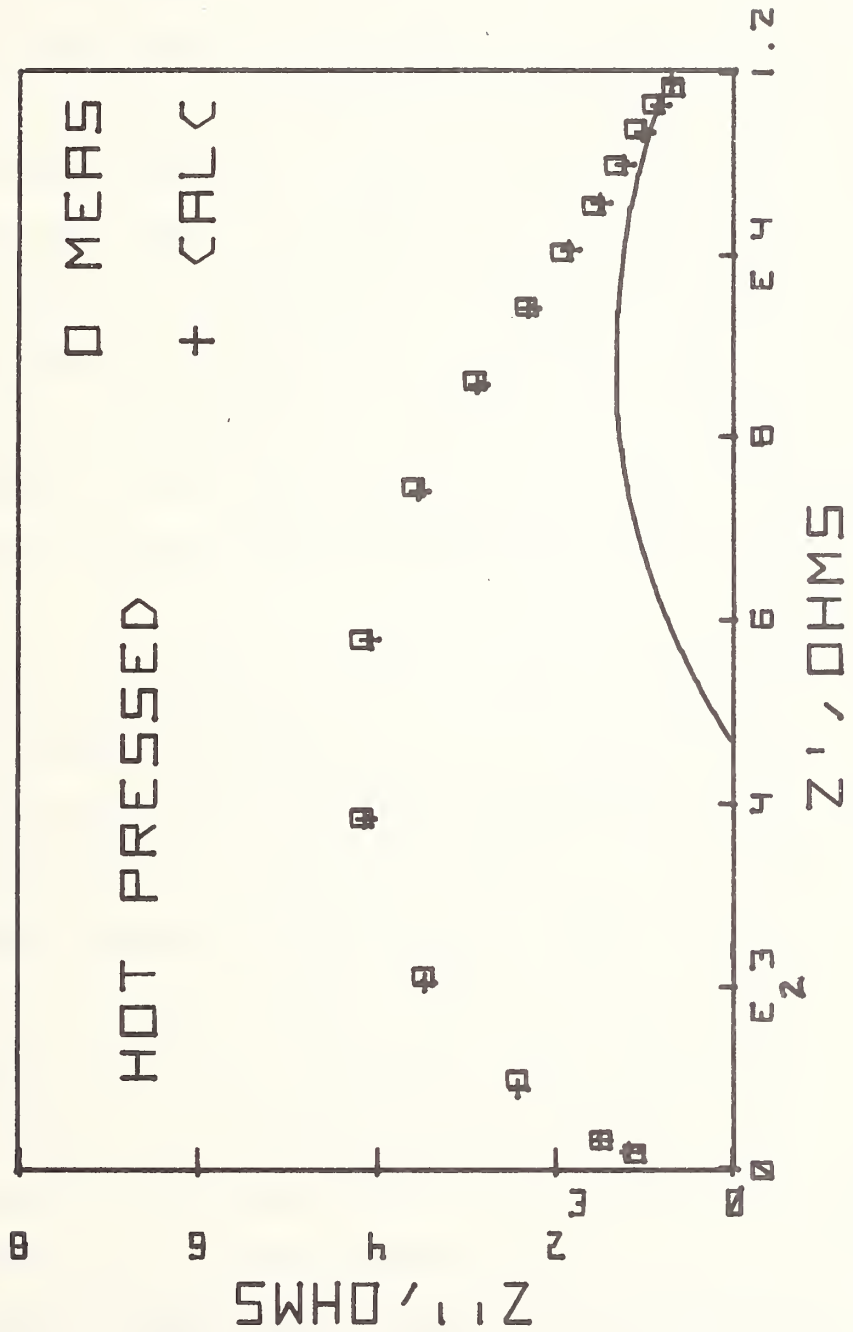
After the first curve the capacitance does stay essentially fixed while the resistance rises almost 20%, finally stabilizing at a value not much influenced by the atmosphere. Continued sintering and loss of contact seems a likely explanation for the instability.

Because of this lack of stability in the Pt electrodes, comparisons of absolute magnitudes from one specimen to another must be done cautiously. However, some meaningful comparisons can be made. Figures 29 and 30 compare the data for sintered and hot-pressed specimens of $Ce_{0.9} Y_{0.1}$ _{1.95}, the latter being considerably denser (~96% of theoretical) than the former (~85%). The data in each case were fitted with the high-frequency part of the equivalent circuit of Fig. 26. The arc shown in each figure represents Z_{gb}^* alone. The span of the arc is ΔZ_{gb} , and the left-hand intercept is R_B (refer to Fig. 26 and eqn. 1). In Figs. 29 and 30 it is clear that, relative to the bulk resistance, R_B , the more porous sintered specimen exhibits a larger value of ΔZ_{gb} than does the denser hot-pressed specimen. This observation is consistent with our interpretation of Z_{gb}^* as arising from inhomogeneities in the specimen, in this case the pores.

The appearance of the right-hand part of the high-frequency arc depends strongly on temperature. Figure 31 shows data on hot-pressed



29. Complex impedance plot for sintered $\text{Ce}_{0.9} \text{Y}_{0.1} \text{O}_{1.95}$ at 250°C in O_2 . Calculated values are from the equivalent circuit of Fig. 26 (high frequency side), fitted to the data. The arc represents Z^* _{gb}.



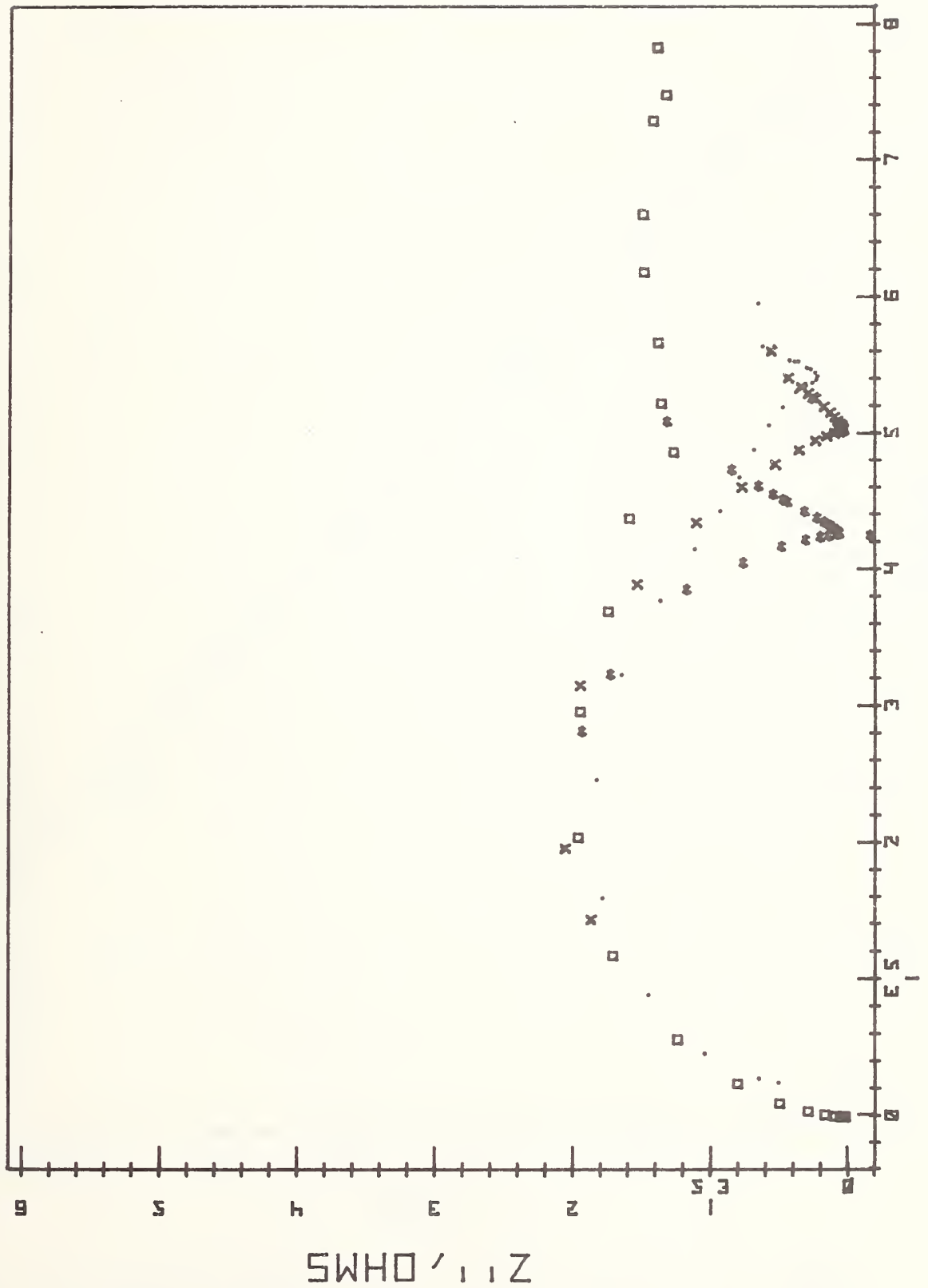
30. Complex impedance plot for hot-pressed $\text{Ce}_{0.9} \text{Y}_{0.1} \text{O}_2$ at 250°C in O_2 . Calculated values are from the equivalent circuit of Fig. 26, fitted to the data. The arc represents Z^*_{gb} .

$\text{Ce}_{0.9} \text{Y}_{0.1} \text{O}_{1.95}$ at four temperatures from 252 to 580°C. These data have been scaled so that the left-hand portions roughly coincide, in order to reveal the changes taking place in the right-hand side as the temperature increases. At the lowest temperature (252°C) there almost appear to be two arcs, and as the temperature rises these move together, until at the highest temperature the tangent at the real axis to the curve defined by the data is almost vertical, indicating behavior like that of a simple R-C parallel circuit with only a single time constant. What appears to be happening is that the magnitude of the inhomogeneity impedance is decreasing relative to the bulk resistance as the temperature rises. This is probably the result of the increase in bulk conductivity with increasing temperature, which would tend to produce an increase in screening of the inhomogeneities and a consequent reduction in their influence.

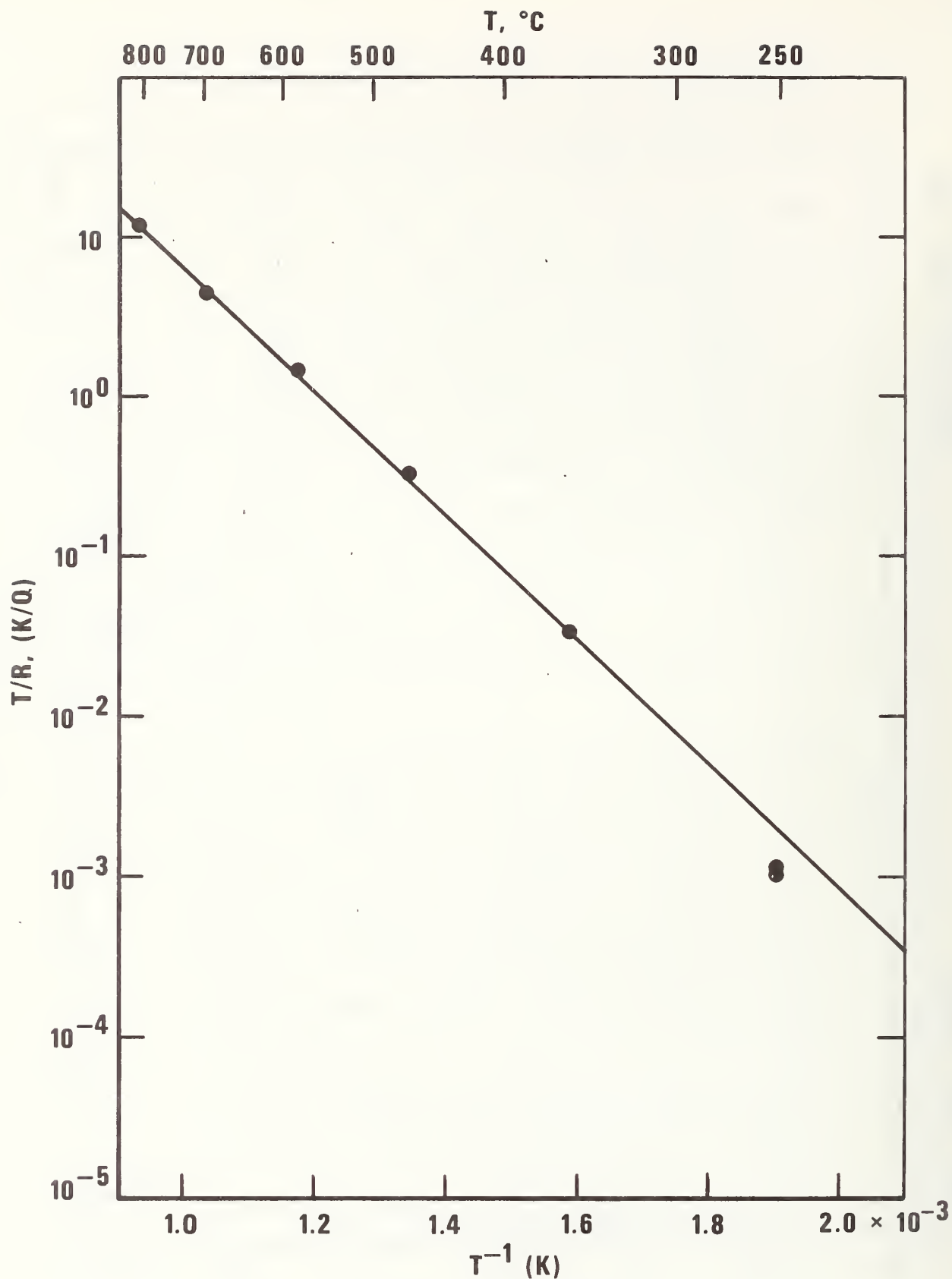
An estimate of R_B , the resistance of the interior of the ceramic grains, can be obtained from the fits of the equivalent circuit to these data. Figure 32 shows these estimates plotted in the form of $\log(T/R_B)$ against T^{-1} , where T is the absolute temperature. The solid line is a least-squares fit to all the points except that at the lowest temperature, where the data are more uncertain. From the slope of this line we calculate an activation energy of 74.3 kJ/mol, in excellent agreement with the value 73.3 kJ/mol obtained by Tuller and Nowick [25] from four-probe dc measurements on somewhat more porous specimens of the same composition. Our value is also in rough conformity with the high temperature value found by Kudo and Obayashi [26] for the same dopant (Y) and composition. This latter value is estimated as about 62.7 kJ/mol from the

FEB 15, 1978

HPB 252 N2 89



31. Complex impedance plot for hot-pressed $\text{Ce}_{0.9}\text{Y}_{0.1}\text{O}_{1.95}$ in N_2 at several temperatures: \square , 252°C ; \bullet , 350°C ; \times , 470°C ; \ast , 580°C .



32. Arrhenius plot for bulk resistance, R_B , for hot-pressed $\text{Ce}_{0.9}\text{Y}_{0.1}\text{O}_{1.95}$ in N_2 .

curves given in their paper, but which must be raised to about 70.4 kJ/mol when corrected for the fact that they plot \ln (resistivity) rather than \ln (resistivity/temperature) - see the discussion below.

Both Tuller and Nowick and Kudo and Obayashi made their measurements at temperatures from about 400°C to about 1000°C. Kudo and Obayashi observed a break in their plots of \ln (resistivity) vs T^{-1} at about 500 to 600°C, a break which does not appear in the data of Tuller and Nowick and also probably not in ours either. The increase in value found by Kudo and Obayashi may arise from a combination of their method of measurement and their specimen preparation. They prepared dense ceramics (>96% of theoretical) by incorporation "when needed" of 3 mole % MgO, which by analogy to results in zirconia [57,58] can be expected to produce partially blocking grain boundaries. They measured the resistance using either an ac bridge at a frequency of 1 kHz or a dc 4-probe method. One kHz is a sufficiently low frequency that at 400°C and up we find all of the inhomogeneity effect to be included in the real part of the resistance. Thus they measured not just the bulk resistance but the bulk resistance plus whatever contribution the inhomogeneities made. We observe in our specimens that the inhomogeneity contribution has a greater temperature dependence than does the bulk, and begins to be a significant part of the total at temperatures below about 500°C. Thus we suggest that Kudo and Obayashi's low-temperature activation energy reflects inhomogeneity effects; it is their high-temperature value that corresponds to the true conduction process in the interior of the grains. Tuller and Nowick [25], on the other hand, worked with unadulterated but porous (>80% theoretical density) material and a dc measurement. They must have included an inhomogeneity contribution in their resistance

measurements but its temperature dependence would have been identical to that of the true bulk resistance and therefore its inclusion would not have affected the measured activation energy. The specimens we have worked with to date, while of very low porosity (>95% theoretical density) and containing no sintering additives, have not been fully reacted and therefore contain small amounts of phases other than the major fluorite phase. These can account for our observation of an inhomogeneity contribution to the resistance with a temperature dependence different from that of the bulk. Thus an appropriate comparison may be made, as above, among the activation energies drawn from the data of Tuller and Nowick [25], the high-temperature data of Kudo and Obayashi [26], and our data over the whole temperature range where the inhomogeneity effect has been removed. Among these activation energies there is reasonable agreement, as noted above.

Kudo and Obayashi [26] plotted $\ln(\rho)$ (resistivity) against T^{-1} . However, for ionic conduction one expects (see for instance eqn. 3.63, Ref 59 and the discussion following it, the following equation to be valid for a single mobile defect:

$$\rho = AT \exp(Q/kt), \quad (2)$$

where ρ is the resistivity, A a constant, T the absolute temperature, Q the activation energy, and k the Boltzmann constant. It follows that the slope of a plot of $\ln(\rho)$ against T^{-1} is given by

$$Q' = Q - kT. \quad (3)$$

That is, the apparent activation energy Q' will be smaller than the real value by a term kT , which ranges from 5.8 to 10.6 kJ/mol in the temperature

range from 400 to 1000°C. This is the source of the 7.7 kJ/mol we added to the Kudo and Obayashi observed value for the apparent activation energy to correct for this effect.

Experimental Results - The Electrode Arc

At high temperatures and low frequencies the data, when plotted in either the impedance or the admittance complex plane, produce a flattened arc. This behavior is reproduced by the equivalent circuit of Fig. 26, using an equation similar to eqn. 1 for Z_{el}^* :

$$Z_{el}^* = \frac{\Delta Z_{el}}{1 + (j\omega\tau_{el})^{(1-\alpha)}} \quad (4)$$

Figure 33 shows representative data compared to values calculated using eqn (4) with fitted parameters. The data are quite well reproduced.

One possible model for this equivalent circuit is a diffusion-controlled Warburg impedance in parallel with a simple resistance, R_d . The parameter α would have the fixed value 0.5 for this model.

Physically this model suggests flow of electrochemically reacting oxygen through two parallel paths (Fig. 34). In one, giving rise to R_d , there is rapid interchange between the oxygen in the atmosphere and the oxygen ions in the electrolyte. This path involves the three-phase electrolyte-electrode-gas contact. According to the experiments of Schouler et al [60] on Ag-electroded stabilized zirconia, R_d depends on temperature and oxygen partial pressure according to

$$R_d = B P_{O_2}^{-1/2} \exp(Q_R/kT), \quad (5)$$

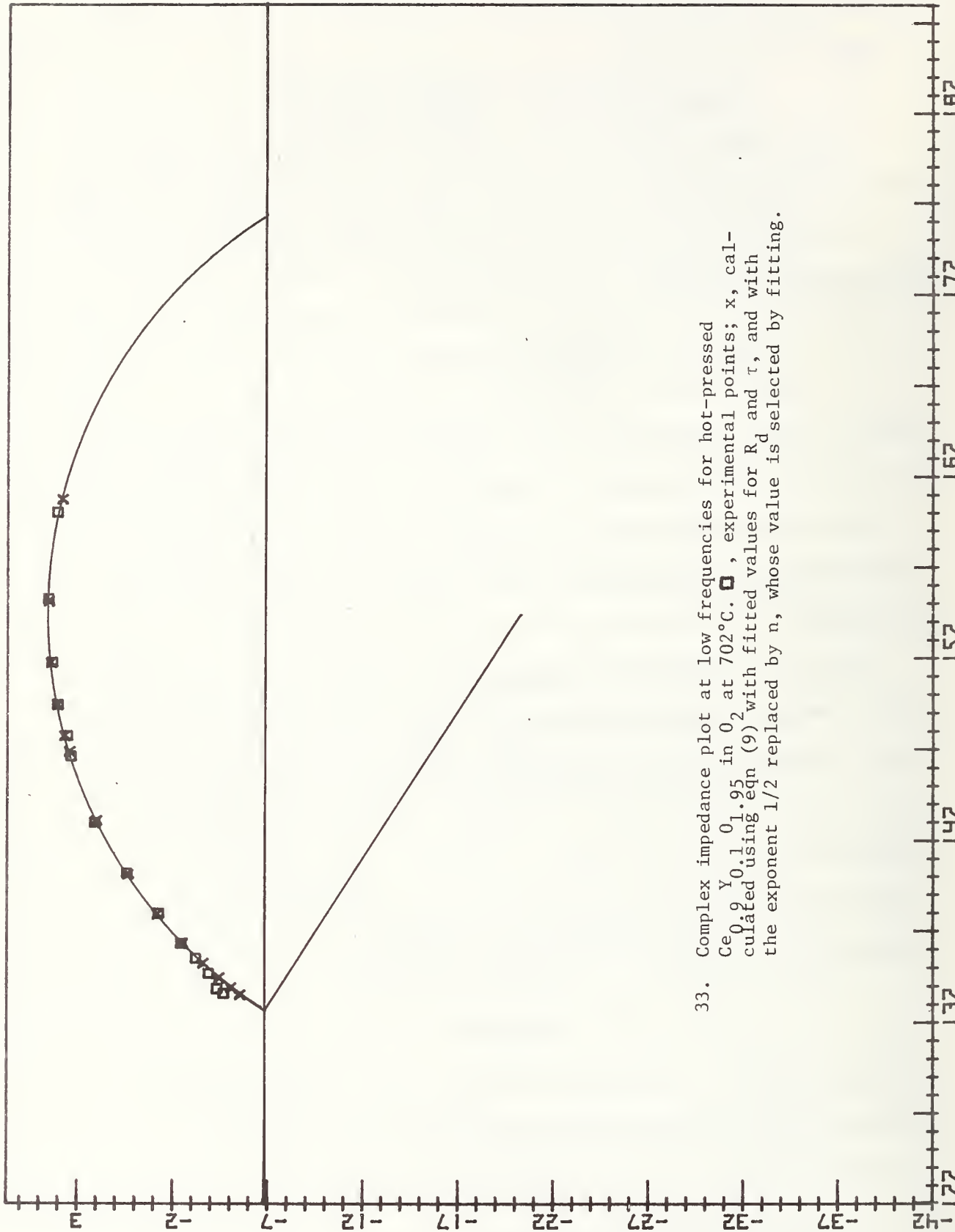
and they suggest the rate-controlling step is the reaction between O atoms and O_2 molecules adsorbed on the electrode-gas interface;

$$2O_{ads} \rightleftharpoons O_{2ads}. \quad (6)$$

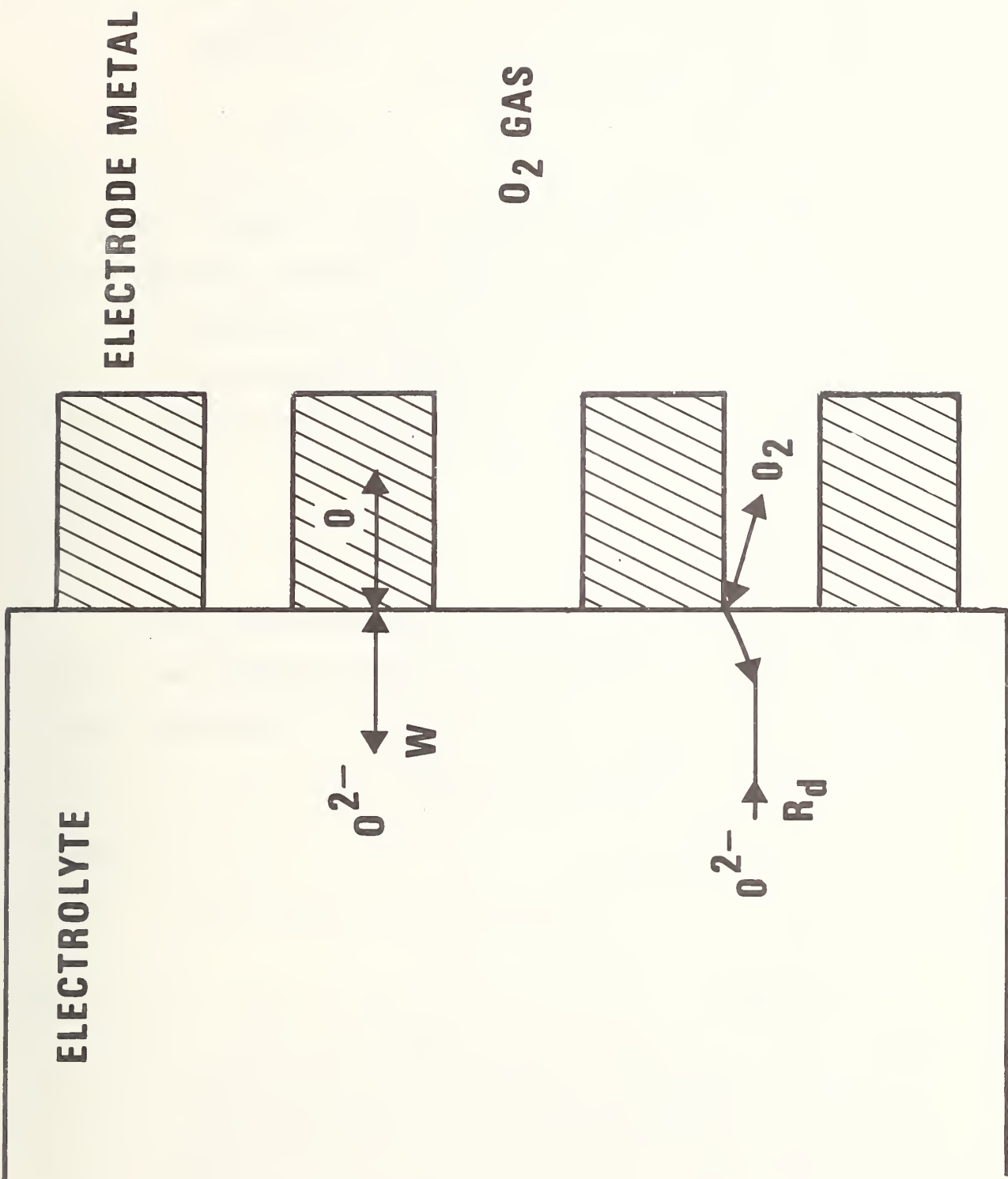
B is a constant depending on the length of the 3-phase line interface.

JAN 21, 1978

HPB 702 02 86



33. Complex impedance plot at low frequencies for hot-pressed $\text{Ce}_{0.9} \text{Y}_{0.1} \text{O}_{1.95}$ in 02 at 702°C. \blacksquare , experimental points; \times , calculated using eqn (9) with fitted values for R_d and τ , and with the exponent 1/2 replaced by n , whose value is selected by fitting.



34. Schematic of Porous Electrode-Electrolyte Interface. R_d denotes the resistive path for the oxygen discharge reaction, and W the diffusive path.

The other path involves interchange between oxygen ions in the electrolyte and oxygen atoms in the electrode material. The rate controlling step is diffusion of the oxygen atoms in the electrode material, and this gives the Warburg-type impedance

$$Z_w^* = \frac{\sigma}{A_E} (1-j) \omega^{-1/2}, \quad (7)$$

where A_E is the area of electrode-electrolyte contact. Grahame [61] has given an expression for σ for the case of smooth homogeneous electrodes with a uniform current density where some reactant is transported by diffusion through the electrolyte to the interface. The situation is essentially unchanged whether the diffusion path lies in the electrode or the electrolyte, and so we adopt Grahame's expression for σ :

$$\sigma = \frac{RT}{2\sqrt{2} F^2 c D} 1/2, \quad (8)$$

in which F is the Faraday, R the gas constant, c the molar volume concentration of diffusing species (0 atoms) and D its diffusion coefficient.

The combination of R_d and Z_w^* produces an expression for the total impedance of the electrode equivalent circuit [54],

$$Z_{el}^* = \frac{R_d}{1 + (j\omega\tau)^{1/2}}, \quad (9)$$

in which τ is given by

$$\tau = \frac{1}{2} \left(\frac{A_E R_d}{\sigma} \right)^2. \quad (10)$$

The plot of Z_{el}^* in the complex plane is an arc whose span on the real axis is R_d and for which the angle between the real axis and the line joining the left intercept with the center of the arc is $\pi/4$. Equation (7) can be valid only at higher frequencies; at low frequencies the Warburg impedance must approach a finite limit.

This electrode arc can be characterized by two parameters. Schouler et al [60] expressed their data in terms of $(R_d/2)$ and

$$C_z = (\tau/2R_d) \quad (11)$$

$$= A_E^2 R_d / (2\sigma)^2, \quad (12)$$

Given measured values of R_d it should be possible to calculate $C_z (A_E^{-2})$ using data in the literature on the solubility and diffusion coefficient of atomic oxygen in the metallic electrodes.

We have made this comparison for the impedance data of Schouler et al [60] for Ag electrodes on Ca-stabilized ZrO_2 . The data on diffusion and solubility of atomic O in Ag were drawn from the work of Ramanarayanan and Rapp [62].

$$D = 4.9 \times 10^{-3} \exp \left[-\frac{5840}{T} \right] \text{ cm}^2 \text{s}^{-1} \quad (13)$$

$$c = 7.01 \times 10^{-3} \exp \left[-\frac{5790}{T} \right] P_{O_2}^{1/2} \text{ mole-cm}^{-3} \quad (14)$$

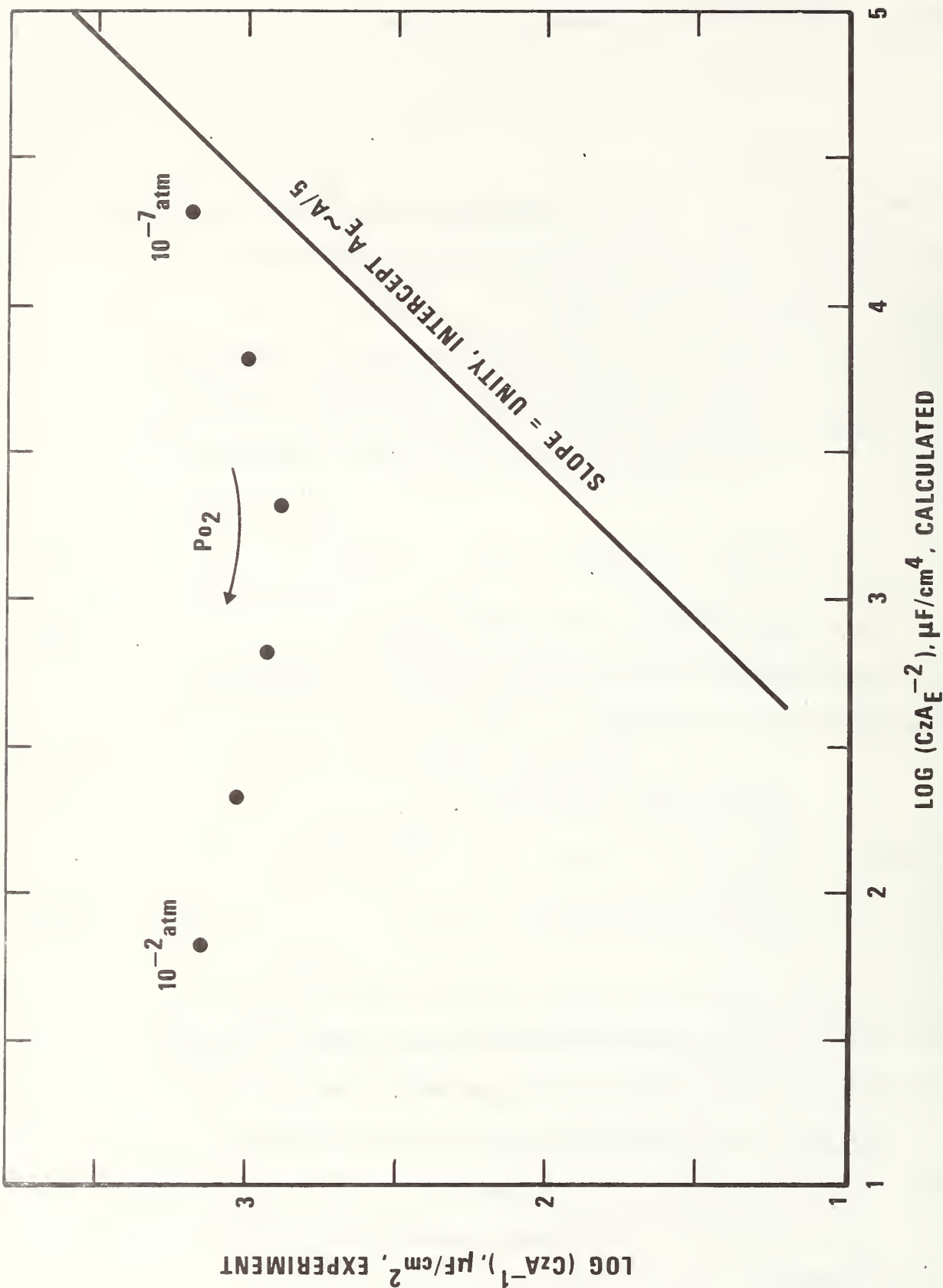
Schouler et al [60] give for the experimental values of the parameters in eqn (5) at 900K:

$$R_d = 1.19 \times 10^{-10} \exp \left(23789/T \right) P_{O_2}^{-1/2} \text{ cm} \quad (15)$$

Combining eqns (8), (12), (13), (14), and (15),

$$C_z A_E^{-2} = (144.2/T^2) \exp(6371/T) P_{O_2}^{1/2} \text{ F/cm}^4. \quad (16)$$

In a later paper, Schouler and Kleitz [63] give a plot of C_z/A vs P_{O_2} at 900K, where A is the geometric electrode area. Figure 35 compares their experimental data with values for C_z/A_E estimated with eqn. (16). Whereas we expect on the basis of the model that the data should lie along a line of unit slope such as the one drawn on Fig. 35, in fact there is very little variation of the observed values for $C_z A^{-1}$ with oxygen partial pressure.



35. Comparison of experimental values (Ref. 63) for effective electrode capacitance per unit area (C_{zF}^A) to values calculated with eqn. 16 (see text). The solid line is illustrative of the expected behavior.

A less detailed comparison can be made with our own data for Pt electrodes. The measurement temperatures range from 478 to 804°C, in tank oxygen and in tank nitrogen. Figures 36 through 39 illustrate the effect of changing from an oxygen to a nitrogen atmosphere. We believe the placement of these curves along the real axis has been affected by the instability of the Pt electrodes discussed above, and expect that with stable electrodes, the left-hand intercepts will be the same for the oxygen and nitrogen atmosphere. The arcs represent the fits of eqn (1) to the data. At the lower temperatures in nitrogen the fitting involves a long extrapolation and the results are obviously somewhat uncertain.

From the fits we derive the values for the parameters of eqn (1) given in Table 5. The parameter τ was converted to C_z using eqn (10).

Table 5. Parameters for Electrode Arc for Hot-Pressed $\text{Ce}_{0.9}\text{Y}_{0.1}\text{O}_{1.95}$

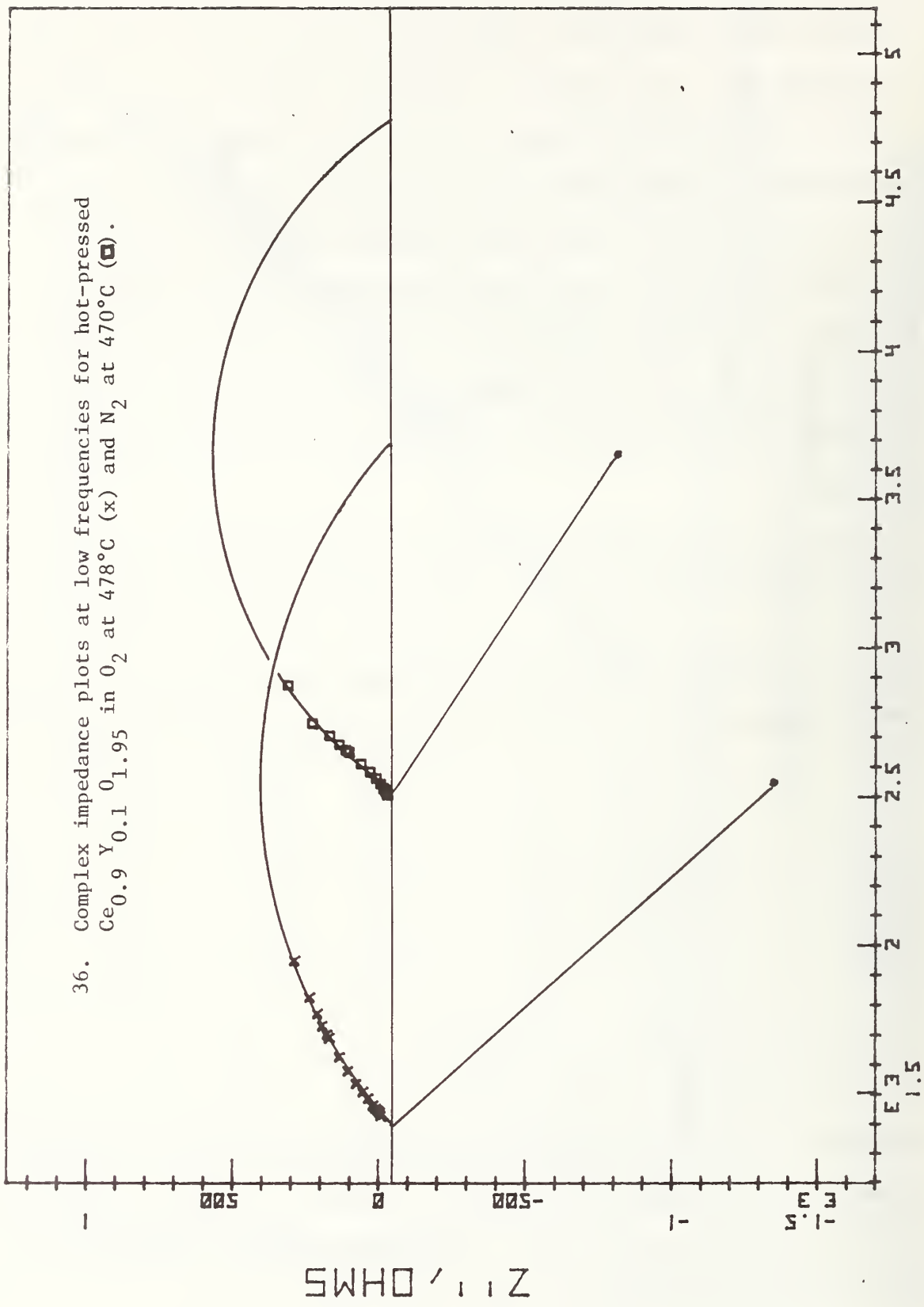
<u>T°C</u>	<u>$\Delta Z_{el}, \Omega$</u>	<u>$C_z, \mu\text{F}$</u>	<u>α</u>	<u>T°C</u>	<u>$\Delta Z_{el}, \Omega$</u>	<u>$C_z, \mu\text{F}$</u>	<u>α</u>
478	2280	69.3	.56	470	2250	60.9	.36
593	496	244	.53	582	1961	116	.27
702	43.7	169	.39	694	534	154	.32
804	7.2	116	.38	804	51.0	208	.38
804	6.8	112	.40				

Figure 40 and 41 show the variation of ΔZ_{el} and C_z , respectively, with temperature for both atmospheres. At the higher temperatures, where the parameters are best known, ΔZ_{el} appears to exhibit an exponential dependence on T^{-1} , with an activation energy of 164 to 328 kJ/mol. This value is a bit more than twice the activation energy, 73.3 kJ/mol, given by Tuller and

FEB 10, 1978

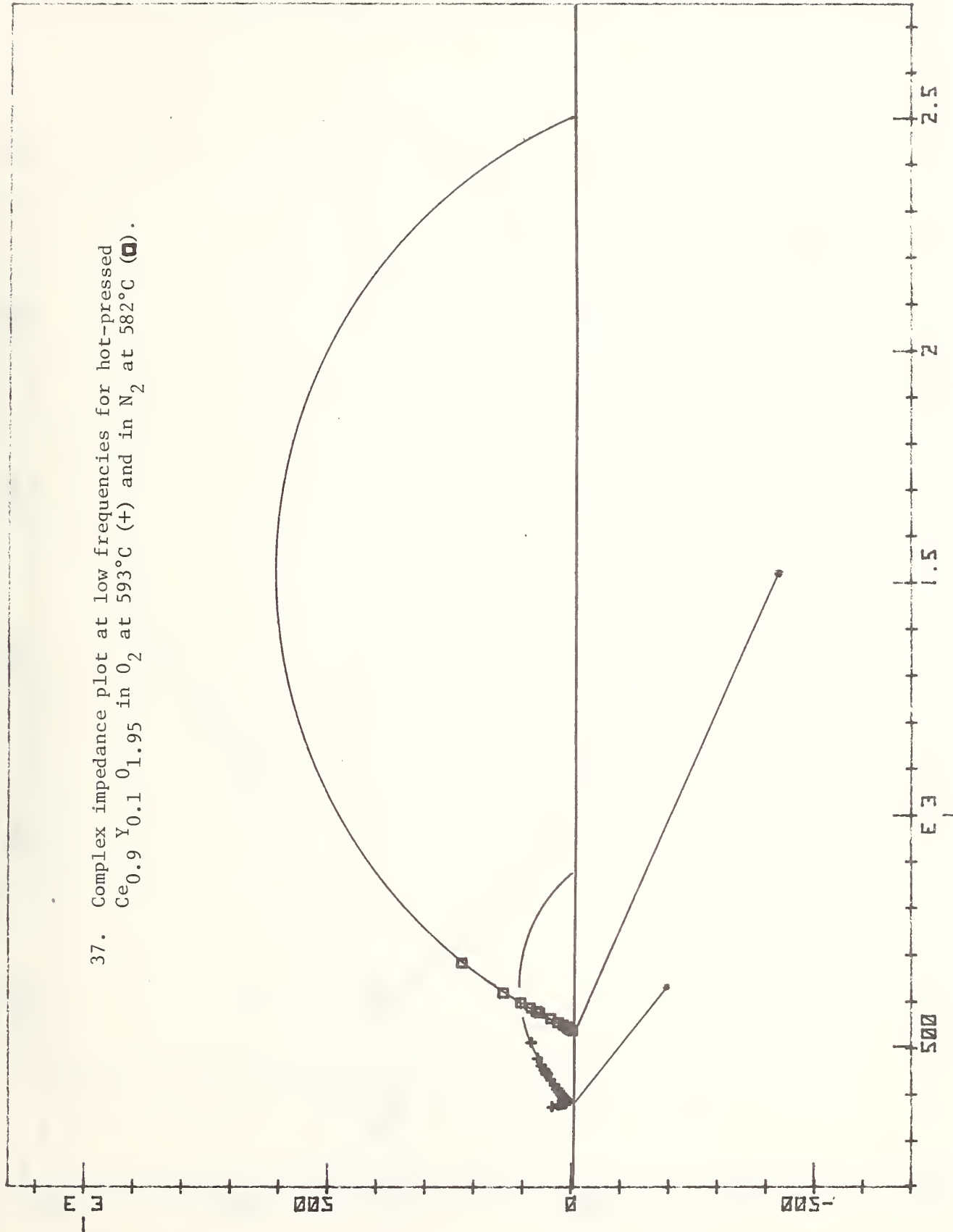
HFB 478 02 84

36. Complex impedance plots at low frequencies for hot-pressed
 $\text{Ce}_{0.9} \text{Y}_{0.1} \text{O}_{1.95}$ in O_2 at 478°C (x) and N_2 at 470°C (□).

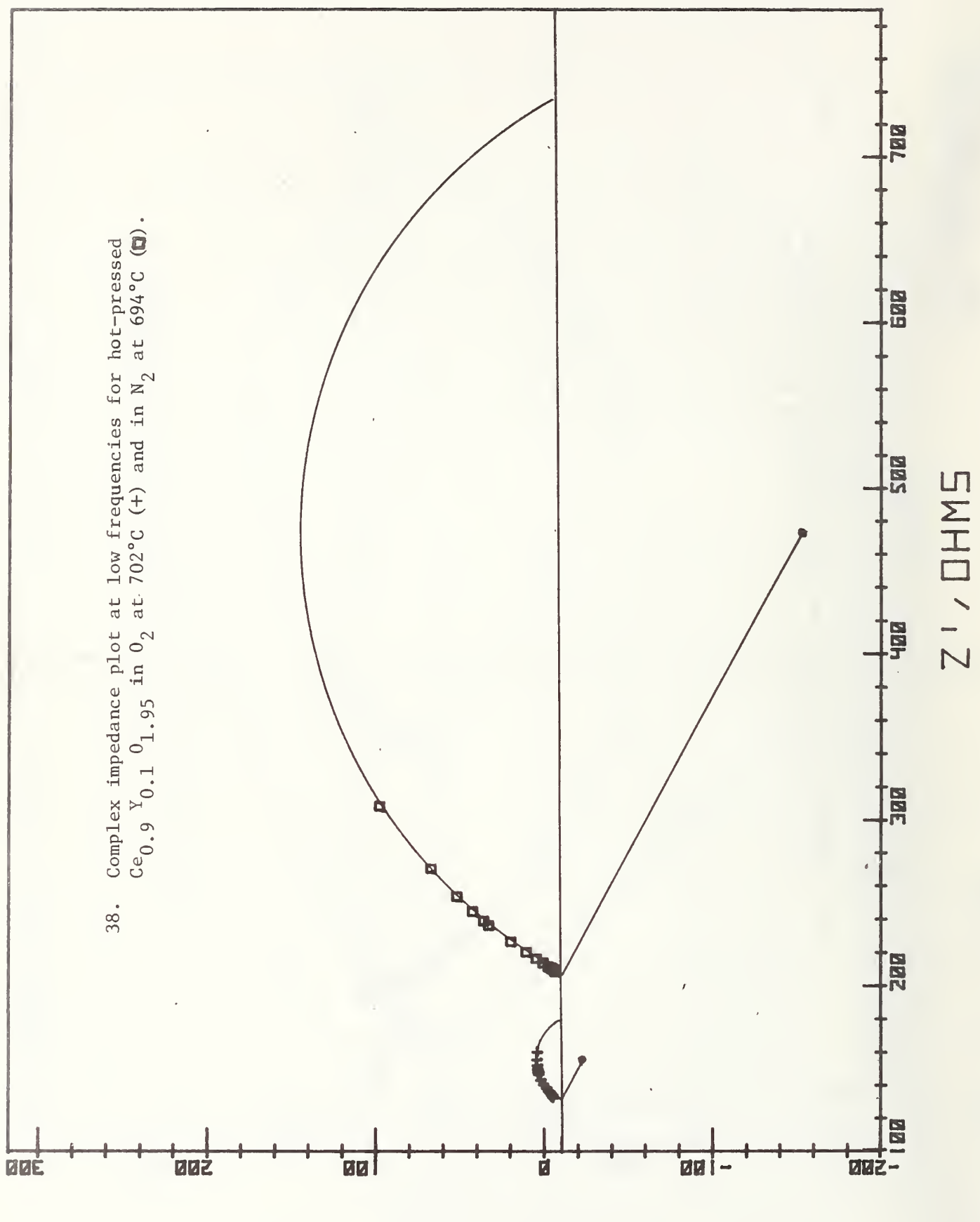


FEB 13, 1978

HPB 582 NZ 52



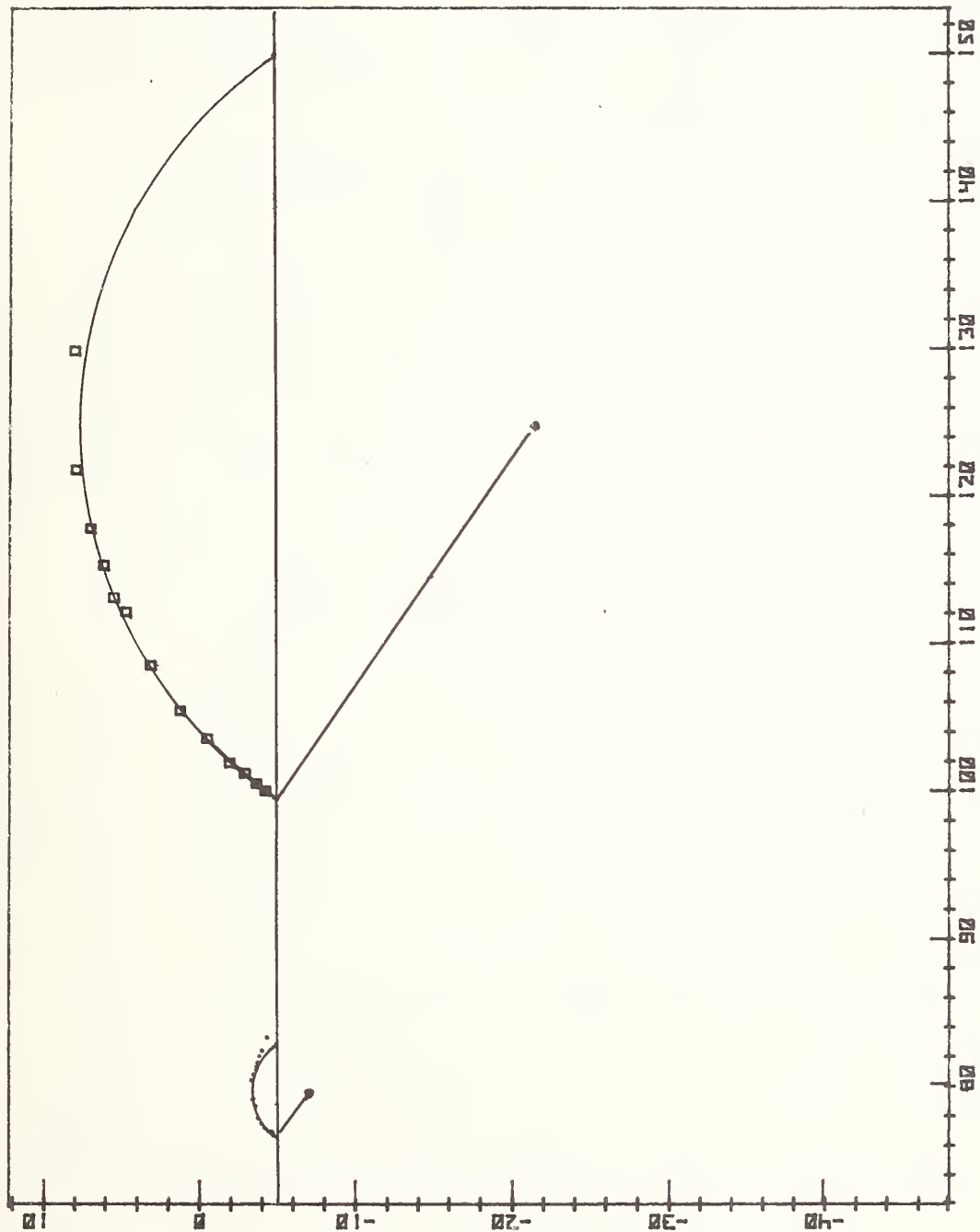
SHONZO



11

FEB 10, 1978

HPB 804 N2 94



IN HCL - Z

Z', HMS

39. Complex impedance plot at low frequencies for hot-pressed
 $\text{Ce}_{0.9} \text{Y}_{0.1} \text{O}_{1.95}$ at 804°C in O_2 (.) and in N_2 (□).

Nowick [25] for oxygen transport in the same composition. For comparison, Schouler et al [60] found the activation energy for ΔZ_{el} to be 198 kJ/mol for $Zr_{0.83}Y_{0.17}O_{1.92}$ with Ag electrodes whereas that for oxygen transport in stabilized ZrO_2 is about 125 kJ/mol [64]. It seems likely that ΔZ_{el} is not controlled by transport of oxygen in the electrolyte, but reflects some process on the interfaces.

On the other hand, C_z does not appear to depend on whether the atmosphere is oxygen or nitrogen, in agreement with the results of Schouler and Kleitz [63] reflected in Fig. 35. Furthermore, α does not appear to equal 1/2. This behavior is so at variance with the diffusion model discussed above and expressed in eqn (16) that we feel compelled to reject that model for the electrode arc and to continue the search for an explanation for the behavior.

The temperature dependence of C_z is expressed by

$$C_z = C_{zo} \exp (Q_z/kT) \quad (17)$$

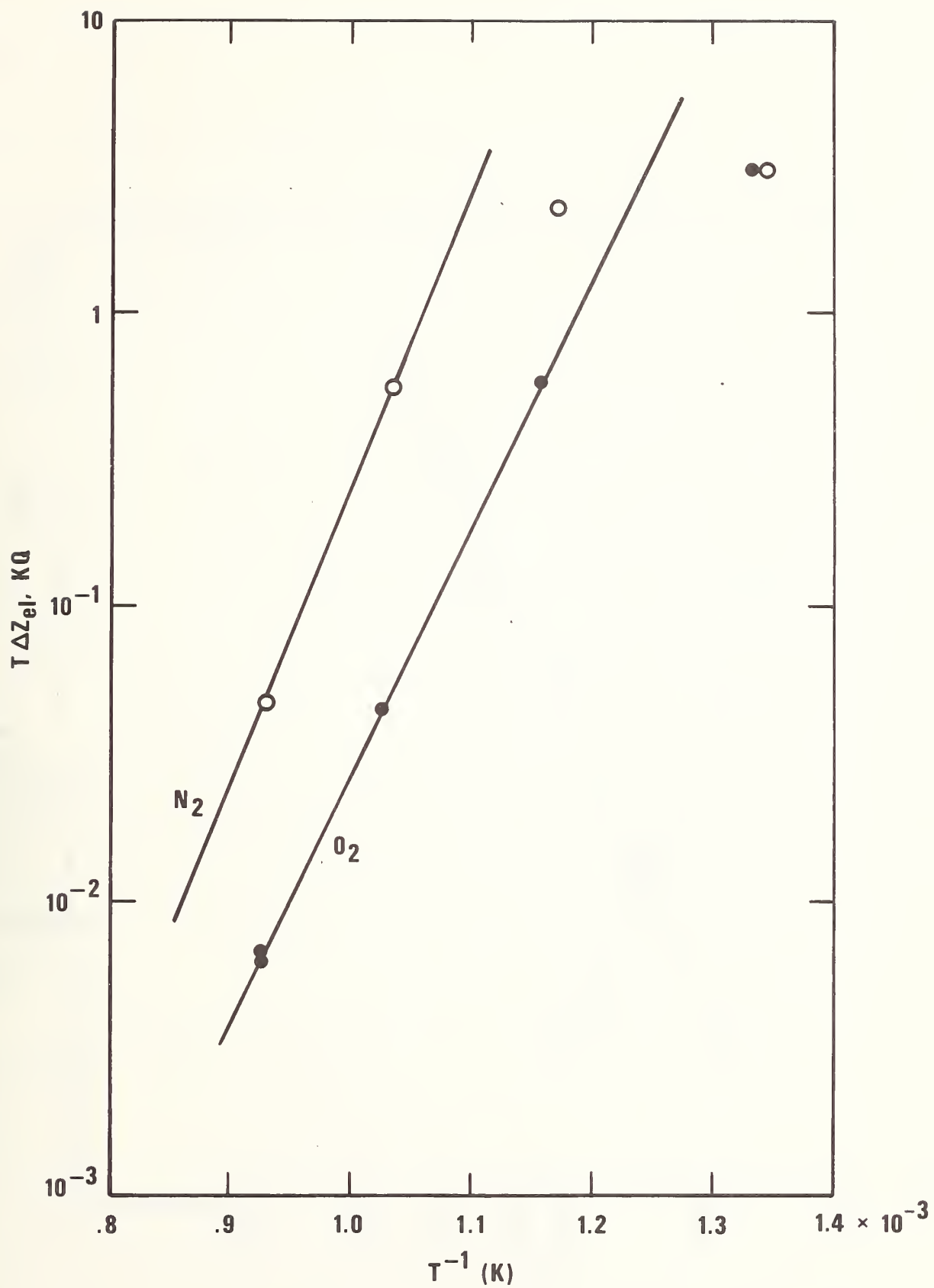
with the following values for C_{zo} and Q_z :

Atmosphere:	O_2	N_2
C_{zo} , μF	4.53	3.30×10^3
Q_z , eV	0.30	-.26

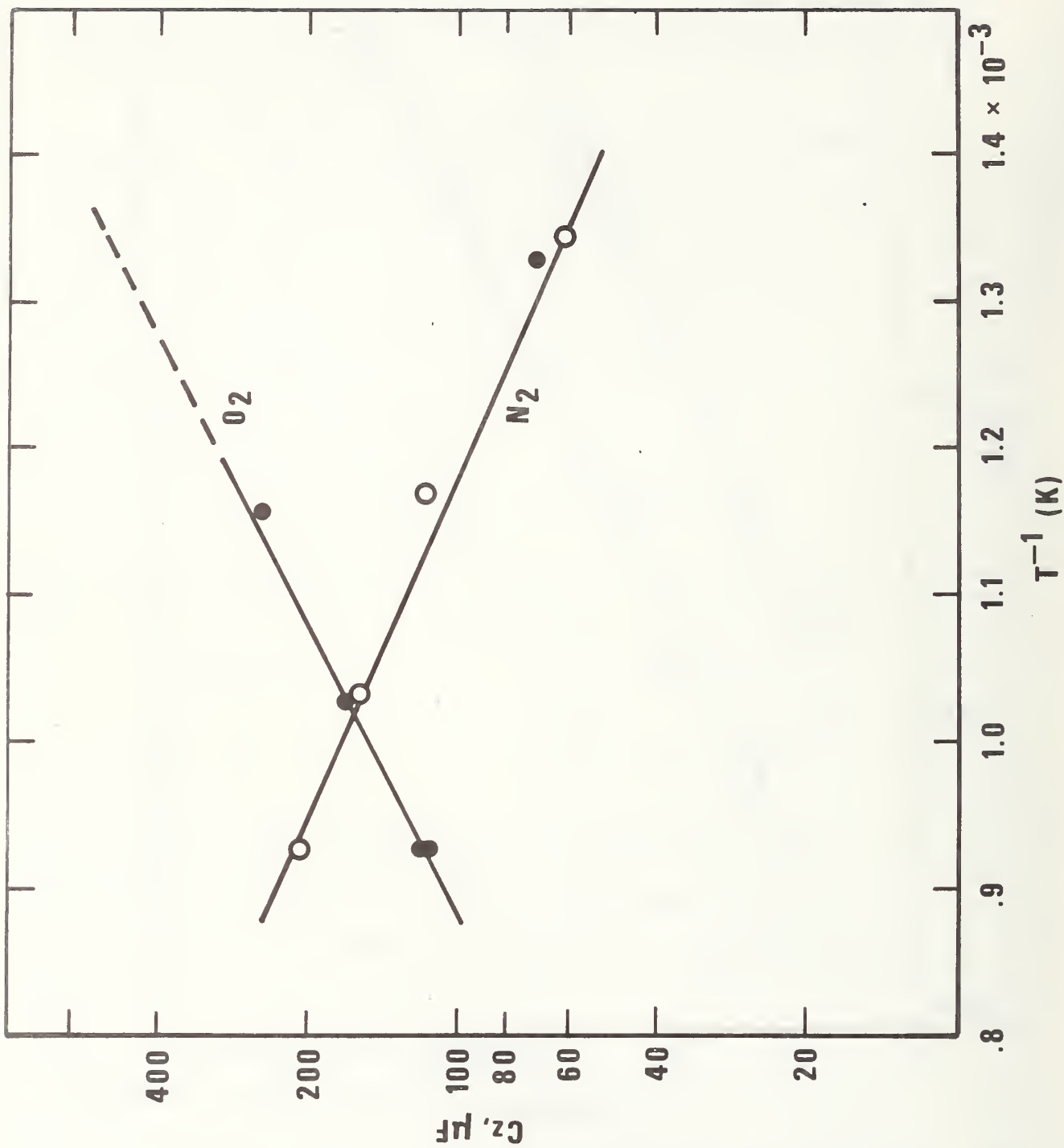
This reversal in sign of the activation energy may be related to the observation of Schouler et al [60] that Pt electrodes apparently have a layer of oxide in high oxygen pressures but not at low, in this temperature range.

Summary

The high frequency impedance arc appears to contain information about both the bulk resistance in the interior of the grains, R_B , and a contribution, ΔZ_{gb}^* , from inhomogeneities. The inhomogeneities may be



40. Temperature dependence of $T \Delta Z_{el}$ for $Ce_{0.9} Y_{0.1} O_{1.95}$ at $804^\circ C$ in Tank O₂ (●) and Tank N₂ (○).



41. Temperature dependence of C_z for $\text{Ce}_{0.9} \text{Y}_{0.1} \text{O}_{1.95}$ in tank O_2 and tank N_2 .

pores, second phase inclusions, or grain boundaries. The impedance data can be quite well fitted with the equivalent circuit of Fig. 26, using a desk-top computer with a least-squares technique. This part of the data appears to be independent of the atmosphere. More porous specimens show relatively more important inhomogeneity effects, as expected. For hot-pressed $\text{Ce}_{0.9} \text{Y}_{0.1} \text{O}_{1.95}$, in which inhomogeneities exist due to incomplete reaction, the variation with temperature of the inhomogeneous contribution, ΔZ_{gb}^* was greater than that of the bulk resistance, R_B . The effect of the former had essentially disappeared for temperatures higher than about 500°C. The bulk resistance (R_B) values give an activation energy in agreement with data in the literature [40, 41] for the same composition.

The sputtered Pt electrodes were found to be unstable, and to approach a steady-state condition only after high-temperature (800°C) anneal, and even then only very slowly. This aging results in an apparent increase in bulk resistance, as if it might involve a decrease in effective contact between the solid electrolyte and the electrode metal. On the other hand, it appears to have less influence on the measured geometric capacitance, C_g .

The low-frequency arc reflects reactions at the electrode-gas phase electrolyte interface. The impedance is well fitted by a Cole-Cole expression. An unsuccessful attempt was made to reproduce the experimental behavior by a model involving two parallel paths for the flow of oxygen, one in which the impedance is controlled by diffusion of oxygen atoms in the metal, giving rise to a Warburg impedance, and the other in which the impedance is a pure resistance dependent on the inverse square root of the oxygen pressure, as observed.

2.3 Battery Materials

Introduction

The advent of fast ion conductors, and particularly the discovery of the very rapid sodium ion transport in sodium beta-alumina, has opened up the possibility of relatively cheap, high power density, high energy density secondary batteries for automotive use, and also utility load-levelling. Solid-electrolyte batteries operating with liquid or solid electrodes obviate the problem of controlling dendritic growth on the electrodes, and shorting during the charge cycle.

Presently the leading candidates for automotive power batteries include sodium-sulfur, lithium-sulfur, and zinc-chlorine. All suffer serious drawbacks, including the fact that none has as high power- and energy-density as desirable. There is thus considerable interest in finding systems capable of operating with lithium or hydrogen under not-too-extreme conditions of temperature. To this end, a more complete knowledge of the basic mechanisms controlling the desirable properties in candidate materials is required. In the work on this program we are currently contributing to the understanding of the sodium ion transport mechanism in sodium beta-alumina.

2.3.1 Beta-Alumina

Introduction

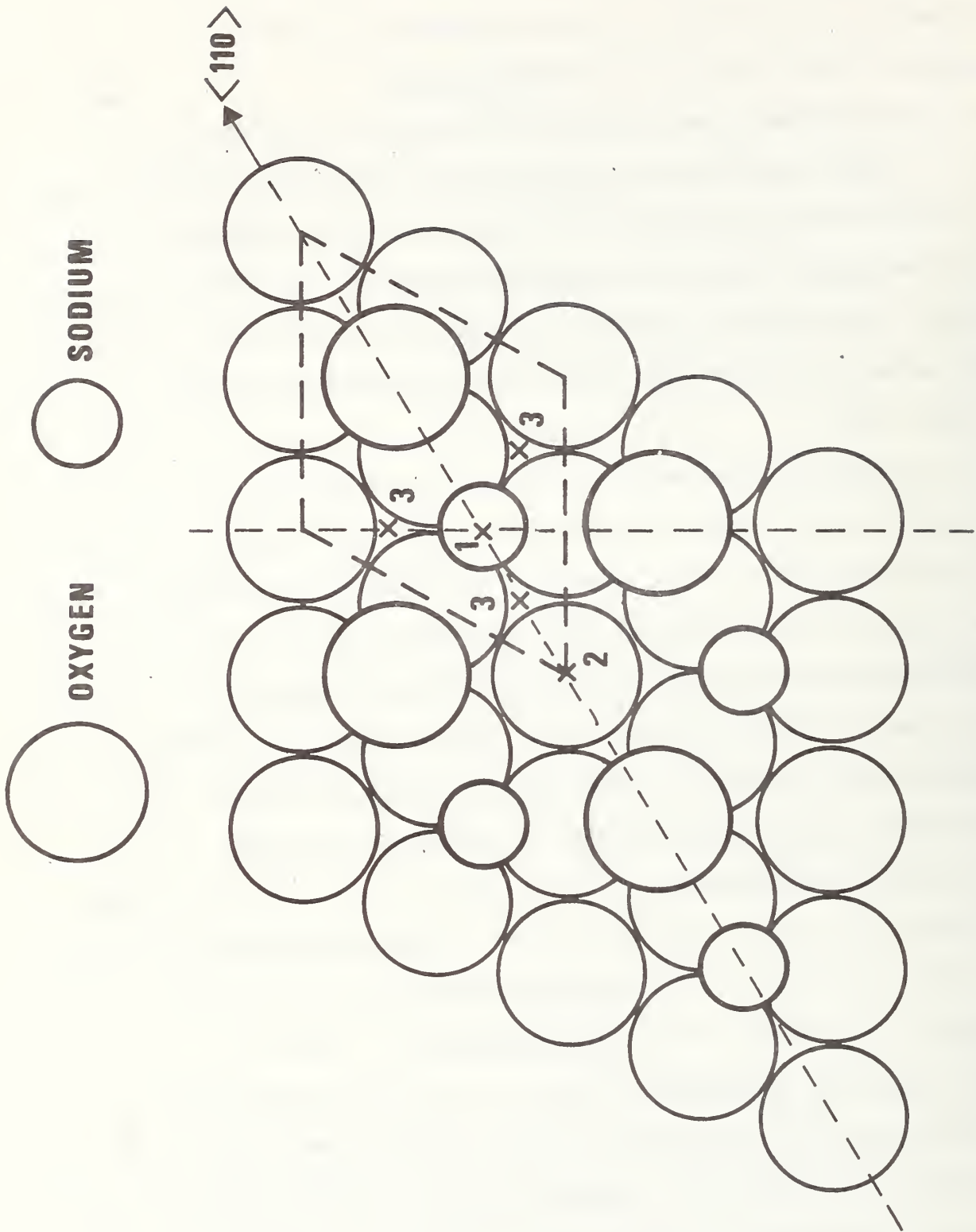
One of the leading candidate systems for high energy density and high power density batteries for transport use, and perhaps also utility load-following use, is the sodium/sulfur battery. The electrolyte is the ceramic, sodium beta-alumina, in which sodium ion conduction is very high with a transference number of essentially unity. Because of the

potential usefulness of these batteries there is great current interest in the properties of beta alumina, and particularly in the details of the mechanism by which the very rapid transport occurs.

The structure of beta-alumina is well known [65]. The unit cell consists of blocks of spinel structure formed by Al^{3+} and O^{2-} ions stacked in the c-axis direction and interspersed with special planes, parallel to the crystallographic basal planes, in which all the Na^+ and some O^{2-} ions reside, and in which the rapid Na^+ transport occurs. The ionic conduction mechanism can be viewed in a sense as two-dimensional transport in these planes.

The stoichiometric beta-alumina composition is $\text{Na}_2\text{O} \cdot 11 \text{Al}_2\text{O}_3$. However, this does not actually occur, and real specimens contain an excess of 20-35% Na_2O [66]. There appears to be proportionality between the ionic conductivity and this excess Na^+ concentration [67], and it is now thought that these excess ions occupy interstitial sites among the regular Na^+ lattice sites and are responsible for the rapid Na^+ transport [68]. Models of this transport in terms of liquid-like motion of the Na^+ ions have been proposed [69]; however, we will discuss our work using the point defect description.

Two defect models have been proposed [68]. In the description that follows, "cell" will refer to the translation repeat unit of one of the two conducting planes in the crystallographic unit cell. Figure 42 illustrates this "cell" in schematic fashion. In the simple interstitial model [70] the excess Na^+ ions constitute the interstitials and occupy the anti Beevers-Ross (aBR) sites. Transport involves an interstitialcy motion in which the interstitial moves from the aBR site to an adjacent regular Na^+ site (Beevers-Ross, or BR site) while the occupant moves to an aBR site in an adjoining "cell" and becomes the interstitial.



42. Arrangement of ions in the conducting plane of beta-alumina. Dotted lines enclose "cell"; two such "cells", on adjacent conducting planes, are included in the crystallographic unit cell. Na^+ ion sites are: 1, BR site; 2, aBR site; and 3, MO site. Mirror planes described in text are indicated by dashed lines.

In a second defect model [71], an interstitial (excess) Na^+ ion and a regular Na^+ ion share a "cell", both occupying mid-oxygen (MO) sites, leaving the BR and aBR sites both vacant. Transport occurs when either ion of this split interstitial "dumb-bell" moves through the adjacent aBR site to an adjoining "cell", where it and the regular Na^+ of the new "cell" form a new split interstitial.

In order to help to identify which of these processes is more likely to be responsible for Na^+ ion transport, we have performed an internal friction experiment on a single crystal of sodium beta alumina. In this experiment an alternating tensile-compressive stress of approximately fixed frequency is applied along the $\langle 110 \rangle$ crystallographic direction and the energy loss per cycle (expressed as the inverse of the quality factor, Q^{-1} , of the resonating crystal) observed as a function of temperature. A prominent peak in the TQ^{-1} vs T plot signals a process in which mobile ions are moving under the stimulus of the applied stress.

The first defect model described above, in which the Na^+ interstitial occupies an aBR site and displaces a regular Na^+ ion which in turn moves to another aBR site (interstitialcy mechanism), would not produce internal friction. The result of the unit transport step would be the disappearance of an interstitial from one aBR site and the appearance of an interstitial at an adjacent one. Since the aBR sites are crystallographically equivalent by virtue of a unit translation, an equivalency that is not removed by a homogeneous stress, no motion from one such site to another would be induced by the stress, and therefore no internal friction would be observed.

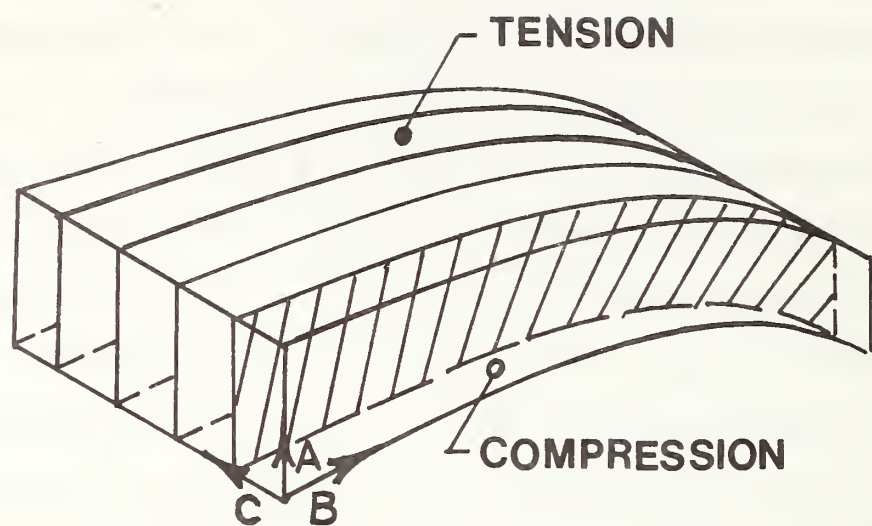
On the other hand, the second mechanism, involving the split interstitial on M0 sites, could produce an internal friction peak. There are three crystallographically equivalent orientations for the split interstitial, related by a pair of mirror planes parallel to the c-axis. (cf. Fig. 42) Application of a $\langle 110 \rangle$ compressive stress removes one mirror plane and reduces the set of three equivalent orientations to two sets, one composed of a pair of orientations still equivalent by virtue of the remaining mirror plane and symmetrical disposed about the $\langle 110 \rangle$ axis along which the stress has been applied. When the extra Na^+ ion moves from one cell to another in the transport process, the effect as described above is to move the split interstitial from one cell to the next. Some of the jumps of this kind involve a reorientation of the new split interstitial relative to the old. Such jumps would be stimulated by the stress and could therefore contribute to the internal friction as well as to the transport. In addition, reorientation of the split interstitial within the "cell" could also contribute to the internal friction, but, in this case not to the transport. The activated state for this non-transport reorientation is probably not very different from that for the transport process. Hence the split interstitial model could result in very similar, but not necessarily identical, activation energies and pre-exponential factors for the transport and internal friction experiments. The observation of internal friction in the experiment reported here thus tends to eliminate the simple interstitialcy mechanism and to support the split interstitial model as most likely to be important to the Na^+ transport process.

Experimental

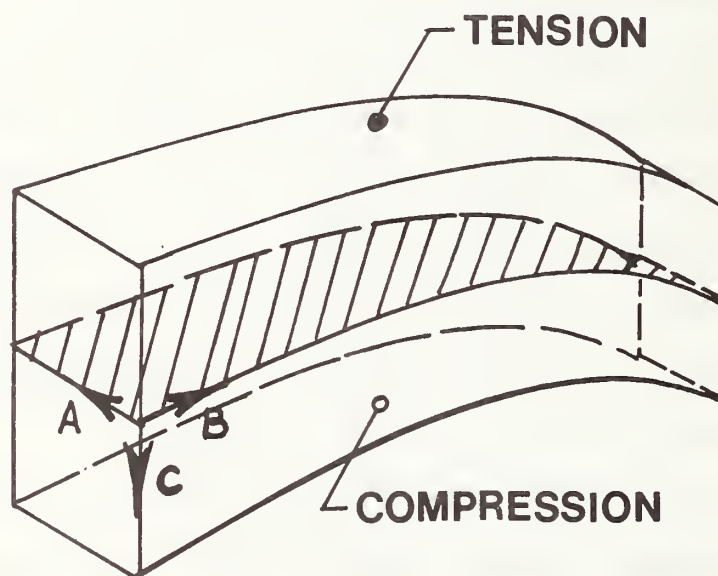
Internal friction data in the temperature range from 90K to above room temperature were collected on a sample of single crystal $\text{Na } \beta\text{-Al}_2\text{O}_3$. The sample was cut from a boule grown from the melt by the Crystal Products Department of the Union Carbide Corporation. Such crystals typically contain 15-35% excess Na^+ . The sample was a bar of dimensions $7.82 \times 1.17 \times 0.82$ cm, with the long dimension within 1/2 degree of the $\langle 110 \rangle$ crystallographic (and also crystal growth) direction. The c-axis was parallel to the 1.17 cm dimension. Cutting was performed with a diamond saw under pump oil, and the crystal was stored and handled in an argon atmosphere to protect it from atmospheric water. The bar was resonated in the fundamental flexure mode. Because of the rectangular cross-section, the frequency exhibited by this mode when the displacement was parallel to one side of the bar was different from that when displacement was parallel to the other. Figure 43 shows schematically the flexural strain generated in the bar, and the orientation of the conducting planes relative to this displacement, for the two orientations. In both cases a tensile-compressive stress is generated oriented along the $\langle 110 \rangle$ crystallographic direction. However, there is additionally a shear tending to produce slip on planes which are parallel to the conducting planes for the 16 kHz resonance but which are perpendicular to the conducting planes for the 12 kHz resonance.

To achieve this flexural vibration, the sample was suspended in a temperature-controlled, evacuable chamber (Figure 44) suspended (by fine fibers) near one end from a phonograph cutting head and near the other from a phonograph pickup with a Rochelle salt transducer. The suspension fibers were of glass (150 μm diameter) coated with a thin layer of plastisol. They were located on the crystal near the nodes of the fundamental flexural vibration. The temperature was measured with a

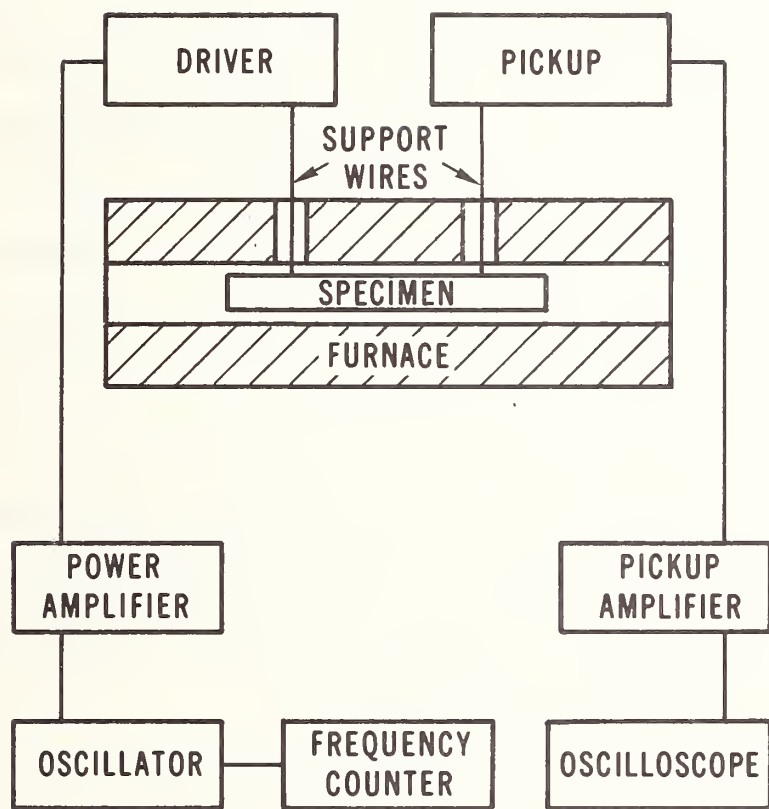
12 KHz VIBRATION



16 KHz VIBRATION



43. Flexural strain produced in specimen bar for two orientations.



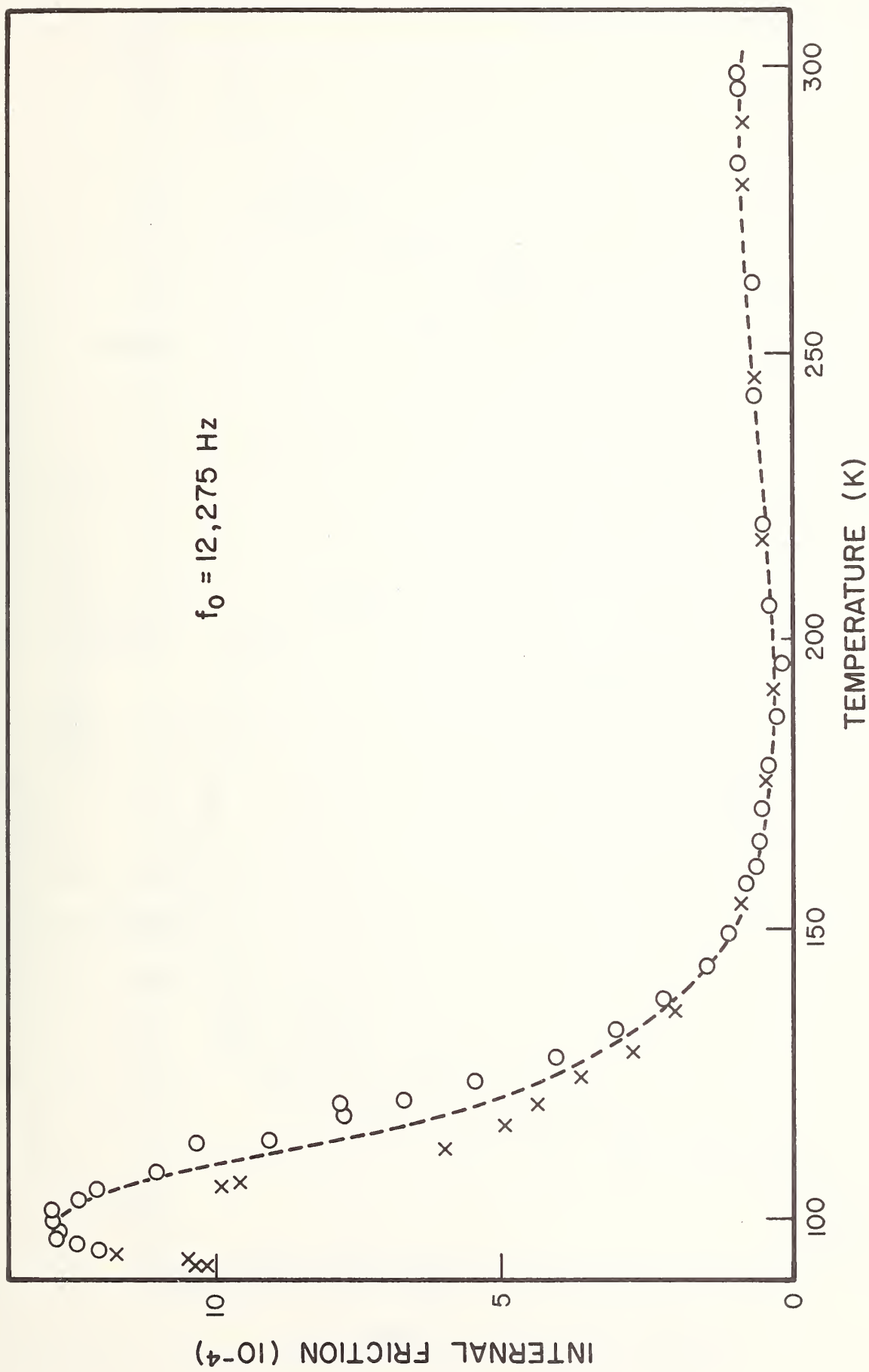
44. Experimental arrangement for internal friction experiment.

platinum resistance thermometer calibrated at the National Bureau of Standards, held near to but not touching the specimen. The thermometer was encased in plastic to simulate the thermal transport properties of the specimen. Temperatures below room temperature were varied by passing cold nitrogen gas and liquid nitrogen through coils surrounding the specimen chamber. Cooling and warming rates of 1/2 to 1 K per minute were used during the measurements.

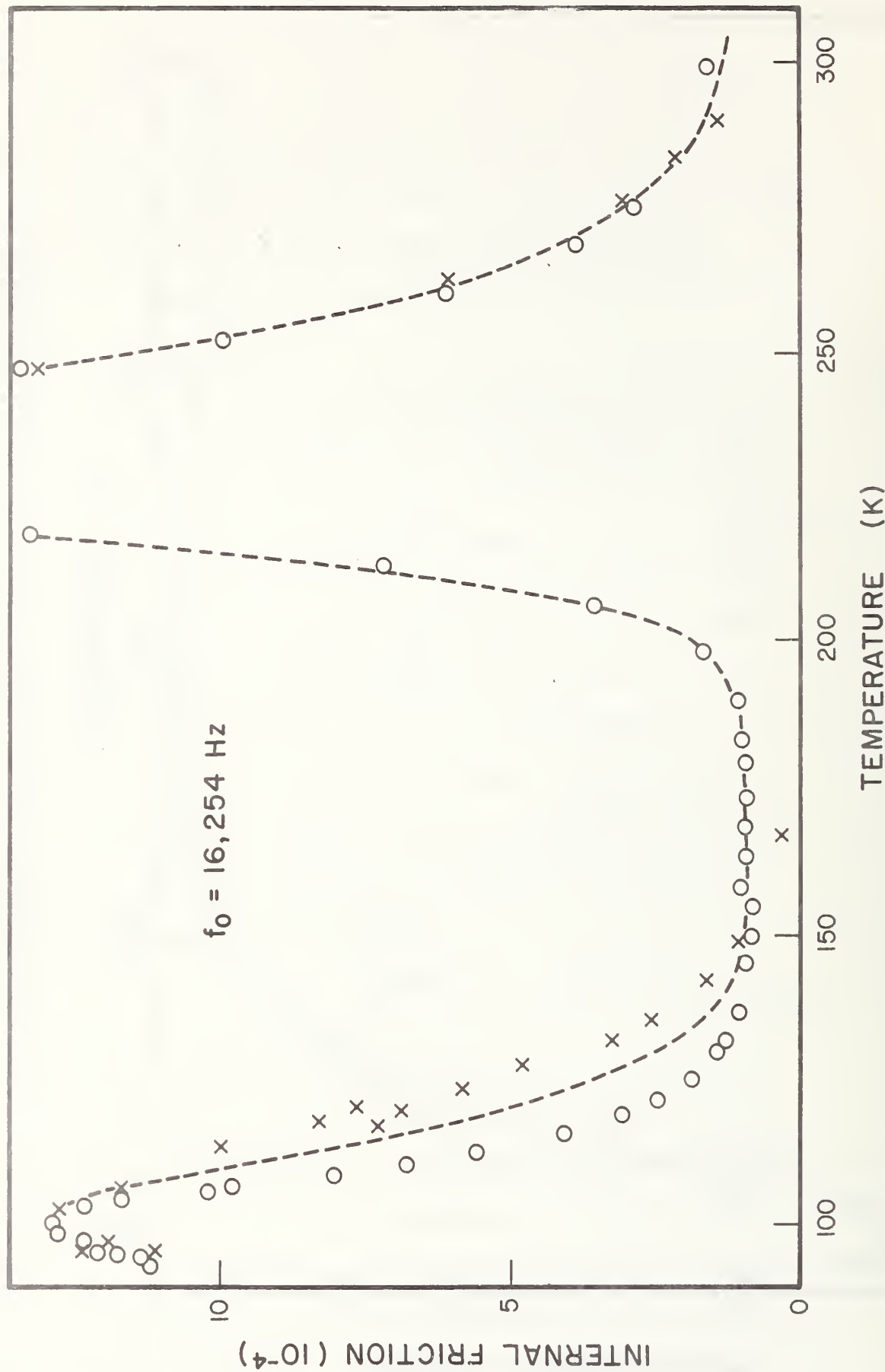
The internal friction data were obtained by a variation of Forster's method, using a new instrument developed at the National Bureau of Standards by Parks and Linzer [72]. Briefly, a voltage-controlled oscillator is inserted into a feed-back loop designed to locate the frequency of maximum signal output from the pickup, thus allowing a continuous measurement of the resonance frequency as the temperature was varied. A phase-lock detector yielded a direct measure of the internal friction (Q^{-1}) by measuring the frequencies at which some predetermined shift in phase relative to the phase at resonance occurred. In practice phase shifts of 45, 22.5, and 11.25 degrees were used to check the consistency of the results. All values reported here are for a 22.5 degree phase shift and represent the mean of 10 readings.

Results

The two expected flexural resonances were observed. At room temperature the fundamental resonance frequencies were 12.276 kHz, for the specimen lying flat with the larger cross-sectional dimension (width) horizontal (12 kHz orientation), and 16.257 kHz with the width vertical (16 kHz orientation). Figures 45 and 46 display the internal friction data (TQ^{-1}) over the temperature range from about 90K to room temperature. There is a ± 6 K discrepancy in temperature between the data taken with rising and falling temperatures, such that the thermometer leads the



45. Internal friction for the sodium beta-alumina specimen with the width horizontal. Falling temperature, x. Rising temperature 0.



46. Internal friction for the sodium beta-alumina specimen with the width vertical. Falling temperature x. Rising temperature o.

specimen. This is due to the fact that the thermometer could not directly contact the specimen. This discrepancy was largest in the middle of the temperature range where the rate of rise or fall was largest.

For the 12 kHz orientation, with the width horizontal (Fig. 45), there is a single strong internal friction peak near 100K. With the width vertical (16 kHz orientation) an additional very strong peak occurs near 235K (Fig. 46). The orientation suggests that this peak arises from the effect of the shear component of the stress, probably interacting with small cracks parallel to the conducting planes observed in the large faces of the crystal. Annealing the crystal in vacuum for 3 hours at 125°C to reduce the H_2O content [73] had no influence on the peak near 100K in either orientation, but reduced the peak at 235K with the 16 kHz orientation to less than 50% of its former amplitude. This higher temperature peak will not be discussed further.

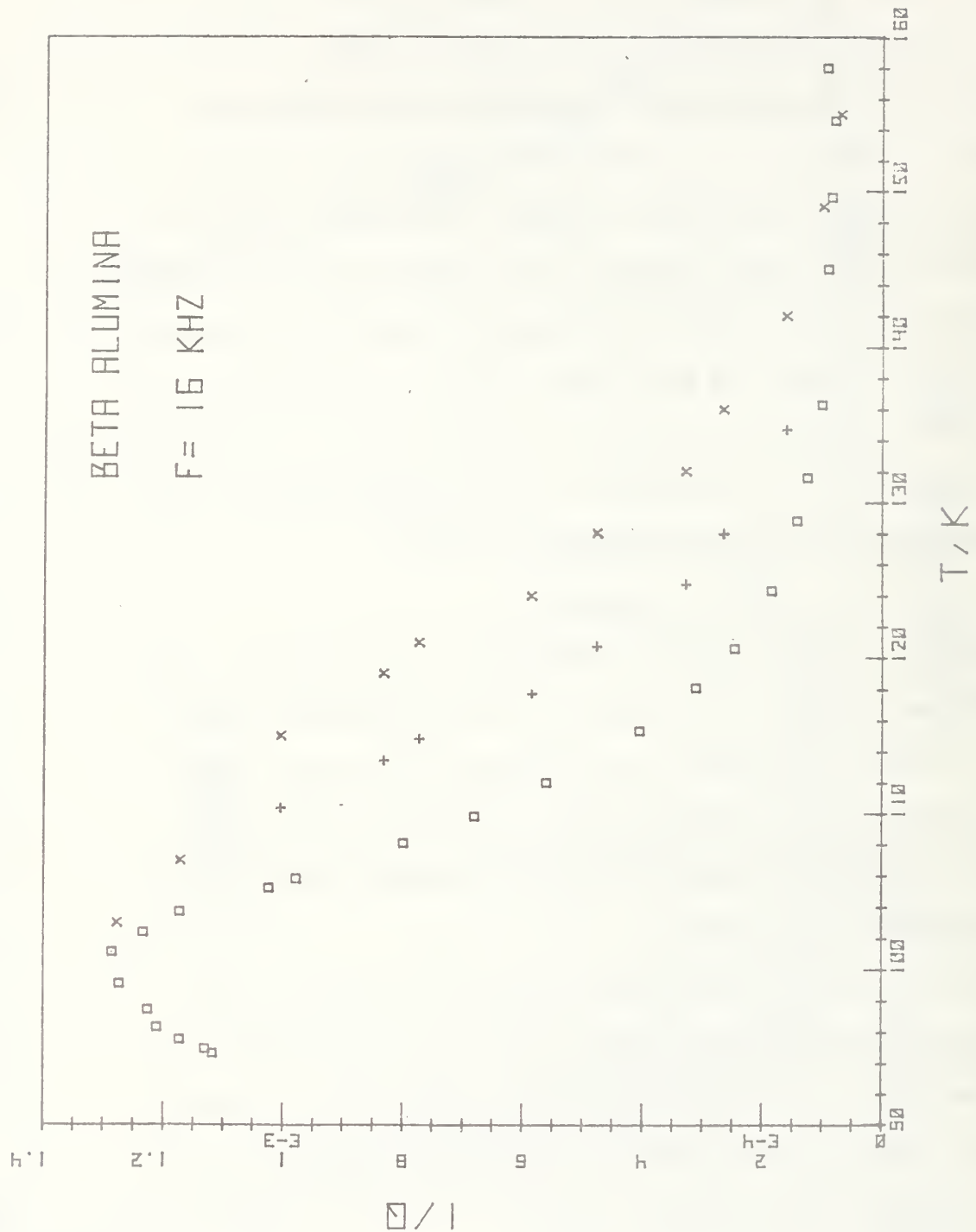
Analysis

Because of the large temperature uncertainty in the middle of the range, a detailed analysis of the internal friction peaks would not be worthwhile. However, an analysis of the variation of the peak temperature, when combined with the similar data of Barmatz and Farrow [74], would help in comparing the processes producing internal friction with those producing Na^+ ion transport.

The following scheme was adopted to minimize the impact of the temperature hysteresis exhibited in Figs. 45 and 46 on the estimate of the peak temperature. It was observed that the data taken with rising temperatures could be fit very well (Fig. 47) with a hyperbolic secant:

$$TQ^{-1} = A \operatorname{Sech} [B(T^{-1} - T_m^{-1})]. \quad (18)$$

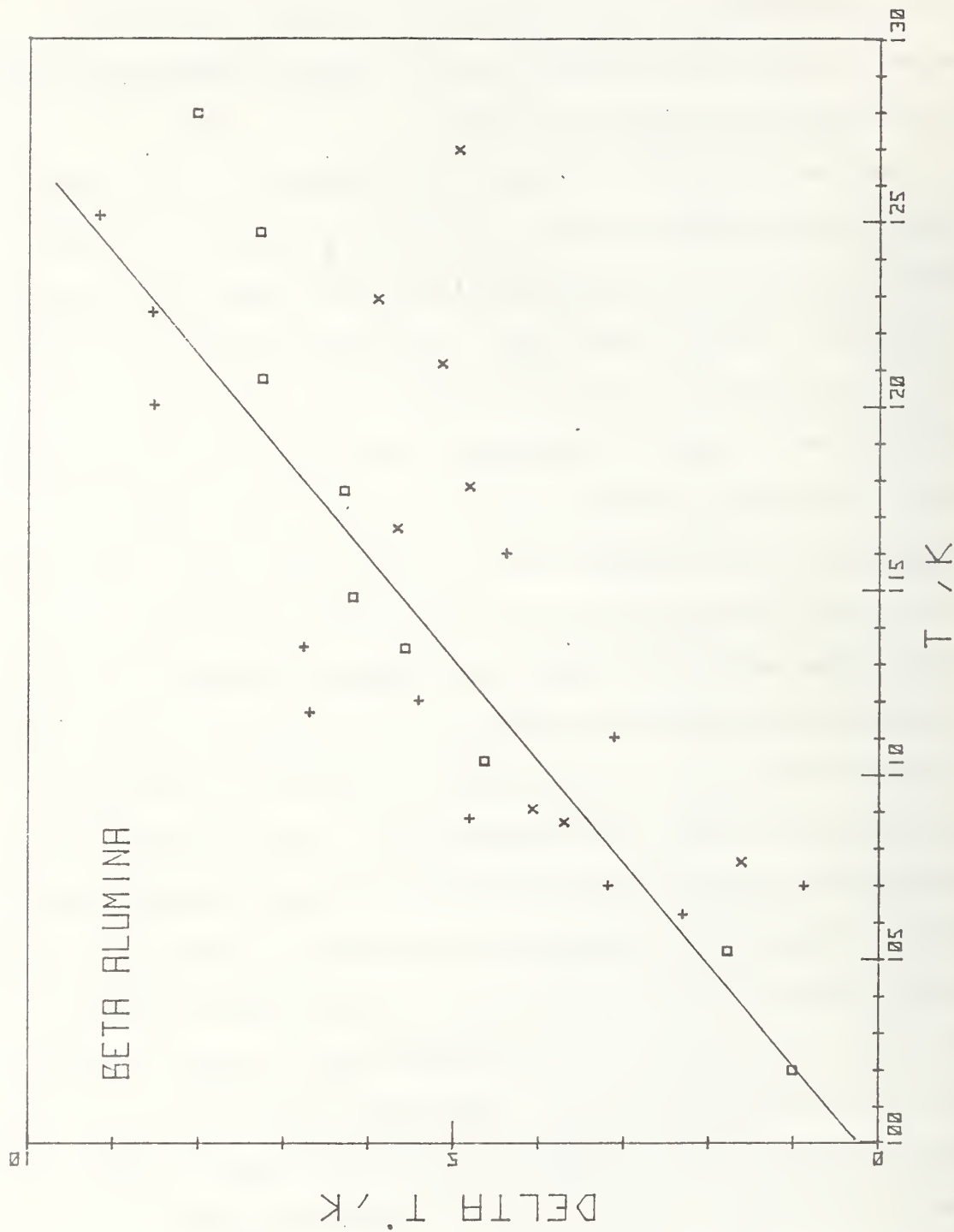
Using this as an interpolation formula for the rising-temperature data, an estimate for the true temperature corresponding to equilibrium was



47. Internal friction for the sodium beta alumina specimen with the width vertical, details of the temperature variation. Falling temperature \square , estimated equilibrium data \times , rising temperature $+$.

obtained as the mean of the temperature of a data point taken with falling temperature and the temperature of the point on the rising temperature curve at the same TQ^{-1} value. Figure 47 shows these estimated equilibrium data points as pluses.

Equation 18 was found to produce an excellent fit to the estimated equilibrium data points as well, and it was therefore fitted to these data by least squares, minimizing the sum of the squares of the deviations in TQ^{-1} from the fitted curve. The estimated standard deviation in the peak temperature, T_m , due to random error is about 0.2K. In addition, however, there is a systematic error because the equilibrium data may not be correctly represented by the mean of the rising and falling data. This systematic error in choosing the correct temperature for each equilibrium data point is bounded by the experimental values for the rising and falling temperatures. Figure 48 displays the maximum systematic error (one half the distance on the temperature scale of Fig. 47 from the rising to the falling temperature curve) as a function of the temperature for each equilibrium data point. The error decreases as the temperature goes down because the rate of rising or falling of the experimental temperature decreases near the end of the temperature range and the rising and falling temperatures of the experiments performed with temperature converge on the equilibrium values. Figure 48 shows that at the peak temperature (100 - 103K) the systematic error must be less than $\pm 1K$, and in reality must be considerably less. We adopt values of about $\pm 1K$ at 102K and $\pm 0.6K$ at 101K as the maximum values for the systematic temperature error.



48. Maximum systematic temperature error in internal friction data.

The extreme values for T_m including this maximum value for the systematic error are:

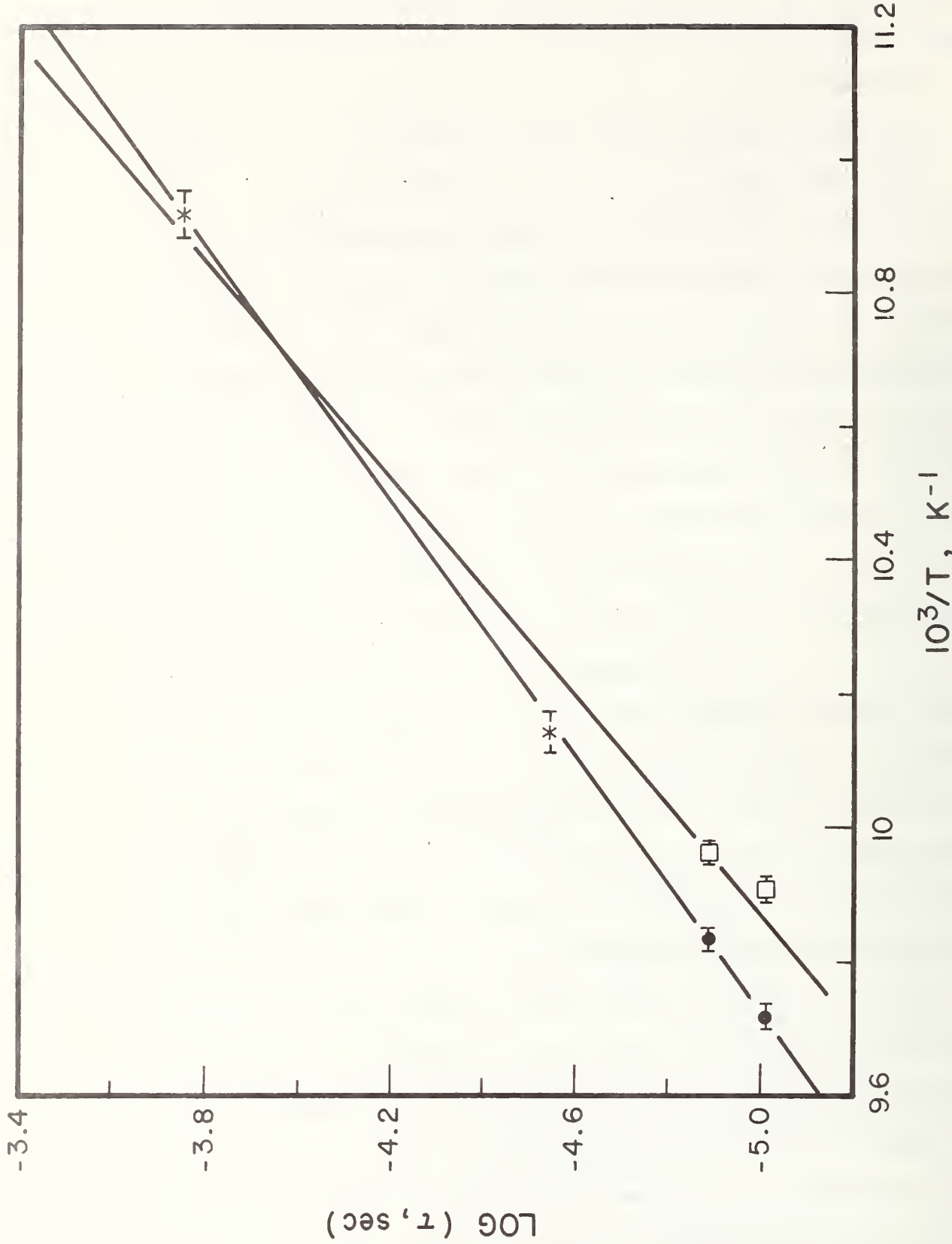
Frequency, kHz	12.34	16.39
T_m , Upper limit, K	101.6	102.9
T_m , Lower limit, K	100.4	100.9

The relaxation times obtained from these data combined with the very similar data of Barmatz and Farrow [74] obey the Arrhenius equation quite well (Fig. 49). Least-squares fits were made to the two sets of four experimental points (the two values of Barmatz and Farrow together with either our upper or our lower limiting values), weighting them according to the stated random errors in the peak temperatures and assuming no errors in the frequencies. These fits gave two limiting pairs of values for the activation energy and pre-exponential factor, namely 20 kJ/mol and 5.6×10^{-16} s, and 23 kJ/mol and 7.4×10^{-18} s.

Discussion

These activation energies are quite close to those reported [68] for various Na^+ transport processes 16.4 kJ/mol, and it seems very probable that the internal friction reflects the same processes. However, the small discrepancy of 6 kJ/mol persists and may be real. Furthermore, the pre-exponential factors appear to be unrealistically small, and may be hard to reconcile with any realistic model.

The simple interstitialcy model discussed above cannot give rise to internal friction, and can be ruled out in our experiment. The split interstitial is consistent with our results. A detailed comparison can be made between the behavior of this model and the various experimental results. We use here the formalism of the relaxation mode analysis [75] to calculate the ionic conductivity and the relaxation frequency for internal friction. Work is still continuing on calculating the Na^+ tracer diffusion coefficient.



49. Arrhenius plot for internal friction in sodium beta-alumina. Data of Barmatz and Farrow (Ref. 74) \times , our data with maximum systematic error added x, and subtracted x. The error bars are reported random error standard deviations.

Figure 50 displays a block of "cells" in which only the MO and aBR sites are shown. In the central cell the 3 orientations of the split interstitial are shown, and the directions of possible interstitial jumps indicated by arrows. In the surrounding cells the orientations of the new split interstitials reached by the jumps are shown by heavy lines. According to this figure, the rate equations governing the occupation probabilities P_i of the various orientations for the split interstitials, neglecting defect interactions except for site availability, are

$$\begin{aligned}\dot{P}_1 &= -\frac{3}{2} \Gamma P_1 + \frac{3}{4} \Gamma P_2 + \frac{3}{4} \Gamma P_3, \\ \dot{P}_2 &= \frac{3}{4} \Gamma P_1 - \frac{3}{2} \Gamma P_2 + \frac{3}{4} \Gamma P_3, \\ \dot{P}_3 &= \frac{3}{4} \Gamma P_1 + \frac{3}{4} \Gamma P_2 - \frac{3}{4} \Gamma P_3,\end{aligned}\tag{19}$$

$$\text{where } \Gamma = v(1-p) + (4/3)\mu, \tag{20}$$

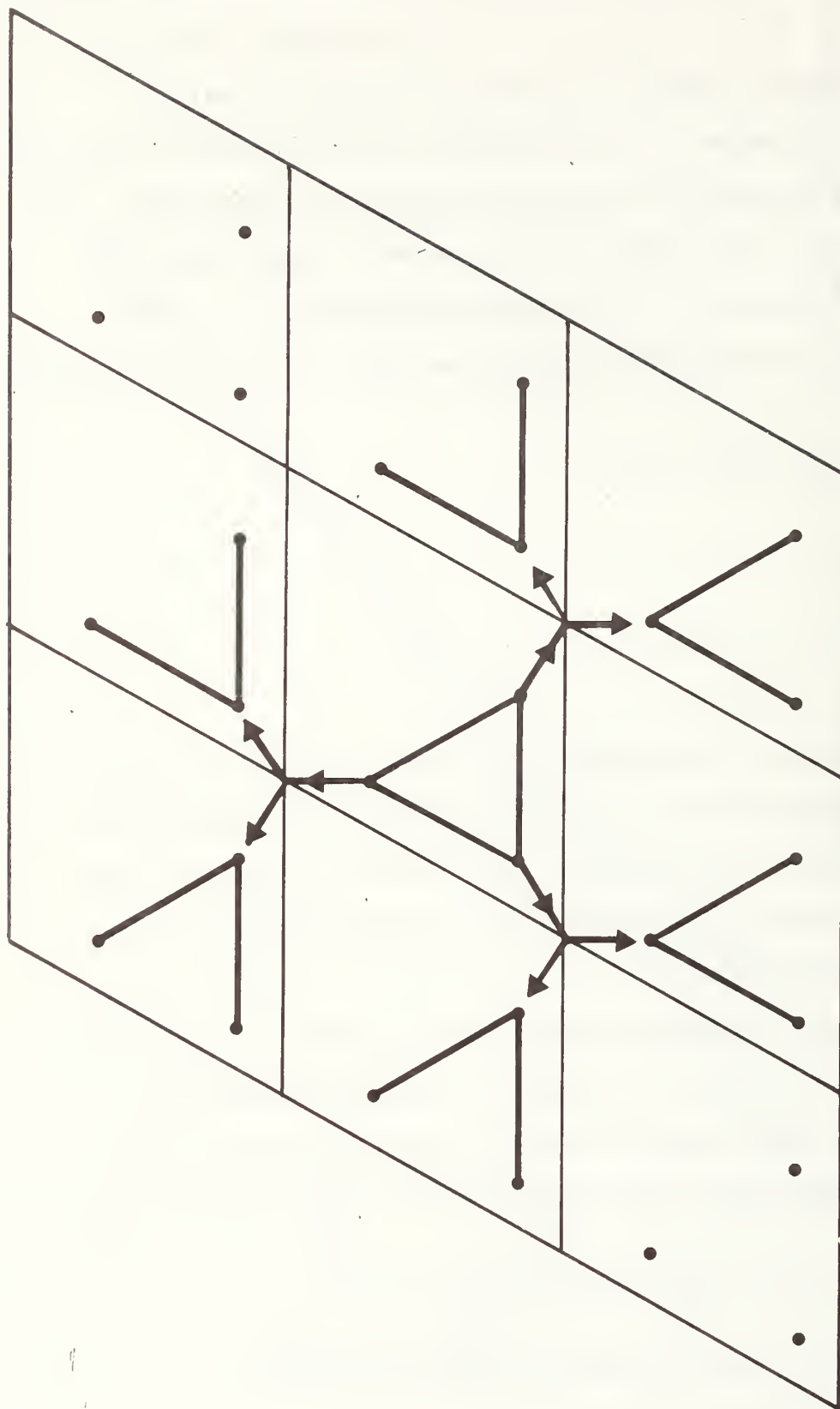
with v the probability of one member of the split interstitial jumping into an empty adjacent "cell" and μ the probability of its jumping into the vacant MO site in its own "cell". The fraction of excess Na^+ ions is p , so that $(1-p)$ is the probability that a given adjacent cell does not contain an interstitial.

If we define a 3-dimensional vector space in terms of the 3 orientations so that the coordinates represent the occupation probabilities of the orientations, then a general solution to eqns (19) in the undriven case can be written

$$\underline{P} = \frac{1}{\sqrt{3}} \left\{ \frac{1}{\sqrt{3}} (1,1,1) + \frac{f_2}{\sqrt{6}} (1,1,-2) + \frac{f_3}{\sqrt{2}} (1,-1,0) \right\} \tag{21}$$

where the three terms represent three relaxation modes, and

$$f_i = f_{i0} \exp(-\lambda_i t), \tag{22}$$



50. Arrangement and jumps of split interstitials from one "cell" to another in sodium beta-alumina. AB sites lie at intersections of trigonal network; MO sites are indicated by small filled circles. Lines connecting MO sites indicate possible split interstitials and arrows the paths from one "cell" to the next.

in which λ_i^{-1} is the relaxation time for the i th mode and f_{io} is determined by the applied stress and the response of the material to it.

In particular, a $\langle 110 \rangle$ stress will excite the second mode but not the third (The first is the equilibrium mode). For this second mode the relaxation time is given by

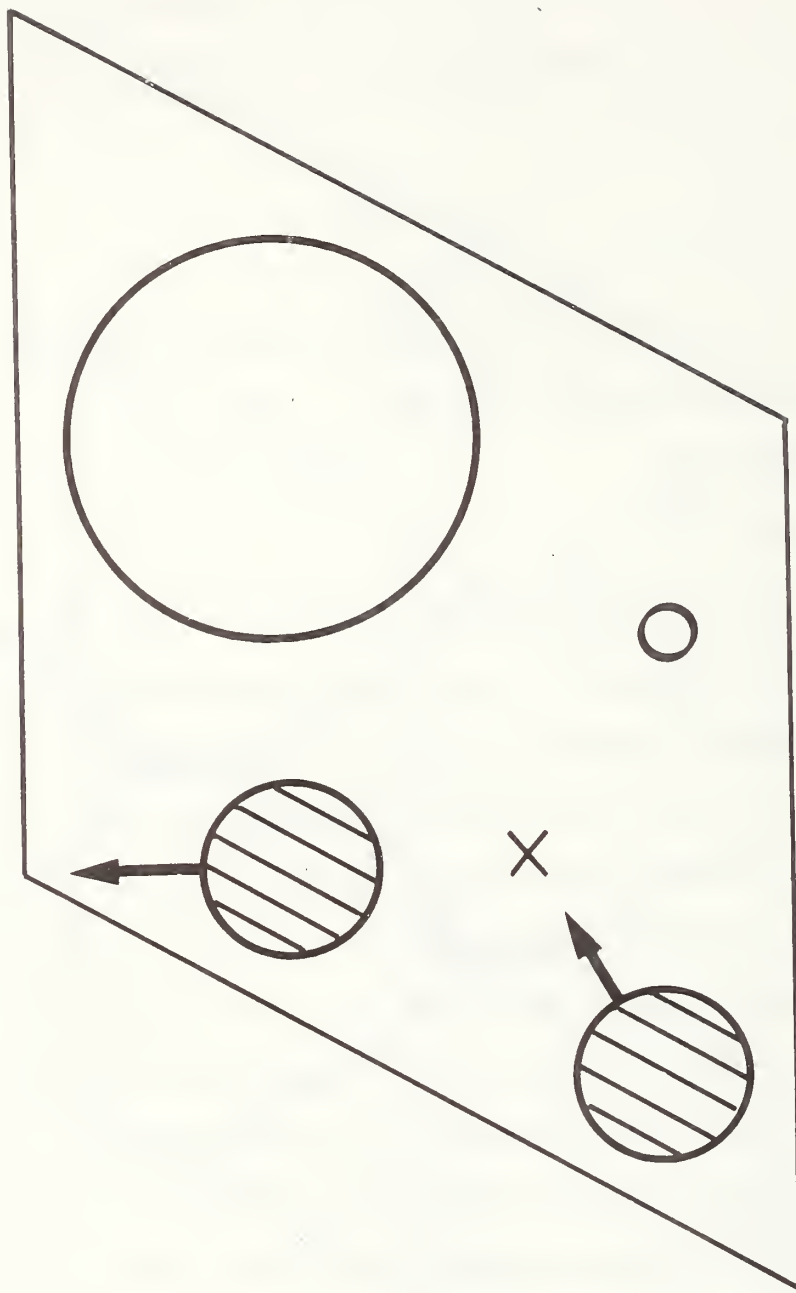
$$\begin{aligned}\tau^{-1} &= \lambda = 9\Gamma/4 \\ &= \frac{9}{4} \nu(1-p) + 3\mu\end{aligned}\quad (23)$$

In this equation we will assume that ν and μ are given by the usual Arrhenius expressions for activated processes:

$$\nu = \nu_0 \exp(-Q_\nu/kt) \quad (24)$$

$$\mu = \mu_0 \exp(-Q_\mu/kt) \quad (25)$$

To calculate an expression for the Na^+ ionic conductivity, we again return to the relaxation modes, but this time in the presence of an electric field sufficiently small such that only linear terms in the changes induced by the field in the occupation probabilities need be retained. To proceed we adopt a more detailed idea of the movement of the split interstitial toward the activated state. Following Wang et al [71], we assume a coupled motion in which one Na^+ ion moves into a nearby aBR site while the other moves to the BR site in the same cell (Fig. 51). This is assumed to be the activated state for both transport and reorientation without transport. Transport occurs when the Na^+ ion at the aBR site moves on into another cell, reorientation without transport when it moves back again to the MO site from which it came, the other Na^+ ion then moving away from the BR site toward either remaining MO site, the one it came from or the one originally empty. In our model here we have taken the activated state to be identical for the two processes, transport



51. Approach of the split interstitial model for sodium beta-alumina to the activated state for both transport and reorientation jumps. The large circle is the lattice oxygen ion, the shaded circles are sodium ions on MO sites, and the small circle is the unoccupied MO site.

and reorientation without transport, but they need not be exactly the same, and in particular the activation energies could be somewhat different.

In the presence of a field, Equations (24) and (25) are modified by including with the activation energies Q_μ and Q_ν a term $\pm\alpha = \pm \frac{\sqrt{3}ea}{4kt}E$, where E is the electric field strength, assumed to lie in the $\langle 110 \rangle$ direction, e is the electronic charge, k is the Boltzmann constant, T the temperature in kelvins, and a the lattice parameter. The plus or minus sign is used when the movement from ground to the activated state involves the motion of the Na^+ ions in a direction opposite to or the same as that of the applied field. For the case in which the original split interstitial is oriented perpendicular to the field, there is no net motion of the charge as the defect approaches the activated state and therefore no field-dependent term added to Q_μ and Q_ν .

With eqns (24) and (25) modified in this way, the equilibrium mode replacing the first term in eqn (21) is

$$\begin{aligned}\underline{P}_1 &= (p_{11}, p_{12}, p_{13}) \\ \underline{P}_1 &= \left[\frac{1}{2+\gamma}, \frac{1}{2+\gamma}, \frac{\gamma}{2+\gamma} \right],\end{aligned}\tag{26}$$

$$\text{with } \gamma = \frac{(3/2)\nu(1-\alpha) + 2\mu(1+3\alpha)}{(3/2)\nu + 2\mu},\tag{27}$$

where ν and μ are given by eqns (24) and (25) as written. The ionic current is given by

$$\text{given } J = \sum_i J_i\tag{28}$$

where the subscript i denotes the orientation of the split interstitial before jumping to a new position, and

$$J_i = (Npe) p_{ic} \sum_j \Gamma_{ij} b_{ij}\tag{29}$$

with N the number of regular Na^+ sites per cm^3 , p (as before) the fraction of interstitial sites occupied, e the unit electronic charge (positive), p_{ic} the probability of occupation of the i th orientation in the equilibrium mode in the presence of the field (see eqn. 26), Γ_{ij} the probability per second of a j -type transport jump from an i orientation, and b_{ij} (which can be positive, negative, or zero) the sum of the distances moved by the two ions of the split interstitial in making the entire jump.

Correcting the activation energies for the transport jumps for the effect of the field and retaining only the linear terms as described above, and using the values for p_{ic} implied in eqns (26) and (27) and taking into account the availability of nearby sites into which to jump, the ionic conductivity becomes

$$\sigma = \frac{3Np(1-p)e^2a^2}{6k} \frac{2v+3\mu}{3v+4\mu} \frac{v}{T} . \quad (30)$$

Note that v and μ in this equation are given by eqns (24) and (25), in which the activation energies in the absence of the field are to be used. If Q_μ and Q_v are equal, then eqns (23) and (30) predict that the activation energies for the internal friction and conductivity experiments will be the same. Otherwise, they can differ.

The conductivity data of Wittingham and Huggins [76] have been used in eqn. (30) to calculate v_0 for their crystal ($p = 0.16$), assuming $v \gg \mu$, and this in turn used in eqn. (23) to calculate f_{e1} , the frequency for which 100K would be the temperature of the internal friction peak for a crystal such as ours ($p = 0.3$), and the result compared in Table 6 to the value interpolated from our experimental data. We also list the attempt frequency and activation energy obtained by Walstedt et al [77] from ^{23}Na NMR nuclear-relaxation time T_1 measurements on crystals similar to ours, and the corresponding value of f_{e1} .

Table 6 - Comparison of Internal Friction Relaxation Energies

<u>Source</u>	<u>Ref.</u>	<u>ν_0, Hz</u>	<u>Q, kJ/mole</u>	<u>f_{el}, Hz</u>
Conductivity	76	2.8×10^{12}	15.9	3.4×10^3
NMR	77	$\sim 10^{11}$	~ 14	$\sim 6 \times 10^3$
This Work	-	-	-	8.4×10^3

Conclusions

The agreement among these frequencies lends support to the proposition that the various experiments are all measuring essentially the same process, the motion of the excess Na^+ ions. The difficulty in representing the temperature variation of the frequencies in terms of activation energies and pre-exponential factors in a way that is consistent among the experiments may result from unresolved errors in the measurements, from curvature in the Arrhenius plot combined with the fact that the various experiments do pertain to somewhat different temperature regimes, or may indicate that each experiment reflects a somewhat different averaging over a distribution of processes. The internal friction result is inconsistent with the simple interstitial model in which the excess Na^+ ions occupy the aBR sites. It is consistent with and strongly supports the split interstitial model in which the excess Na^+ ion and the regular Na^+ ion in the same cell occupy two out of the three available MO sites. The close correspondence with the transport process suggests also that transport involves the split interstitial motion.

If resources permit, it is intended to test the possibility of curvature of the Arrhenius plot for the internal friction by extending the accessible frequency-temperature regime using ultrasonic attenuation measurements.

References

1. L. H. Bennett, et. al., *J. Mol. Catalysis* 2, 203 (1977).
2. P. N. Ross and P. Stonehart, *J. Catalysis* 39, 298 (1975).
3. L. H. Bennett, et. al., *Science* 184, 563 (1974).
4. P. N. Ross and P. Stonehart, *J. Catalysis*, 48, 42 (1977).
5. E. A. Torrero, editor, *Microprocessor-New Directions for Designers*, Hayden Book Co., Inc., New Jersey (1975).
6. J. A. Fraunhofer and C. H. Banks, *Potentiostat and Its Applications*, Butterworth & Co., London, (1972), p. 3.
7. J. B. Peatman, *Microcomputer-Based Design*, McGraw-Hill Book Co., New York (1977).
8. Motorola, *M6800 Microcomputer System Data*, Motorola, Inc. (1976).
9. MEK6800D1, *M6800 Microcomputer Design Kit*, Motorola Inc.
10. Motorola, *M6800 Microprocessor Application Manual*, Motorola, Inc., (1975), p. 4-42.
11. *ibid*, p. 4-46.
12. Motorola, *MC14411 Data Sheet*, Motorola, Inc. (1975).
13. Precision Monolithics, Inc., *Technical Specification-AIM DAC100, 8 and 10 Bit I.C. Digital-to-Analog Converter Series*, PMI (1973), p. 4.
14. Precision Monolithics, Inc., *Application Note AN-6, A Low Cost, High Performance Tracking A/D Converter*, (1973).
15. D. F. Hoeschele, Jr., *Analog-to-Digital/Digital-to-Analog Conversion Techniques*, J. Wiley & Sons, Inc., New York (1968), p. 392.
16. J. G. Graeme, *Designing with Operational Amplifiers-Application Alternative*, McGraw-Hill Book Co., N.Y. (1977), p. 44.
17. Motorola, *M6800 Programming Reference Manual*, Motorola, Inc., (1976).
18. J. B. Wester and W. D. Simpson, *Software Design for Microprocessor*, Texas Instruments Learning Center, Dallas, TX (1976).

19. R. H. Uiterwyk, 8K BASIC Version 2.0, Southwest Technical Products Corp., San Antonio, TX (1976).
20. H. H. Bauer, *Electrodics-Modern Ideas Concerning Electrode Reactions*, Wiley & Sons, New York (1972), p. 15.
21. E. B. Magrab and D. S. Blomquist, *The Measurement of Time-Varying Phenomena-Fundamentals and Applications*; Wiley-Interscience, New York (1971), p. 233.
22. W. Schottky, *Wiss. Veroff. Siemenswerke*, 14, H2, 1 (1935).
23. E. Baur and H. Preis, *Z. Elektrochem.*, 43, 727 (1937).
24. K. Kiukkola and C. Wagner, *J. Electrochem. Soc.*, 104, 379 (1957).
25. H. L. Tuller and A. S. Nowick, *J. Electrochem. Soc.*, 122, 255 (1975).
26. T. Kudo and H. Obayashi, *J. Electrochem. Soc.*, 122, 142 (1975); 123, 415 (1976).
27. J. W. Patterson, E. C. Bogren and R. A. Rapp, *J. Electrochem. Soc.*, 114, 752 (1967).
28. A. S. Nowick and D. S. Park, "Fluorite-Type Oxygen Conductors," in Superionic Conductors, ed. by G. D. Mahan and W. L. Roth, Plenum Press (New York, 1976).
29. J. Lefevre, *Ann. Chim.*, 8, 135 (1963).
30. R. Collongues, F. Quelyroux, M. Perez y Jorba and J. C. Gilles, *Bull. Soc. Chim. Fr.*, 1141 (1965).
31. M. R. Thornber, D. J. M. Bevan and J. Graham, *Acta Cryst.*, B24, 1183 (1968).
32. J. G. Allpress and H. J. Russell, *J. Solid State Chem.*, 15, 68 (1975).
33. R. E. Carter and W. L. Roth, "Conductivity and Structure in Calcia-stabilized Zirconia," in Electromotive Force Measurements in High-Temperature Systems, ed. by C. B. Alcock, Elsevier (New York, 1968).

34. D. Michel, Mater. Res. Bull., 8, 943 (1973).
35. D. Michel, Rev. Int. Hautes Tempar. Refract., 9, 225 (1972).
36. B. Hudson and P. T. Moseley, J. Solid State Chem., 19, 383 (1976).
37. W. H. Rhodes and R. E. Carter, J. Am. Chem. Soc., 49, 244 (1966).
38. P. E. D. Morgan, Remarks during panel discussion on "Interconnection Materials", Workshop on "High Temperature Solid Oxide Fuel Cells", Brookhaven National Laboratory, May 5-6, 1977.
39. L. Gordon, Anal. Chem., 27, 1704 (1955).
40. ibid., Record Chem. Progr., 17, 125 (1956).
41. L. Gordon, M. L. Salutsky and H. H. Williard, Precipitation from Homogeneous Solution, John Wiley, New York (1959).
42. M. L. Salutsky and L. L. Quill, J. Am. Chem. Soc., 72, 3306 (1952).
43. T. Moeller and E. P. Horwitz, J. Inorg. Nucl. Chem., 12, 49 (1959).
44. W. W. Wendlandt and T. D. George, Texas J. Sci., 13, 316 (1961).
45. C. B. Bishop, Ph.D. Thesis, Michigan State University (1959).
46. J. M. Axelrod, Ph.D. Thesis, University of Maryland (1959).
47. R. G. Charles, J. Inorg. Nucl. Chem., 27, 1489 (1965).
48. E. L. Head and C. E. Holley, Jr., "The Preparation and Thermal Decomposition of Some Rare Earth Carbonates," Rare Earth Research II, ed. by K. S. Vorres, Gordon and Breach, New York (1963).
49. R. C. Vickery, Chemistry of the Lanthanons, Academic Press, New York, and Butterworths, London (1953), pp. 214-216.
50. ibid., Analytical Chemistry of the Rare Earths, Pergamon Press, New York, (1961), p. 13.
51. G. Czapski, H. Levanon and A. Samuni, Israel J. Chem. 7, 375 (1969).
52. M. P. Pechini, U.S. Patent No. 3,330,697; July 11, 1967.
53. B. N. Sudarikov, V. A. Zaitsev and Yu. G. Puchkov, Nauch. Doklady Vysshei Shkoly, Khim. i Khim. Tekhnol. 1959, No. 1, 80-3; Chem. Abstr., 53, 13738h (1959).

54. L. H. Bennett, et. al., "Materials for Fuel Cells", NBSIR 77-1270, May 1977.

55. K. S. Cole, and R. H. Cole, J. Chem. Phys. 9, 341 (1941).

56. A. D. Franklin et. al., Quarterly Progress Report, "Materials for Fuel Cells," 1 July to 30 September 1977 (October 28, 1977).

57. E. Schouler, G. Giroud, and M. Kleitz, J. Chim Phys, 70, 1309 (1973).

58. J. E. Bauerle, J. Phys. Chem. Solids 30, 2657 (1969).

59. A. D. Franklin, "Statistical Thermodynamics of Point Defects," in Point Defects in Solids, Vol. 1, J. H. Crawford, Jr. and L.M. Slifkin, ed. (Plenum, N.Y., 1972) p. 73.

60. E. Schouler, M. Kleitz, and C. Desportes, J. Chim. Phys. 70, 35 (1973).

61. D. C. Grahame, J. Electrochem Soc. 99, 370C (1952).

62. T. A. Ramanarayanan and R. Rapp, Met. Trans 3, 3239 (1972).

63. E. Schouler and M. Kleitz, J. Electroanal. Chem., 64, 135 (1975).

64. L. A. Simpson and R. E. Carter, J. Am. Ceram. Soc 49, 139 (1966).

65. C. A. Beevers and M. A. Ross, Z. Kristallogr. 97, 59 (1937).

66. cf. J. T. Kummer, Prog. Solid State Chem. 7, 141 (1972).

67. J. H. Kennedy and A. F. Sammells, J. Electrochem., Soc. 119, 1609 (1972).

68. M. S. Whittingham, Electrochimica Acta 20, 575 (1975).

69. W. L. Roth, J. Sol. State Chem. 4, 60 (1972).

70. M. S. Whittingham and R. A. Huggins, J. Electrochem. Soc. 118, 1 (1971).

71. J. C. Wang, M. Gaffari, and Sang-il Choi, J. Chem. Phys. 63, 772 (1975).

72. S. I. Parks and M. Linzer, "An Automated Device for Internal Friction and Modulus Measurements," in Preparation.

73. J. T. Kummer, Prog. Solid State Chem., 7, 141 (1972).

74. M. Barmatz and R. Farrow, 1976 Ultrasonics Symposium Proceedings, edited by J. deKlerk and B. McAvoy, IEEE Cat. No. 76, CH 1120-5su, (IEEE, New York, 1976) p. 662.

75. K. Compaan and Y. Haven, Trans. Far. Soc. 52, 786 (1956);
54, 1498 (1958).
76. M. S. Wittingham and R. A. Huggins, J. Chem Phys. 54, 414 (1971).
77. R. E. Walstedt, R. Dupree, J. P. Remeika, and A. Rodriquez,
Phys. Rev. B 15, 3442 (1977).

U.S. DEPT. OF COMM. BIBLIOGRAPHIC DATA SHEET		1. PUBLICATION OR REPORT NO. 78-1472	2. Gov't Accession No.	3. Recipient's Accession No.
4. TITLE AND SUBTITLE Materials for Fuel Cells		5. Publication Date July 1978		
7. AUTHOR(S) L. H. Bennett, M. I. Cohen, A. L. Dragoo, A. D. Franklin, A. J. McAlister and K. F. Young		8. Performing Organ. Report No.		
9. PERFORMING ORGANIZATION NAME AND ADDRESS NATIONAL BUREAU OF STANDARDS DEPARTMENT OF COMMERCE WASHINGTON, D.C. 20234		10. Project/Task/Work Unit No. 5610494		
12. Sponsoring Organization Name and Complete Address (Street, City, State, ZIP) Power Systems Division Department of Energy Washington, D. C. 20545		11. Contract/Grant No.		
15. SUPPLEMENTARY NOTES				
<p>16. ABSTRACT (A 200-word or less factual summary of most significant information. If document includes a significant bibliography or literature survey, mention it here.)</p> <p>Research is described on hydrogen oxidation electrocatalysis on a number of compounds related to WC. Compounds in the series of $Mo_{1-x}W_xC$, with $x \sim 0.2$, were found to be active, although some uncertainty exists as to the purity of the samples. Some activity was also noted in $W_{0.5}Ti_{0.5}C$ and rhenium metal. Experiments on the preparation of MoP and FeP are described.</p> <p>The microprocessor-controlled potentiostat for electrochemical measurements was completed and is described in detail.</p> <p>Experiments on several techniques for the preparation of very finely-divided Y-doped CeO_2 powder are described. The powders to serve as raw materials for hot-pressing pure, dense, homogeneous ceramics. Straight sintering of some of these specimens yield densities of 95-97% theoretical.</p> <p>The equivalent circuit previously suggested appears to fit very well the frequency-dependence of the impedance of sintered specimens of $Ce_{0.9}Y_{0.1}O_{1.95}$ with sputtered or evaporated Pt electrodes. The bulk part of the data is independent of Po_2 and varies with porosity as expected. An activation energy for the crystal conduction were obtained in agreement with literature values. High temperature instability in the Pt electrodes was observed. The electrode polarization impedance is well-fitted by a Cole-Cole expression. It cannot be attributed to a model proposed earlier involving oxygen atom diffusion in the Pt electrode.</p> <p>Internal friction experiments on a single crystal of $Na\beta-Al_2O_3$ are interpreted in terms of the Na^+ ion motion.</p>				
<p>17. KEY WORDS (six to twelve entries; alphabetical order; capitalize only the first letter of the first key word unless a proper name; separated by semicolons)</p> <p>Electrocatalysis; electrochemical measurements; fuel cells; phosphoric acid; polarization; refractory hard metals; cerium dioxide; sodium beta alumina; solid electrolytes</p>				
18. AVAILABILITY		<input checked="" type="checkbox"/> Unlimited <input type="checkbox"/> For Official Distribution. Do Not Release to NTIS <input type="checkbox"/> Order From Sup. of Doc., U.S. Government Printing Office Washington, D.C. 20402, SD Cat. No. C13 <input checked="" type="checkbox"/> Order From National Technical Information Service (NTIS) Springfield, Virginia 22151		
		19. SECURITY CLASS (THIS REPORT)	21. NO. OF PAGES	
		UNCLASSIFIED	133	
		20. SECURITY CLASS (THIS PAGE)	22. Price	
		UNCLASSIFIED	\$7.25	

